QC
1S93
.S6R
v.62 no.6

TECHNOLOGY

Journal of Research

of the

National Bureau of Standards

IMPORTANT NOTICE

Beginning in July 1959, the Journal of Research will be published in four separate sections. See the announcement given on the last page of this issue.

PUBLIC LIBRARY
JUL 8 1959
DETROIT

JUNE 1959

VOLUME 62 NUMBER 6

U.S. DEPARTMENT OF COMMERCE
Lewis L. Strauss, Secretary
NATIONAL BUREAU OF STANDARDS
A. V. Astin, Director

JUNE • 1959
VOLUME • 62
NUMBER • 6

JOURNAL OF RESEARCH
of the
NATIONAL BUREAU OF STANDARDS

The National Bureau of Standards

Functions and Activities

The functions of the National Bureau of Standards are set forth in the Act of Congress, March 3, 1901, as amended by Congress in Public Law 619, 1950. These include the development and maintenance of the national standards of measurement and the provision of means and methods for making measurements consistent with these standards; the determination of physical constants and properties of materials; the development of methods and instruments for testing materials, devices, and structures; advisory services to government agencies on scientific and technical problems; invention and development of devices to serve special needs of the Government; and the development of standard practices, codes, and specifications. The work includes basic and applied research, development, engineering, instrumentation, testing, evaluation, calibration services, and various consultation and information services. Research projects are also performed for other government agencies when the work relates to and supplements the basic program of the Bureau or when the Bureau's unique competence is required. The scope of activities is suggested by the listing of divisions and sections on the inside of the back cover.

Publications

The results of the Bureau's work take the form of either actual equipment and devices or published papers. These papers appear either in the Bureau's own series of publications or in the journals of professional and scientific societies. The Bureau itself publishes three monthly periodicals, available from the Government Printing Office: The Journal of Research, which presents complete papers reporting technical investigations; the Technical News Bulletin, which presents summary and preliminary reports on work in progress; and Basic Radio Propagation Predictions, which provides data for determining the best frequencies to use for radio communications throughout the world. There are also five series of nonperiodical publications: The Applied Mathematics Series, Circulars, Handbooks, Building Materials and Structures Reports, and Miscellaneous Publications.

Information on the Bureau's publications can be found in NBS Circular 460, Publications of the National Bureau of Standards ($1.25) and its Supplement ($1.50), available from the Superintendent of Documents, Government Printing Office, Washington 25, D.C.

Order all publications from the Superintendent of Documents
U.S. Government Printing Office, Washington 25, D.C.

Use of funds for printing this publication approved by the Director of the Bureau of the Budget (June 24, 1958)

Journal of Research of the National Bureau of Standards Vol. 62, No. 6, June 1959 Research Paper 2957

Thermal Degradation of Polymers At Low Rates[1]

Samuel L. Madorsky

In measuring the rates of thermal degradation of polymers at constant temperatures in the range of 200° to 500° C, one encounters a distortion of the initial parts of the rate curves during the time required to heat the specimen to the pyrolysis temperature. This distortion has been largely overcome by using a new apparatus, based on an electronic balance, in which the degradation of the specimen is carried out at very low rates. The apparatus is equipped with an electronic thermostat that controls the temperature to within ±0.1° C, and also with an automatic recorder that measures both the temperature and the loss of weight of the specimen. Pyrolysis experiments were carried out in a vacuum in this apparatus on pure specimens of polystyrene, poly(α-methylstyrene), polymethylene, high-molecular-weight polyethylene, and low-molecular-weight polyethylene. The initial rates of degradation, in percent of sample per minute, varied from 0.008 to 0.095. Except for the initial parts of the rate curves, in some cases up to about 30 percent loss of weight, the rate curves at low rates resemble closely those previously obtained at high rates of degradation.

1. Introduction

Studies on rates of thermal degradation of polymers in a vacuum by the loss-of-weight method have been carried out at the National Bureau of Standards for a number of years. The method [1, 2][2] consisted in heating a 4 to 6 mg sample of polymer in a platinum crucible suspended from a tungsten spring balance [1, 3] and observing at intervals the loss of weight sustained by the sample, as indicated by the position of a crossline on the extension of the spring. For convenience, the rate experiments were usually planned to be completed within about 8 to 9 hrs. This placed a lower limit on the temperature of operation. In the range 250° to 500° C used in these studies it usually took about 15 min to heat the polymer sample from room temperature to that required in a given experiment. Some vaporization of the sample, in some cases [2] as much as 30 percent of its weight, took place during this heating-up period. Constancy of temperature in any given experiment was a required condition in all the rate studies. The initial loss thus caused a distortion of the initial part of the rate curve and masked the true picture of the initiation of thermal degradation.

This difficulty could be largely overcome by carrying out the rate experiments for longer periods of time at lower temperatures so that the initial loss of sample would be reduced to as low a percentage as practicable. However, continuous operation for long periods of time suggests the use of automatic recording of loss of weight of sample. The spring balance did not lend itself easily to automatic recording.

A new apparatus for the study of rates of thermal degradation of polymers has been designed and constructed. It records continuously and automatically time, temperature, and weight of the polymer sample undergoing decomposition. This new apparatus was used in a study of thermal degradation at low rates of several polymers. The polymers selected for this study were: Polystyrene, which yields both monomer and larger molecular fragments; poly(α-methylstyrene), which yields monomer exclusively; and nonbranched and branched polyethylenes, which yield a spectrum of fragments containing from 1 to n carbons.

2. Apparatus and Experimental Procedure

The elements of the new apparatus (exclusive of the vacuum system) are shown diagramatically in figure 1, and the whole assembly is shown photographically in figure 2.[3] The equipment is built around an electronic microbalance, which is shown in figure 1 in two parts: A, the balance; and B, the electronic unit. From the arm P of the balance a crucible Q containing the polymer sample is suspended within the lower furnace F. The function of the upper furnace E is described later in this paper. The output of the recording balance is fed into one channel of a three-channel recording potentiometer C. The temperature of the furnace F is controlled to about ±0.1° C by an electronic thermostat J, which senses the furnace temperature by means of a platinum resistance thermometer T built into the furnace.[4]

The temperature of the crucible is measured by means of a thermocouple R located directly beneath the crucible, and the output of this thermocouple is fed through the potentiometer buckout D to a second channel of the recording potentiometer C. Portable potentiometer U is used to check the temperature of thermocouple R. Thus, a continuous record of the crucible temperature, as well as of the weight of the sample, is provided on the same sheet. The third channel of the recorder is used to monitor the temperature of either the lower furnace F or the upper furnace E by means of a thermocouple S,

[1] Paper presented at the 134th National Meeting of the American Chemical Society in Chicago, Ill., Sept. 7–12, 1958.

[2] Figures in brackets indicate the literature references at the end of this paper.

[3] The author is indebted to M. Morse of the Electronic Section for his help in the design and construction of some of the electronic parts of the apparatus.

[4] Except for some details which are described, furnaces E and F are similar to those used in connection with the spring balance in previous work [1].

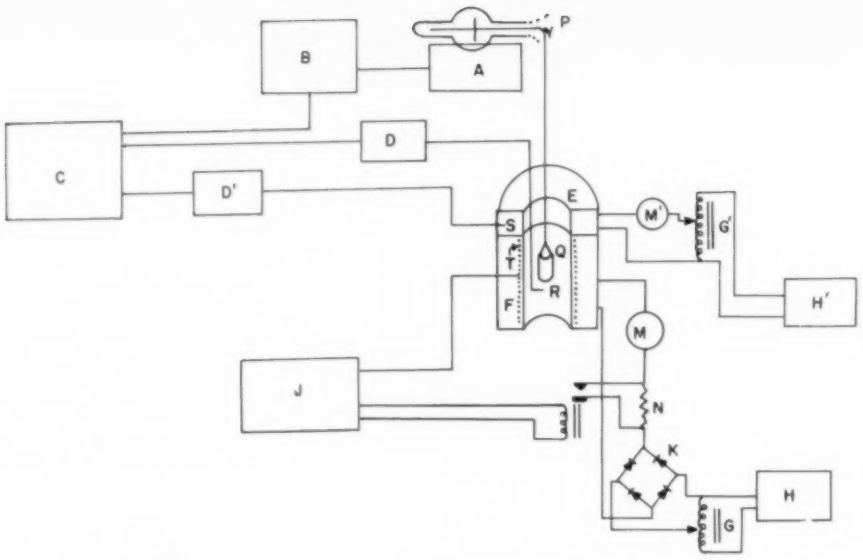

FIGURE 1. *Block diagram of polymer degradation equipment.*

A, Balance, and B, electronic unit—sections of electronic balance; C, 3-point potentiometer recorder; D and D′, potentiometer buckouts; E, upper furnace; F, lower furnace; G and G′, variable autotransformers; H and H′, voltage regulators; J, electronic thermostat; K, bridge rectifier; M and M′, ammeters; N, temperature control resistor; P, balance arm; Q, crucible containing the sample; R, measuring chromel-constantan thermocouple; S, upper furnace chromel-constantan thermocouple; T, platinum resistance thermometer.

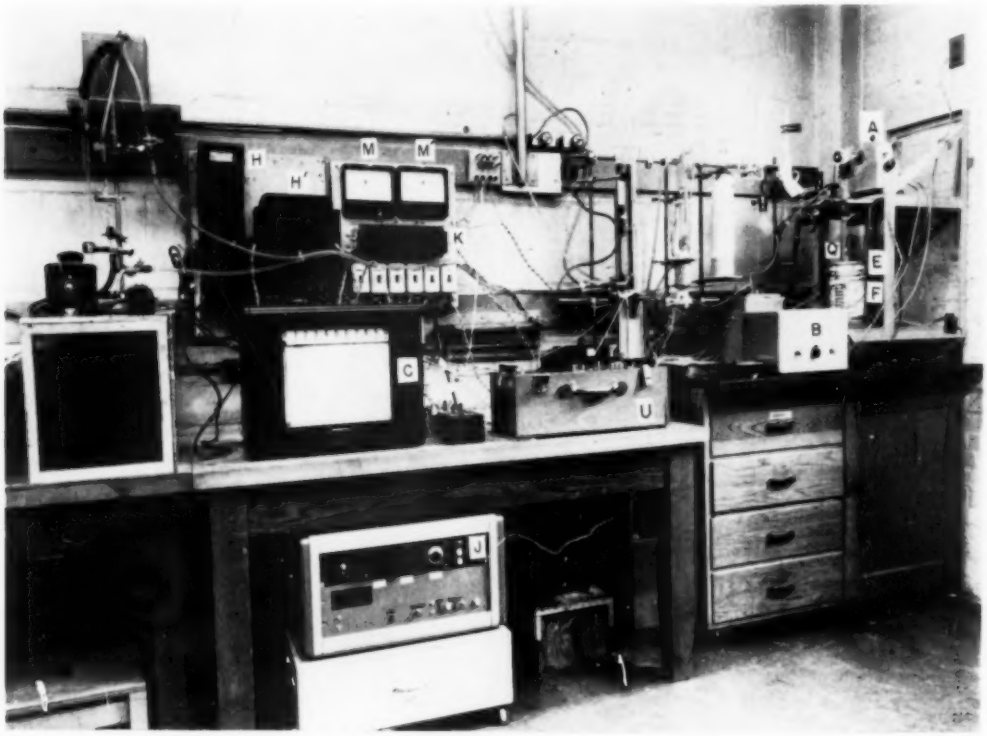

FIGURE 2. *Polymer degradation equipment.*

Letters correspond to the same parts as in figure 1, except U, which indicates potentiometer for checking the temperature of the measuring thermocouple (R in fig. 1).

imbedded in the insulation of E, and connected to the recorder through the potentiometer buckout D′. Power to the furnaces F and E is supplied from the voltage regulators H and H′, respectively, and is controlled by the variable autotransformers G and G′. The power to the lower furnace is, in addition, rectified by the bridge rectifier K. It passes through the resistance N, and is controlled by the electronic thermostat J to maintain the constant temperature. The currents fed into F and E are read by means of ammeters M and M′.

The balance, known as the "Elmic" recording balance, is a modification of an instrument described earlier by Theodore Gast [4]. It makes use of a torsion suspension and a feedback circuit with an electrodynamometer type of actuation. It has four ranges, 10, 5, 2, and 1 mg full scale, the reading being indicated on a meter. For continuous recording, as in the present equipment, a 10-mv recorder is connected to the balance.

The furnace and vacuum system have previously been described [1, 2] in detail. The electronic thermostat [5] consists basically of a resistance-bridge sensing unit, the output from which is amplified and used with a time-proportional control circuit to control the power supplied to the furnace.

The recorder is a standard 3-channel, 10-mv, commercial type. A photograph of a part of the recorder chart is shown in figure 3. The chart gives a record of the first 7 hr of operation of an experiment, which is described later, on the rate of degradation of polymethylene at 362.4° C. The horizontal scale in the chart can be used to calculate the loss in weight and the temperature of the thermocouples S and R (see fig. 1). The vertical scale shows the duration of the experiment. Lines I and II represent records of temperatures indicated by thermocouples S and R, respectively. Line III represents a record of the loss of weight of the sample being heated. In this as well as in all the other rate experiments described in this paper, the 5-mg full-scale range of the electronic balance was used.

The procedure used in the present work is in general the same as that used previously with the spring balance, and has been described in detail [1, 2]. In the present method it also required about 15 min from the time the furnace was raised in position, for the thermocouple R to reach the required temperature (fig. 3).

3. Temperature Measurement

In the previous work on rates of thermal degradation of polymers the cooling-end effect of furnace F, figure 4, was overcome by adding a smaller furnace E on top of furnace F, and keeping the temperature at the interface L constant by means of thermocouples W and W′ in conjunction with an electronic thermostat [5] not shown in the figure. It was assumed that by this means it would be possible to maintain about the same temperature in crucible Q as that indicated by thermocouple R. To check this, a series of blank experiments was carried out in which a chromel-constantan thermocouple V (shown in fig. 4), was placed inside the crucible Q and pressed against the bottom of the crucible by means of a platinum ring. The crucible was suspended in the glass apparatus in the same position as would be used in an actual experiment.

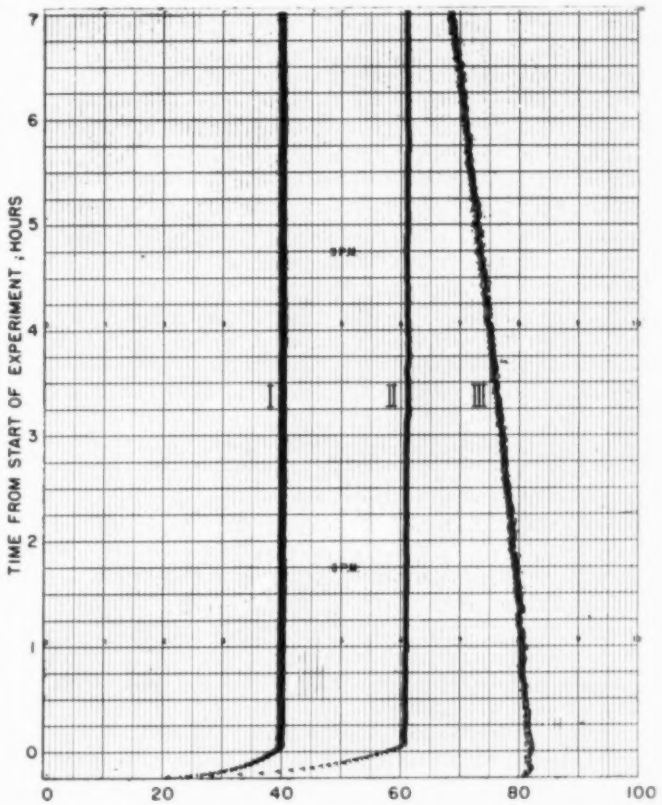

FIGURE 3. *Part of recorder chart, indicating the first 7 hr of operation of an experiment on the degradation of polymethylene at 362.4° C.*

Temperature indicated by thermocouple S (I); temperature indicated by thermocouple R (II); loss of weight of sample (III).

When operating under the experimental conditions previously used, there was a temperature difference between thermocouples R and V of about −14° C. However, it was found that the thermocouples V and R could be made to record the same temperature for a distance of 2 to 3 mm between the crucible and thermocouple R by adjusting the current input in the furnaces E and F. The system was then calibrated by measuring the required currents for a series of temperatures and constructing corresponding current-temperature curves in the range 200° to 400° C. These curves were followed in the experimental work on rates described. Temperature control at the interface L (fig. 4) was not used.

4. Materials Used

The following materials were used in this investigation:

1. Polystyrene. Prepared thermally by the Dow Chemical Co. Average molecular weight of 230,000, as determined by the osmotic pressure method.

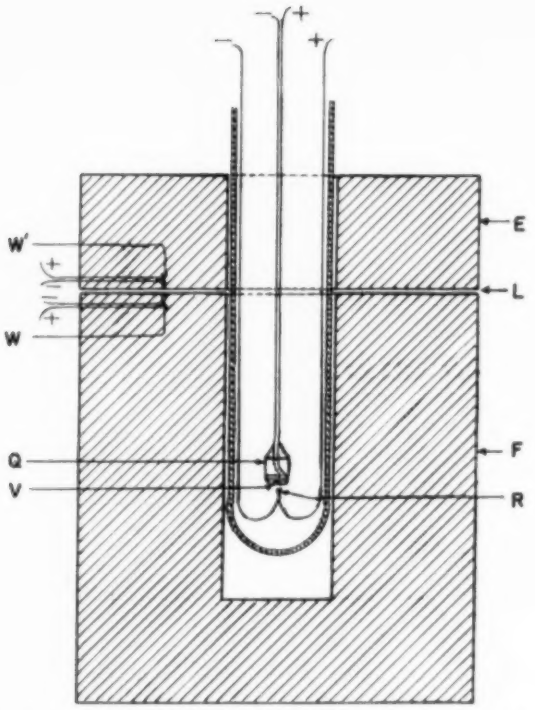

FIGURE 4. *Details of furnace and control of uniformity of temperature.*

E, Upper furnace; F, Lower furnace; Q, platinum crucible; R, V, W, and W', chromel-constantan thermocouples.

2. Poly(α-methylstyrene). Prepared thermally by the Dow Chemical Co. by low-temperature polymerization. Molecular weight by light scattering, 350,000.

3. Polymethylene. Prepared according to the method described by Buckley and Ray [6] by decomposing diazomethane, using trimethyl borate as catalyst. Its molecules are unbranched without methyl groups, and of high molecular weight [7].

4. Polyethylene I. A pure grade polymer, highly branched, and of high molecular weight. Some of its properties are given in table 1.[5]

5. Polyethylene II. A polymer of high purity, having a weight-average molecular weight of about 20,000. Its branching characteristics are not known.

6. Poly(chlorotrifluoroethylene). Prepared without catalyst and having a weight-average molecular weight of 100,000.

All these polymers, except number 4, are the same materials as those used previously in work on rates of thermal degradation at higher temperatures in the tungsten spring balance apparatus [1,2,7,8,9]. As in previous work, the samples were heated in a vacuum at 100° C to a constant weight before they were used in the rate experiments.

TABLE 1. *Properties of branched polyethylene I* [a]

Weight-average molecular weight	525,000
Number-average molecular weight	31,400
Long-chain branching index	18
Density, g/cm³ at 25° C	0.922
Methyls per 1,000 carbons	20.0
Vinyls per 1,000 carbons	0.04
Trans-unsaturation per 1,000 carbons	.02
Vinylidenes per 1,000 carbons	.15
Carbonyls per 1,000 carbons	.03

[a] See footnote 5.

[5] The author is indebted to F. W. Billmeyer, Jr., of the Polychemicals Department of E. I. du Pont de Nemours and Co., Inc., for supplying this polymer and the information on its properties as given in table 1.

5. Experimental

5.1. Rate Measurements

All the experiments on thermal degradation were carried out in a vacuum of about 10^{-4} mm of mercury, obtained by means of an oil pump and mercury diffusion pump. Weights of the samples varied from 4 to 5 mg. The furnace was first heated to the operating temperature in preparation for an experiment, and then raised into position by means of an elevator for pyrolysis of the polymer sample. It ordinarily took about 15 min from the time the furnace was raised into position to the time when thermocouple R (figs. 1 or 4) indicated the operating temperature. The temperature remained constant throughout the experiment to within ±0.1° C. Zero time for a given experiment was taken as the time when this temperature was reached (fig. 3). At the end of an experiment the residue in the crucible was weighed in order to check on the weight loss indicated on the recorder chart. The two values differed by about ±3 percent. This difference is within the combined experimental errors involved in weighing small samples, particularly the residues, on a semimicrobalance used in this work and in reading the recorder chart. The balance weight was used in calculating the results and the error was distributed over the horizontal scale of the recorder chart.

All these polymers, except number 4, are the same materials as those used previously in work on rates of thermal degradation at higher temperatures in the tungsten spring balance apparatus [1, 2, 7, 8, 9]. As in previous work, the samples were heated in a vacuum at 100° C to a constant weight before they were used in the rate experiments.

In figures 5, 6, 7, and 8, percentage volatilization is plotted as a function of time for polystyrene, poly(α-methylstyrene), polymethylene, and polyethylene I, respectively. Generally the curves resemble those obtained for the same materials in the spring balance apparatus, except for the initial parts. Whereas in the previous work, which was carried out at much higher temperatures, the losses during the heating-up period were in some cases as high as 10 percent, the curves in figures 5, 6, 7, and 8, show practically no such initial losses.

Curves showing rates of degradation as a function of percentage of volatilization for the four polymers are shown in figures 9, 10, 11, and 12. The rates were calculated from the volatilization-time curves and are expressed either as percentage of sample (K_1-curves) or as percentage of residue (K_2-curves). In the case of polystyrene the K_1 curve is given only for 299.3° (dash-and-dot line of fig. 9). This curve has a maximum at about 30 percent volatilization. In the previous work at higher temperatures [1] the maxima were between 35- and 40-percent volatiliza-

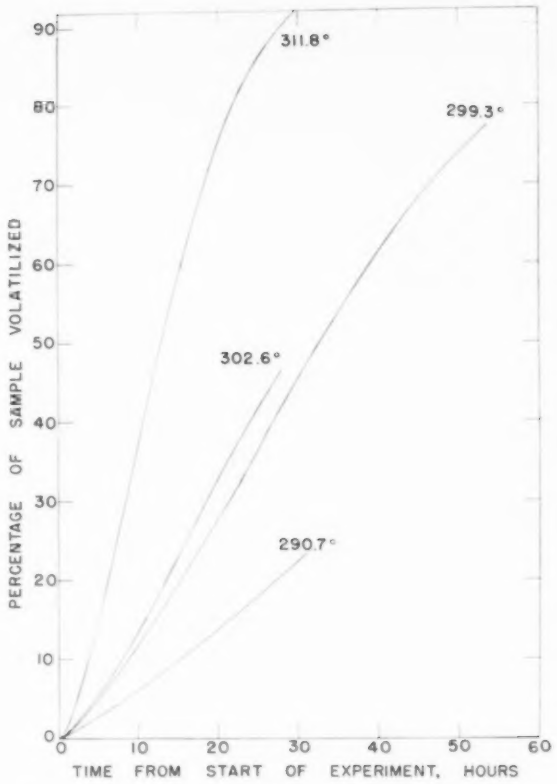

FIGURE 5. *Thermal degradation of polystyrene.*

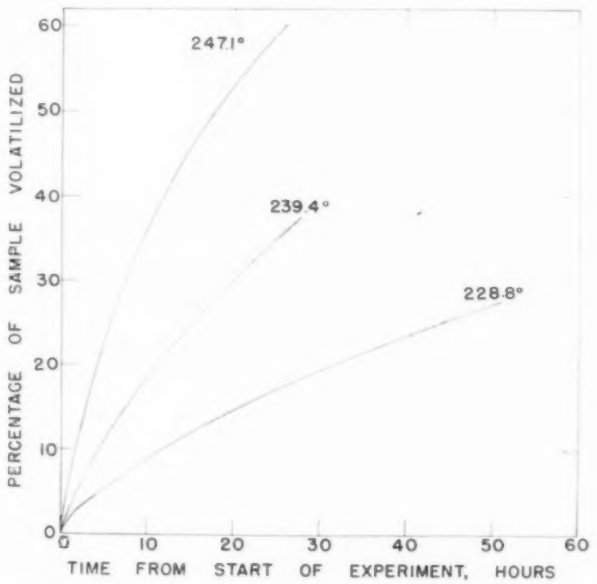

FIGURE 6. *Thermal degradation of poly(α-methylstyrene).*

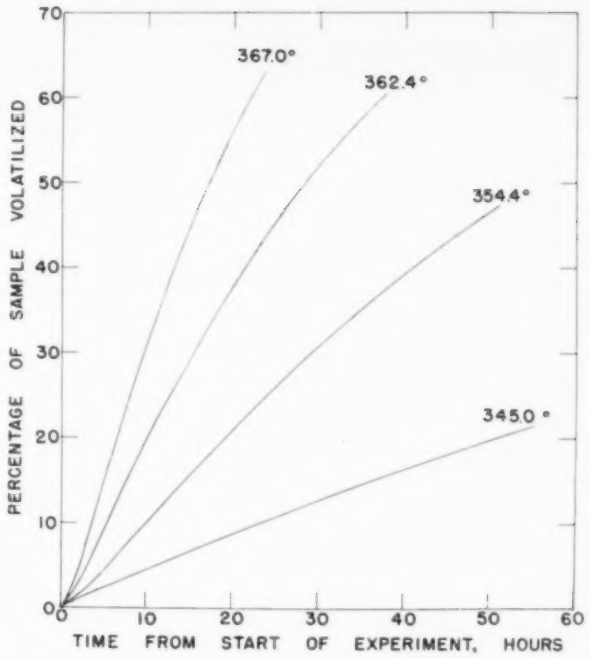

FIGURE 7. *Thermal degradation of polymethylene.*

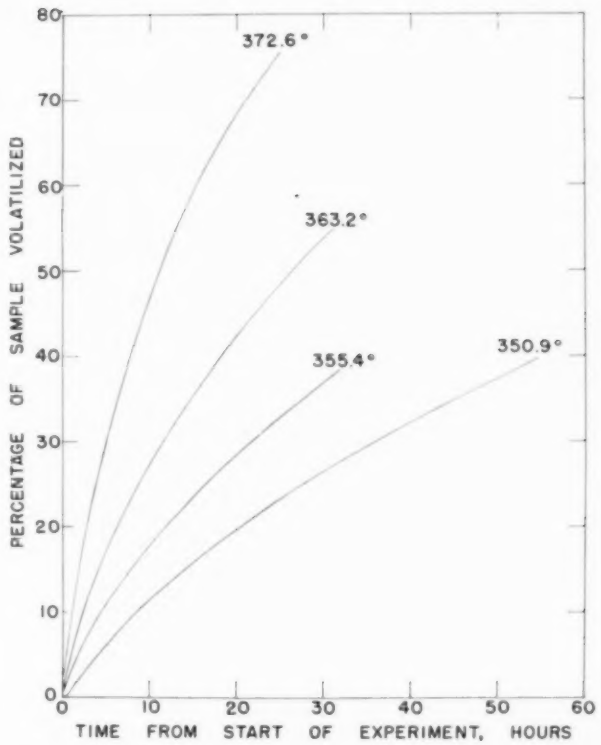

FIGURE 8. *Thermal degradation of branched polyethylene.*

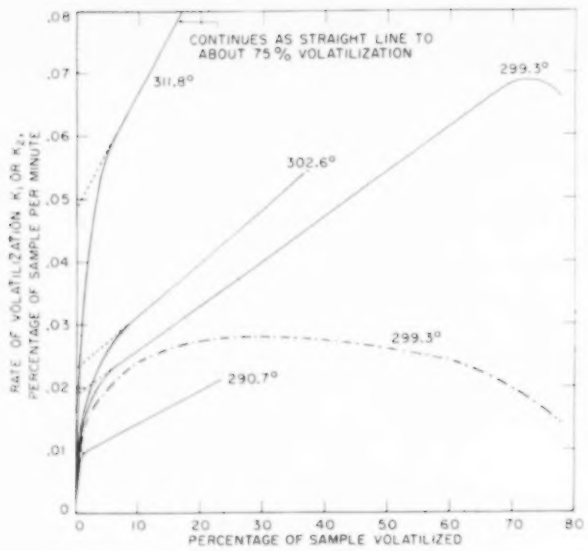

FIGURE 9. *Rates of volatilization of polystyrene.*
(– . – . – . –, K_1 rate; —— K_2 rates)

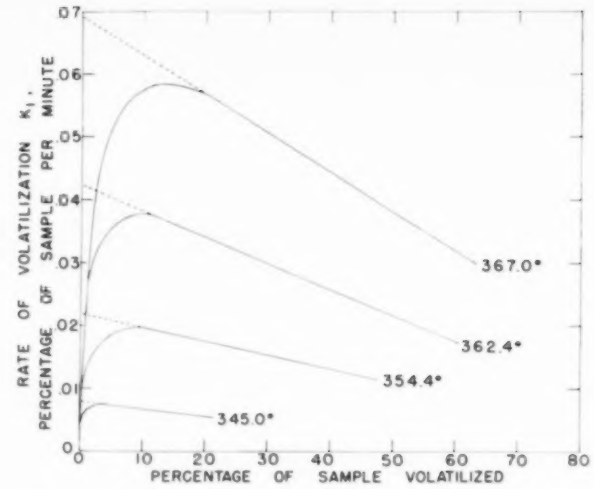

FIGURE 11. *Rates of volatilization of polymethylene.*
(K_1 rates)

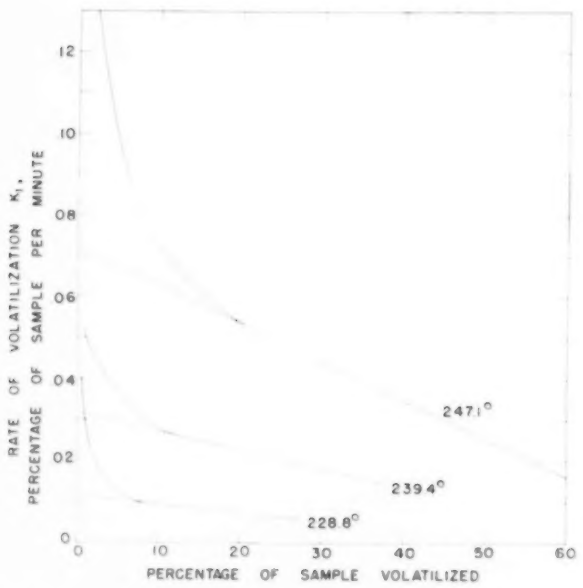

FIGURE 10. *Rates of volatilization of poly(α-methylstyrene).*
(K_1 rates)

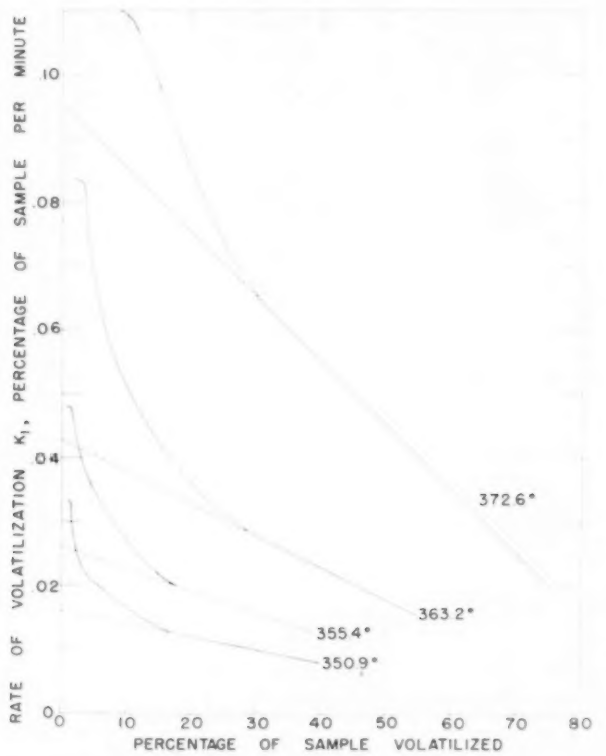

FIGURE 12. *Rates of volatilization of branched polyethylene.*
(K_1 rates)

TABLE 2.—*Rates of thermal degradation of polymers*

Polymer	Temperature	Duration of experiment	Total volatilized	Initial rate
	°C	hr	%	%/min
Polystyrene	290.7	31.0	23.3	0.0090
	299.3	53.4	77.6	.0190
	302.6	27.8	46.4	.0230
	311.8	29.8	92.1	.0484
Poly(α-methylstyrene)	228.8	51.0	27.5	.0110
	239.4	27.8	37.8	.0320
	247.1	26.0	60.4	.0720
Polymethylene	345.0	55.3	21.5	.0080
	354.4	51.0	47.6	.022
	362.4	37.8	60.6	.0424
	367.0	23.8	63.1	.0694
Polyethylene I	350.9	54.5	39.6	.0160
	355.4	31.0	38.6	.0260
	363.2	31.0	54.7	.0430
	372.6	25.0	75.3	.0950
Polyethylene II	360.2	31.0	51.8	.051
Poly(chlorotrifluorethylene)	331.8	44.0	39.2	.043

tion. The K_2 curves do not differ much in shape from those obtained previously in the spring balance. All the pertinent experimental data on rates of thermal degradation obtained in the present investigation are given in table 2.

The K_1 curves for poly(α-methylstyrene) in figure 10 differ up to about 20- to 25-percent volatilization, from the corresponding curves obtained at higher temperatures. Here the rates are initially high, then drop gradually in convex lines to about 8- to 20-percent volatilization, and finally in straight lines in the manner of a first-order reaction. In the previous work at higher temperatures the rates were initially low, then rose gradually, reaching maxima between 20- and 25-percent volatilization, and finally dropped in the same manner as shown in figure 10. It is likely that this difference is due not to the difference in temperature but to the fact that in the present work the rates are much slower and are recorded automatically so that the details are more clearly delineated and the results are more dependable.

The K_1 curves for polymethylene (fig. 11) are similar to those obtained previously at higher temperatures. Polyethylene I (fig. 12) had not been studied previously. It would not be correct to compare the present results with those obtained previously for polyethylene II, because the two polymers are different in structure. On the other hand, a comparison between the K_1 curves for polyethylene I and for polymethylene shows a striking difference between the thermal behavior of these two polymers. The polymethylene rate curves start at the origin, rise to maxima at about 3- to 20-percent loss, then fall in straight lines approaching zero at about 100 percent loss; while the polyethylene curves start at a fast rate, curve gradually in convex form to about 16- to 30-percent loss, and then fall in straight lines like the polymethylene curves. The explanation undoubtedly lies in the fact that volatilization in both polymers is due to fragments breaking off from the ends of the polymer chains; and, since the branched polyethylene has more ends, it volatilizes faster initially until most of the branches disappear.

The intercepts of the extrapolated straight parts of the rate curves K_1 or K_2 in figures 9, 10, 11, and 12 are the apparent initial rates and indicate what the actual initial rates would have been were it not for rate-disturbing factors, such as rapid initial drop in the average molecular weight, presence of foreign groups at the ends of chains, or weak points [10] in the chains. However, the effects of these disturbing factors disappear after degradation proceeds to some extent.

The shape of the polystyrene rate curves (fig. 9) indicates that the reaction approaches a zero order. The pending benzene rings seem to have a stabilizing effect on the chains, so that the number of chain-ends and, therefore, the rate of formation of monomer dimer, and trimer at these ends by an unzipping process stays constant. In the case of poly(α-methlystyrene), the presence of quaternary carbons in the chain imparts instability to the chain, so that formation of new chain ends takes place at random and the reaction is of the nature of a first order one. In polymethylene and polyethylene the chains also break at random and the reaction is first order.

5.2. Activation Energies

The activation energies were obtained by plotting the logarithm of the apparent initial rates at various temperatures for any given polymer as a function of the inverse of the absolute temperature. The results are shown in figures 13, 14, 15, and 16 for polystyrene, poly(α-methylstyrene), polymethylene, and polyethylene I, respectively. In figures 13, 14, and 15 are also plotted the results of the previous work [1, 2, 8] carried out on the same materials at higher temperatures. Judging from the position of the dashed line (for the previous work) with respect to the solid line (for the present work), there seems to be a discrepancy in the two sets of temperatures to the extent of 17° for polystyrene, 12° for poly(α-methylstyrene), and 14° for polymethylene.

In the present work the temperatures were checked by actual measurements, as described earlier and illustrated in figure 4. In the previous work it was erroneously assumed that there would be a region of uniform temperature within 2 to 3 mm distance above the thermocouple R (fig. 4). Actually the temperature of the crucible above R must have been lower than that indicated by the thermocouple by the amounts shown above. A lowering of the temperature readings in the earlier work will not change in any way the shape of the volatilization-time curves, rate curves, or the initial rates, but will lower slightly the values of the activation energies involved. Thus the activation energies of polystyrene, poly(α-methylstyrene), and polymethylene, after correcting the temperatures, are 55, 55, and 73 kcal/mole, respectively, as compared with the values of 58, 58, and 76 kcal/mole reported in the previous work for the same polymers. The results for branched polyethylene I, shown in figure 16, indicate an activation energy of 64 kcal.

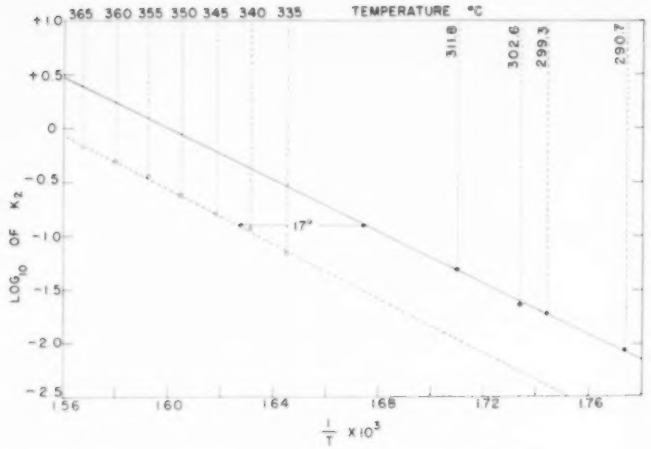

FIGURE 13. *Activation energy of thermal degradation of polystyrene.*

(Dashed line indicates previous work)

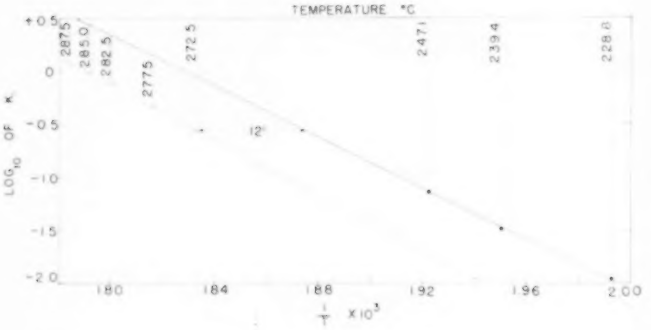

FIGURE 14. *Activation energy of thermal degradation of poly(α-methylstyrene).*

(Dashed line indicates previous work)

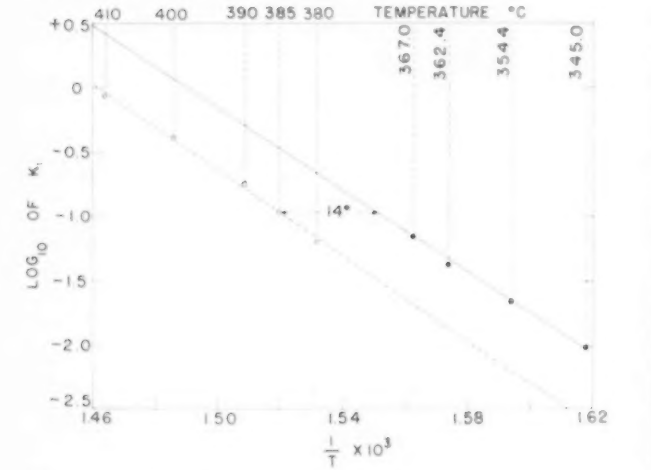

FIGURE 15. *Activation energy of thermal degradation of polymethylene.*

(Dashed line indicates previous work)

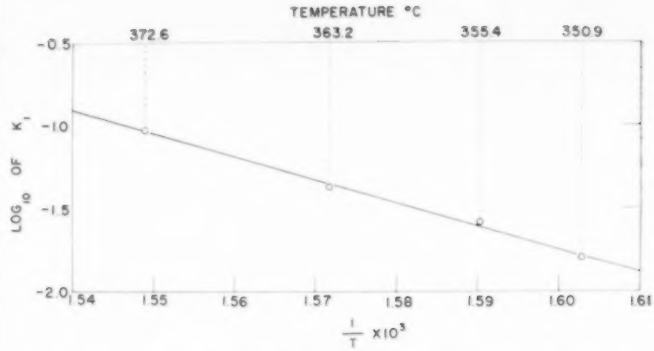

FIGURE 16. *Activation energy of thermal degradation of branched polyethylene.*

5.3. Poly(chlorotrifluoroethylene) and Low-Molecular-Weight Polyethylene

As a further check on the temperature readings in the tungsten spring balance, two polymers, poly(chlorotrifluoroethylene) of average molecular weight 100,000, and polyethylene II of molecular weight 20,000, were pyrolyzed in the electronic balance at relatively low temperatures. The results are shown in figures 17 and 18. Pertinent data for these polymers are given in table 2. The pyrolysis curves and the rate curves resemble closely those obtained previously [1, 9] for these two polymers at higher temperatures. However, when the results obtained in figures 17 and 18 and those obtained in the previous work are plotted in terms of logarithm of the initial rate as a function of inverse of absolute temperature, we find that the temperature readings in the previous work are too high by 14° and 13° C for poly(chlorotrifluoroethylene) and polyethylene II, respectively, and the activation energies too high by 3 kcal/mole for both polymers.

5.4. Correction of Previous Work

On the basis of data in table 2 and the time and rate curves shown, it is suggested that corrections be made in the temperature data and activation energies obtained by the present author and his coworkers in their studies of rates of thermal degradation of a number of polymers determined previously in the tungsten spring balance. The suggested corrections for temperatures and the corrected activation energies are shown in table 3. The corrections given in this table for polystyrene of molecular weight 230,000, poly(α-methylstyrene), polymethylene, poly(chlorotrifluoroethylene), and polyethylene of molecular weight 20,000, are those found experimentally in the present investigation. The corrections for the other polymers shown in the table are those based on the average decrease of temperature and activation energies found experimentally in this work. These averages are −14° C and −3 kcal/mole. No corrections are required for Teflon [10] since the temperatures for this polymer were calibrated by comparing the results obtained in the spring balance

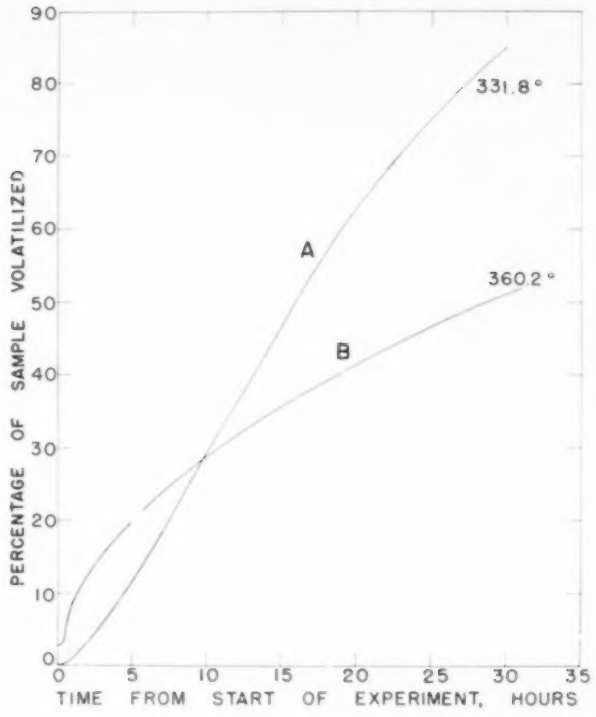

FIGURE 17. *Thermal degradation of poly(chlorotrifluoroethylene) (A) and low-molecular-weight polyethylene (B).*

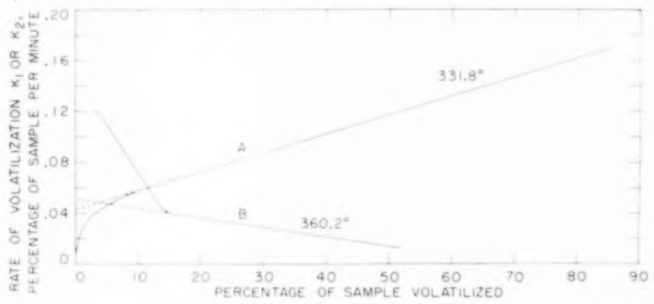

FIGURE 18. *Rates of volatilization of polymers as a function of percentage volatilization.*

Poly(chlorotrifluoroethylene) (A) in percent of residue per minute (K_2 rates); low-molecular-weight polyethylene (B) in percent of sample per minute (K_1 rates)

with those obtained by a pressure method. In the more recent work in the spring balance [11, 12] the furnace was calibrated in the same manner as described in the present work.

6. Comparison of Rates Obtained by Several Investigators

In view of the difficulties involved in measuring temperatures in a study of thermal degradation of polymers, there is a likelihood that there should be disagreements in the results obtained by various investigators. In figure 19 the results of rate studies obtained by Jellinek [13, 14], Grassie and Kerr [15], and the present author are compared. The results of all these investigators were obtained in vacuum,

TABLE 3. *Corrections to be applied to experimental temperature and to activation energies in previous work*

Polymer	Reference	Temperature correction	Experimental and corrected activation energies
		°C	*kcal/mole*
Polystyrene (230,000)	[1]	−17	55
Polystyrene (106,000)	[1]	−14	55
Polystyrene (584,000)	[1]	−14	55
Polyethylene (20,000)	[1]	−13	63
Poly(*m*-methylstyrene)	[2]	−14	56
Poly(α-deuterostyrene)	[2]	−14	55
Poly(α-methylstyrene)	[2]	−12	55
Hydrogenated polystyrene	[2]	−14	49
Poly(methyl methacrylate) A	[2]	−14	30
Poly(methyl methacrylate) B	[2]	−14	52
Poly(methyl acrylate)	[2]	−14	34
Polymethylene	[8]	−14	72
Polypropylene	[8]	−14	58
Polyisobutylene	[8]	−14	49
Polybenzyl	[8]	−14	50
Poly(β-deuterostyrene) (high molecular weight)	[8]	−14	56
Poly(chlorotrifluoroethylene)	[9]	−14	57 [a]
Poly(α,β,β-trifluorostyrene)	[9]	−14	64
Poly(p-xylylene)	[9]	−14	73

[a] In reference [9] the activation energy for poly(chlorotrifluoroethylene) is given as 66 kcal/mole. This is a misprint and should have read 60 kcal. When reduced by 3 units the activation energy becomes 57.

using polymers prepared without catalysts and having high molecular weights. The solid lines in figure 19 represent polystyrene, and the dash-and-dot lines represent poly(α-methylstyrene); also, the letters J, G, and M, in front of the temperatures indicate the work of Jellinek, Grassie, and Madorsky, respectively. Temperatures in parentheses represent the uncorrected temperatures obtained by the present author in the tungsten spring balance.

The polystyrene curves M–290.7° and M–311.8° are the same as those given in figure 5. Curve G–290° was obtained by Grassie and Kerr [15] on a sample of polystyrene (S–3), prepared without a catalyst and having a molecular weight of over 300,000. Their rate apparatus consisted of a dynamic molecular still heated electrically [16]. The G–290° curve is very close to the M–311.8° curve, so that the temperature given by Grassie and Kerr is at least 20° lower than the one obtained in the electronic balance in the present work. The M–290.7° curve lies far below the G–290° curve. At higher temperatures the J–364° curve was obtained by Jellinek for a polystyrene sample (F_{II}), prepared without catalysts and having a molecular weight of 200,000 [13, 14]. He used a quartz spring balance. Curves M–328°(345°) and M–348°(365°) were obtained by the present author on a thermally prepared polystyrene of molecular weight 230,000, using a tungsten spring balance [1]. Position of J–364° is close to that of M–328°(345°) and is far below that of M–348°(365°) curve. Thus Jellinek's temperature reading is about 30° to 32° higher than that of the present author and about 50° higher than that of Grassie and Kerr.

In the case of poly(α-methylstyrene) Jellinek [14] pyrolyzed a 70,000 molecular weight sample in the quartz spring apparatus and obtained a volatiliza-

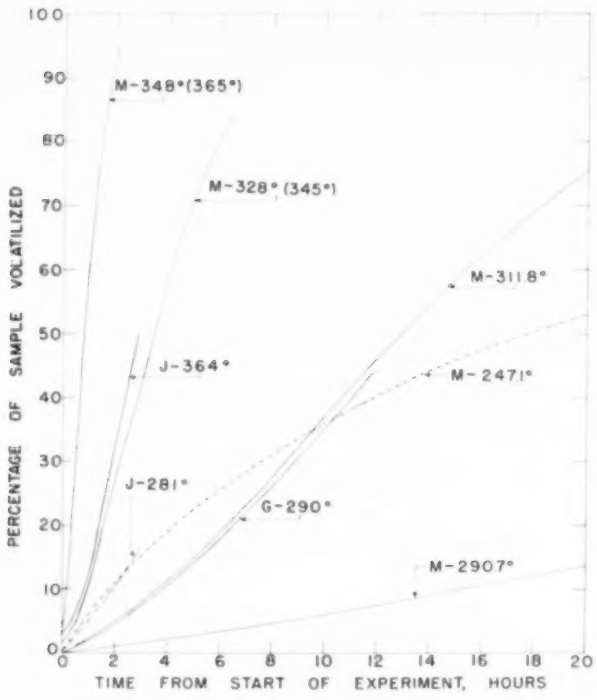

FIGURE 19. *Comparison of results obtained by various investigators on thermal degradation of polymers at various temperatures.*

————, Polystyrene; — . — . — . — ., poly(α-methylstyrene). The letters in front of each temperature refer to the investigators: G, Grassie; J, Jellinek; M, Madorsky. Temperatures in parentheses are uncorrected temperatures obtained in the spring-balance pyrolysis apparatus.

tion-time curve shown in figure 18 as J–281°. The curve M–247.1° is the same as the 247.1° curve given above in figure 6. Jellinek's temperature reading appears to be about 34° higher than the one obtained by the present author using the electronic balance.

It is believed that the principal reason for the differences between the various investigators lies in measurement of the temperature of the sample. As shown earlier in this paper, this measurement is very sensitive to the maintenance of a uniform temperature in the zone where the sample and the thermocouple are located and to the relative position of these two in this zone.

7. Discussion and Conclusions

A quantitative determination of rates, and consequently of activation energies, in the study of thermal degradation of polymers by the pressure or loss-of-weight method is beset by many difficulties. The following are some of the more serious difficulties.

1. Spattering caused by the bursting of bubbles of gaseous products of degradation which accumulate in the polymer sample.

2. Delay in the vaporization of volatile products due to slow diffusion through the solid or semisolid polymer.

3. The difficulty of maintaining a uniform temperature through the polymer sample due to its poor heat conductivity. This is further aggravated by the fact that the degradation reactions involved are endothermic in most cases.

4. The difficulties associated with measurement of temperature.

5. Uncertainties in temperature and rate observation during the initial heating-up period.

With regard to points 1, 2, and 3, the difficulties were reduced to a minimum in the present work as well as in the earlier work by limiting the weight of the samples to about 5 mg or less. As to point 4, precautions were taken in the present work to obtain a uniform temperature in the region where the thermocouple and the sample are located in close proximity to each other. The difficulties encountered during the initial stage of degradation, referred to in point 5, were reduced in this work to a minimum by operating at low temperatures, so that very little loss by volatilization took place during the 15-min heating-up time.

A study of rates of degradation at low temperatures, in conjunction with automatic recording of loss of weight and of temperature, not only renders the observations more accurate, but also reveals details that are otherwise masked by a rapid rate of volatilization at high temperatures. This is particularly true for polyethylene and poly(α-methylstyrene) where the actual initial rates of degradation are very high.

8. References

[1] S. L. Madorsky, J. Polymer Sci. **9,** 133 (1952).
[2] S. L. Madorsky, J. Polymer Sci. **11,** 491 (1953).
[3] S. L. Madorsky, Rev. Sci. Instr. **21,** 393 (1950).
[4] Theodore Gast, Feintechnik **53,** 172 (1949).
[5] F. A. Ransom, Control Eng. **1,** 1 (1954); also, U.S. Patent 2,376,488.
[6] G. D. Buckley and N. H. Ray, J. Chem. Soc. **1952,** 3701.
[7] L. A. Wall, S. L. Madorsky, D. W. Brown, S. Straus, and R. Simha, J. Am. Chem. Soc. **76,** 3430 (1954).
[8] S. L. Madorsky and S. Straus, J. Research NBS **53,** 361 (1955) RP2553.
[9] S. L. Madorsky and S. Straus, J. Research NBS **55,** 223 (1955) RP2624.
[10] S. L. Madorsky, V. E. Hart, S. Straus, and V. A. Sedlak, J. Research NBS **51,** 327 (1953) RP2461.
[11] S. Straus and S. L. Madorsky, J. Research NBS **61,** 77 (1958) RP2888.
[12] S. L. Madorsky and S. Straus (submitted for publication in the J. Polymer Sci.).
[13] H. H. G. Jellinek, J. Polymer Sci. **3,** 850 (1948).
[14] H. H. G. Jellinek, J. Polymer Sci. **4,** 13 (1949).
[15] N. Grassie and W. W. Kerr, Trans. Faraday Soc. **53,** 234 (1957).
[16] N. Grassie and H. W. Melville, Proc. Royal Soc. (London) [A]**199,** 1 (1949).

WASHINGTON, December 5, 1958.

Journal of Research of the National Bureau of Standards Vol. 62, No. 6, June 1959 Research Paper 2958

P s in Metals Caused by Collision With Liquid Drops and Soft Metal Spheres

Olive G. Engel

An equation is developed to give pit depth as a function of collision velocity for pits formed in soft to medium-hard metal plates as a result of collision with liquid drops. The rear face of the target plate must be a free surface. The plate thickness must not be less than 1.5 to 2.0 times the drop diameter nor greater than 4 to 5 times the drop diameter. It is shown that, under the same conditions on the target plate, the equation is also applicable to pits formed in soft to medium hard metal plates as a result of collision with spheres of the same metal that flow radially as a result of the collision. Pit-depth-versus-velocity data obtained in other laboratories were used to test the equation. Metals used as targets were copper, 1100–0 aluminum, 2024–0 aluminum, lead, steel, soft iron, and zinc. Mercury was used as the drop liquid against copper, aluminum, lead, and steel. Water was used as the drop liquid against copper, aluminum, and lead. Spheres of copper, aluminum, lead, soft iron, and zinc were used against targets of the same materials, respectively. The equation can be used to calculate the dynamic compressive yield strength of soft to medium-hard metals.

1. Introduction

Current research on pits produced in high-speed collisions includes: (a) the investigation of solid projectiles impinging against solid targets (artillery experiments); (b) the investigation of solid projectiles impinging against liquid surfaces (water entry problems); (c) the investigation of liquid drops impinging against solid surfaces (high-speed rain-erosion research); and (d) the investigation of liquid drops colliding with liquids. The work that is described in this paper was initiated as part of a high-speed rain-erosion research program and the entire program was conducted under the sponsorship of the Materials Laboratory, Directorate of Laboratories, Wright Air Development Center.

It is difficult to test for the rain-erosion resistance of structural materials at very high collision velocities because of the problems involved in accelerating either waterdrops or test specimens to the velocities in question. It has been suggested that it may be possible to bypass these problems by using drops of high-density liquids instead of drops of water for the erosion tests.[1] To develop this idea into a reliable test procedure, it is necessary to know the corresponding velocities-for-equal-damage when the test specimen collides with a drop of a high-density liquid and when it collides with a drop of water. The pit-depth-versus-velocity equation presented in this paper was developed to provide this information.

It has also been found that this pit-depth-versus-velocity equation is applicable without change to collisions of spheres of the soft, ductile metals with targets of the same metal in those cases in which the sphere flows as a result of collision with the metal plate when the collision velocity is as high as 5,000 ft/sec. Pellets of the soft, ductile metals appear, therefore, to behave as though they were liquid drops when they impinge against a solid surface at this velocity.

The experimental work reported in this paper was done in other laboratories.[2] [3]

2. Collisions With Liquid Drops

The damage done to solid materials that collide at high speed with liquid drops depends both on the properties of a drop of liquid in collision and on the characteristic properties of the solid.

2.1. Damaging Properties of a Liquid Drop in High-Speed Collisions

As the relative collision velocity changes, the effects of collisions with a liquid drop also change. In high-speed collisions with the planar surface of a solid the liquid drop acts as though it were a hard solid sphere, but, unlike a sphere of hard solid material, it undergoes an ultrarapid radial flow outward about the point of impingement [1,2].[4] These damaging properties of an impinging liquid drop vary in intensity depending on the density of the liquid of the drop, on the relative collision velocity, and on the extent to which the solid surface yields under the blow. At any given impingement velocity, collision of a ductile metal plate with a liquid drop does not produce as deep a pit as collision of the same metal plate with a hard solid sphere would produce. This is because when a planar solid collides with a liquid drop part of the collision energy is transformed into the radial flow of the liquid.

[1] This idea was suggested by the rain-erosion research group working at Convair Division of General Dynamics Corp. in San Diego, Calif.

[2] The pit-depth-versus-velocity data reported for collisions of solid targets with liquid drops were obtained by the rain-erosion research group working at Convair Division of General Dynamics Corp.

[3] The pit-depth-versus-velocity data for collisions of spheres of the soft metals that flow as a result of the collision were obtained by Partridge, VanFleet, and Whited at the University of Utah (see reference [11].)

[4] Figures in brackets indicate the literature references at the end of this paper.

2.2. Response of Solid Target Materials

The extent and type of damage produced on solids as a result of collision with liquid drops depends strongly on the characteristic properties of the solids [1]. If the damage is to be described mathematically, it will be necessary to develop separate equations for the damage produced on solid materials that have widely different properties.

2.3. Dimensional Analysis of the Damage

To develop an equation that will give the depth of pits produced in high-speed collision between the planar surface of a solid and a liquid drop is a difficult problem from a theoretical standpoint. Dimensional analysis has proved to be a useful tool in the solution of difficult problems in the past. It is used in this paper to develop a pit-depth-versus-velocity equation.

The method of dimensional analysis has been discussed by Buckingham [3, 4], Bridgman [5], Birkhoff [6], and others. If a physical process can be described by physical quantities of n different kinds, and if none of the quantities involved in the process has been overlooked, then the process is described by the equation:

$$f(Q_1, Q_2, \ldots Q_n, r_1, r_2, \ldots) = 0, \qquad (1)$$

where the Q's are the physical quantities involved in the process, and the r's are ratios. The Q's are quantities of different kinds. If several quantities of any one kind are involved in the process, they are specified by the value of any one of them, and by ratios of the others to this one. These ratios are the r's of eq (1).

A certain number k of the Q's are selected as fundamental. The k selected Q's comprise a possible set of fundamental dimensions and the remaining Q-quantities can be expressed in terms of them. After the k fundamental Q's, now designated as S's, have been selected, the remaining Q's are designated as P-quantities. In a mechanical system the number of the S-quantities is three because the total number of dimensions required to express any of the Q-quantities involved in a mechanical process is three. These dimensions are usually mass, length, and time.

Equation (1) may be put in the form

$$F(\pi_1, \pi_2, \ldots \pi_{n-k}, r_1, r_2, \ldots) = 0, \qquad (2)$$

where the π's are independent products of the arguments Q, and are dimensionless in the fundamental units, or in the form

$$\pi_1 = F'(\pi_2, \pi_3, \ldots \pi_{n-k}, r_1, r_2, \ldots) \qquad (3)$$

in which π_1 is any one of the π's.

A π-product is formed by multiplying each P-quantity by the S-quantities, which are raised to whatever powers $\alpha, \beta, \ldots \kappa$ are required so that their units will just cancel those of the P-quantity to make the π-product dimensionless. That is,

$$\pi = (Q_1^{\alpha} \cdot Q_2^{\beta} \cdot \ldots Q_k^{\kappa}) P. \qquad (4)$$

From a consideration of the equation for the pressure that results when a solid surface runs into a liquid drop at high speed [2], of the expression for the radius of flow of the liquid about the central point of the collision [2], and of the well known equation for the shear stress between layers of liquid in laminar flow, the quantities (see table 1) that should prove to be important in determining the damage that results from the collision of a solid surface with a liquid drop are: c, c', ρ, ρ', V, μ, γ, γ', d, and δ' where c is the speed of sound, ρ is the density, V is the relative impingement velocity, μ is the viscosity, γ is the surface tension, d is the diameter of the liquid drop, and δ' is the damage parameter. Primed quantities refer to the solid material; unprimed quantities refer to the liquid of the drop. In addition to these quantities there is the energy per unit volume put in, E', and the energy per unit volume returned, e', during the collision. E' is the energy per unit volume that the solid material can absorb without nonrecoverable deformation or fracture; e' is the energy per unit volume that the solid material can return. The ratio of these quantities, e'/E', is a measure of the resilience of the solid material.

TABLE 1. *The three fundamental S-quantities, the P-quantities, and the r-ratios involved in rain erosion damage*

Quantity	Dimensions	S	P	r	Dimensionless products, π
Impact velocity, V	L/T	S_1			
Drop diameter, d	L	S_2			
Density of liquid, ρ	M/L^3	S_3			
Viscosity of liquid, μ	M/LT		P_1		$\pi_1^{-1} = \rho d V/\mu$ Reynolds Number
Surface tension of liquid, γ	M/T^2		P_2		$\pi_2^{-1} = \rho d V^2/\gamma$ (Weber Number)^2
Velocity of sound in liquid, c	L/T		P_3		$\pi_3 = c/V$ (Mach Number, liquid)$^{-1}$
Damage parameter, δ'	L		P_4		$\pi_4 = \delta'/d$
Yield or rupture energy density of the solid, E'	M/LT^2		P_5		$\pi_5 = E'/(\rho V^2)$
Ratio of sound velocities, c/c'				r_1	
Ratio of densities, ρ/ρ'				r_2	
Ratio of surface tension and interfacial tension, γ/γ'				r_3	
Resilience, e'/E'				r_4	

Of these quantities V, d, and ρ are arbitrarily selected to be the S-quantities, S_1, S_2, and S_3, respectively. Considering both these S-quantities and the remaining quantities, there are four pairs of quantities of the same kind: c, c'; ρ, ρ'; γ, γ'; and e', E'. These are expressed as four ratios, r_1, r_2, r_3, and r_4, respectively. One member of each of these pairs is a P-quantity if it has not already

been chosen to be an S-quantity. Also any other of the tabulated quantities that has neither been expressed in a ratio nor chosen to be an S-quantity is a P-quantity. The P-quantities are then:

$$\mu,\ \gamma,\ c,\ \delta',\ \text{and}\ E'\ \text{(see table 1)}.$$

The π-products are formed by multiplying the P-quantities by the product of powers of the S-quantities. Each S-quantity is raised to whatever power is required to make the π-product dimensionless. For example, the viscosity μ has the dimensions $M/(LT)$ where M is mass, L is length, and T is time, and, therefore:

$$\pi_1^{-1}=\rho\ d\ V/\mu=(M/L^3)\ (L)\ (L/T)\ (LT/M). \quad (5)$$

Surface tension γ has the dimensions M/T^2 and, therefore,

$$\pi_2^{-1}=\rho\ d\ V^2/\gamma=(M/L^3)\ (L)\ (L^2/T^2)\ (T^2/M). \quad (6)$$

π_3, π_4, and π_5 are formed by a similar procedure. π_1^{-1} and π_2^{-1} are the dimensionless Reynolds Number and the square of the Weber Number, respectively. π_3^{-1} is a kind of Mach Number that gives the ratio of the relative impact velocity between the liquid drop and the solid surface to the speed of sound in the liquid of which the drop is composed.

The damage parameter δ' may be chosen to be a length, a volume, or an area. A length is the easiest quantity to measure experimentally. Taking δ' to be a length, eq (3) for the damage caused by high-speed collision of a solid surface with a liquid drop is

$$\delta'/d=F'[\rho dV/\mu,\ \rho dV^2/\gamma,\ V/c,\ E'/(\rho V^2),\ c'/c,$$

$$\rho'/\rho,\ \gamma'/\gamma,\ e'/E']. \quad (7)$$

It was pointed out in section 2.2 that it will be necessary to develop separate equations to describe the damage produced in liquid-drop-solid-surface collisions for materials that have widely different properties. The damage produced on nonrubbery materials that fail by plastic yield but without fracture is the easiest case to consider. It includes materials such as the soft and medium hard metals. If the collision velocity is not too high, the damage marks produced on these materials by high-speed collision with liquid drops are empty spheroidal segments. Surface and cross-sectional views of such pits in collision experiments performed elsewhere [2] are shown in figures 1, 2, and 3.

The damage pits produced in the planar surface of soft and medium hard metals when the leading surface of the solid runs into a liquid drop at high speed are almost exclusively due to the impact pressure produced. Although the radial flow of the liquid does make a contribution to the damage in the case of the soft metals (it drags metal up the walls of the damage pit and piles it up at the mouth of the crater), this contribution may be small enough in comparison with the damage that is caused by the pressure so that it can be neglected in first approximation. Neglecting all the dimensionless products that result from consideration of the radial flow of the liquid drop and from resilience of the solid target material, the approximate dimensionless damage equation for this class of materials is

$$\delta'/d=F'[\rho'/\rho,\ c'/c,\ V/c,\ E'/(\rho V^2)], \quad (8)$$

where δ' is the depth of the damage pits.

2.4. Experimental Observations

Graphs of measured values of pit depth plotted against relative collision velocity indicate that in the velocity range that has been investigated the pit-depth-versus-velocity curve is very close to a straight line regardless of whether the pits were caused by firing steel spheres against a stationary specimen plate or by firing a specimen plate at high velocity against relatively stationary liquid drops. It is to be expected that at a fixed relative collision velocity the depth of pit caused by a projectile that does not flow during the collision (hardened steel sphere) will be deeper than that caused by a projectile that does flow during the collision (liquid drop). In the first case all of the kinetic energy (neglecting that which is converted into heat) is delivered to the solid target; in the second case part of the kinetic energy is used to produce the flow of the projectile and only the remainder is delivered to the solid target.

Experiments in which 7/32-in. steel spheres were fired against 1/8-in.-thick type-1100 aluminum plates have been carried out by Mr. Herschel L. Smith at the Naval Research Laboratory, Washington, D.C. Some of the data obtained in these experiments are presented in figure 4. One important fact is apparent from these data, namely, for the sphere diameter and for the thickness of specimen plate used, if the specimen plate has only peripheral support the pit-depth-versus-velocity curve has an intercept on the velocity axis, but if the specimen plate is rigidly backed by a heavy steel supporting plate the pit-depth-versus-velocity curve goes directly to the origin.

Experiments in which target plates of different metals were fired into drops of mercury and drops of water at high speed have been carried out in another laboratory.[2] Some of the data obtained are plotted in figures 5 and 6. It can be seen that in every case the pit-depth-versus-velocity curve is essentially a straight line with an intercept on the velocity axis. From the bulge on the trailing face of the specimen in picture 6 of figure 2 it is apparent that the metal plates are supported during the collision with the liquid drops in such a way that the trailing face of the target plate is a free surface. An important fact apparent from the data plotted in figure 6 is that the slope of the straight line is a function of the drop size.

On the basis of the evidence presented, if the specimen has peripheral support only, the pit-depth-

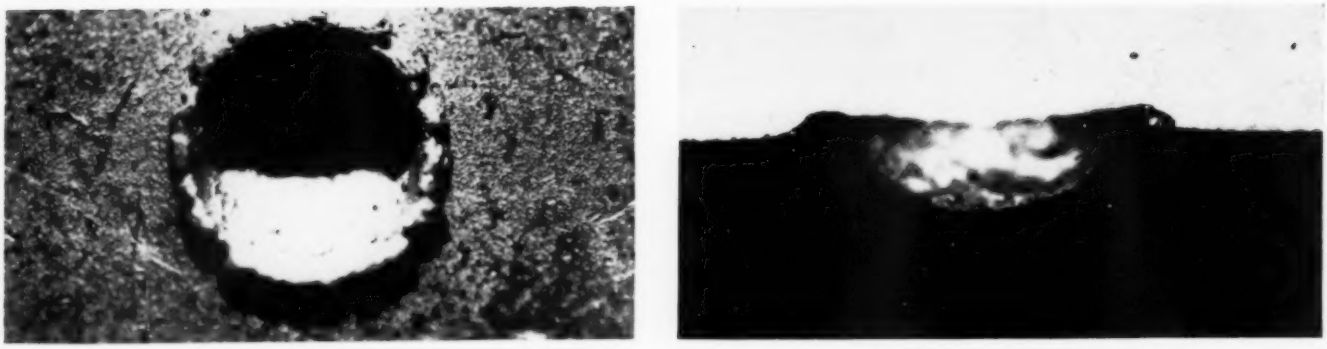

1 SURFACE VIEW 4 CROSS—SECTIONAL VIEW
IMPINGEMENT VELOCITY 686 ft/sec

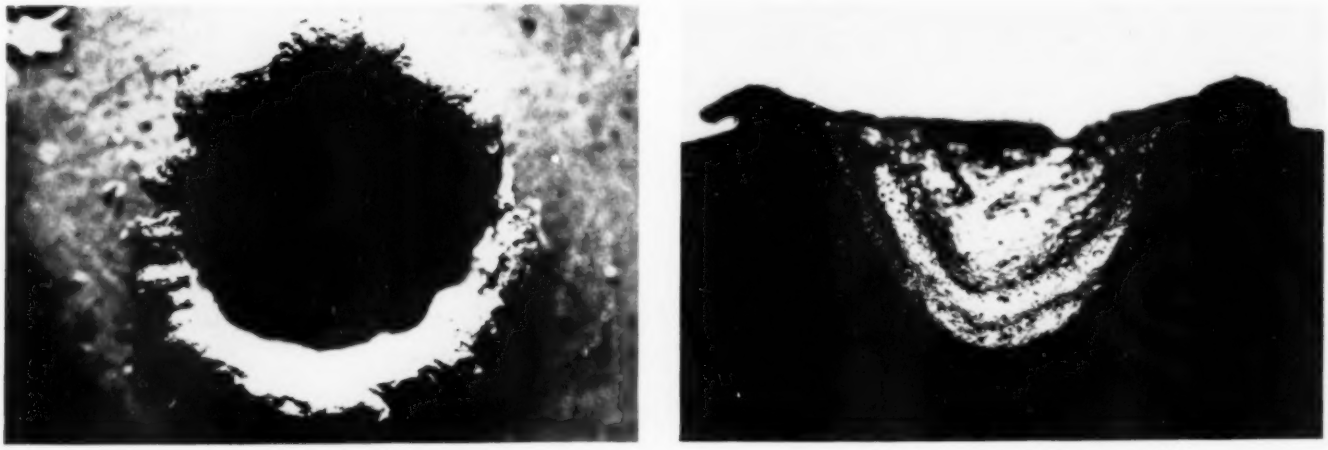

2 SURFACE VIEW 5 CROSS—SECTIONAL VIEW
IMPINGEMENT VELOCITY 1250 ft/sec

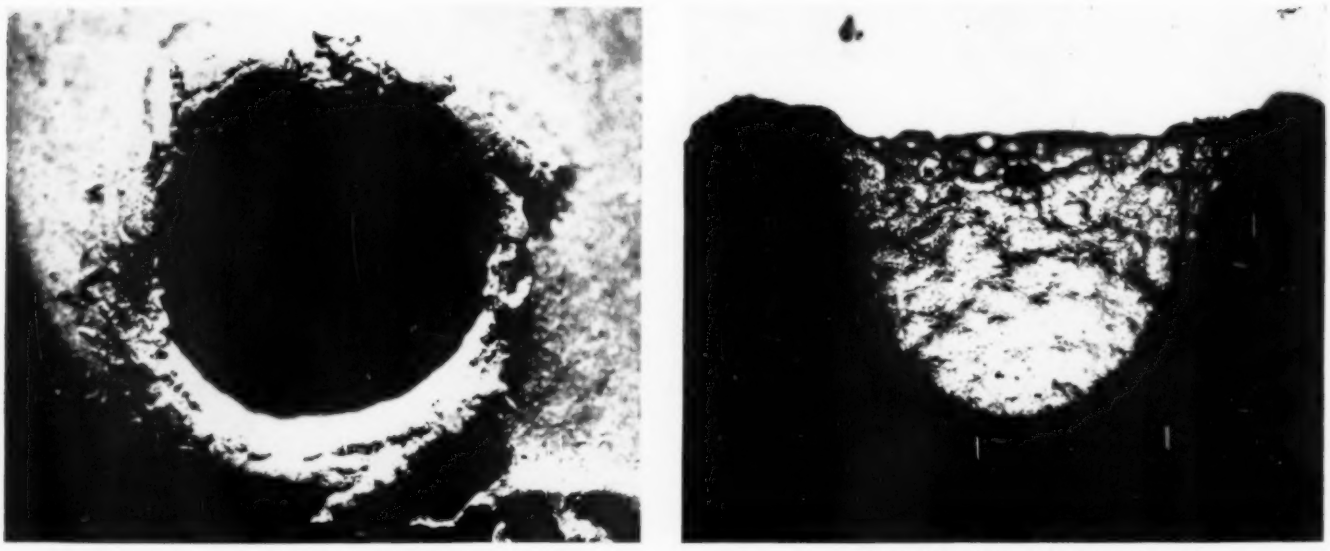

3 SURFACE VIEW 6 CROSS—SECTIONAL VIEW
IMPINGEMENT VELOCITY 1645 ft/sec

FIGURE 1. *Mercury-drop damage pits in lead.*

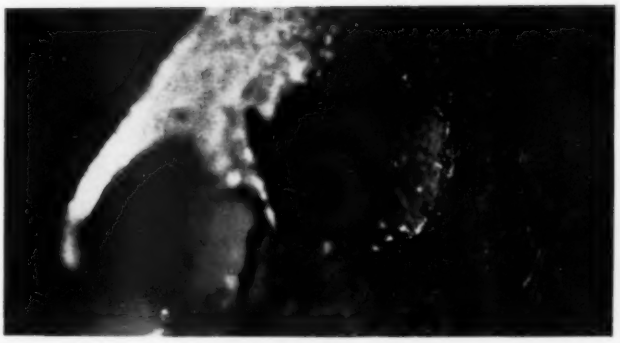

1 SURFACE VIEW

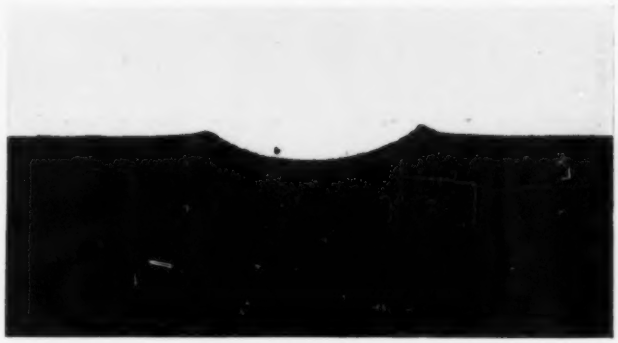

4 CROSS—SECTIONAL VIEW

IMPINGEMENT VELOCITY 686 ft/sec

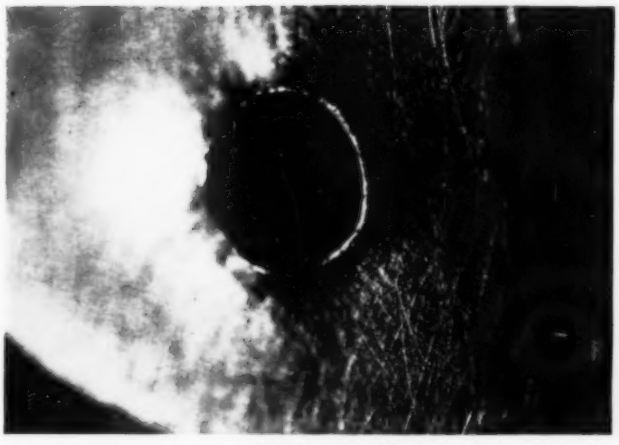

2 SURFACE VIEW

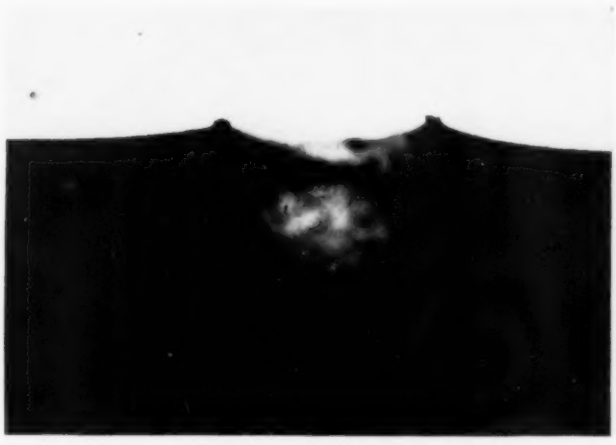

5 CROSS—SECTIONAL VIEW

IMPINGEMENT VELOCITY 1285 ft/sec

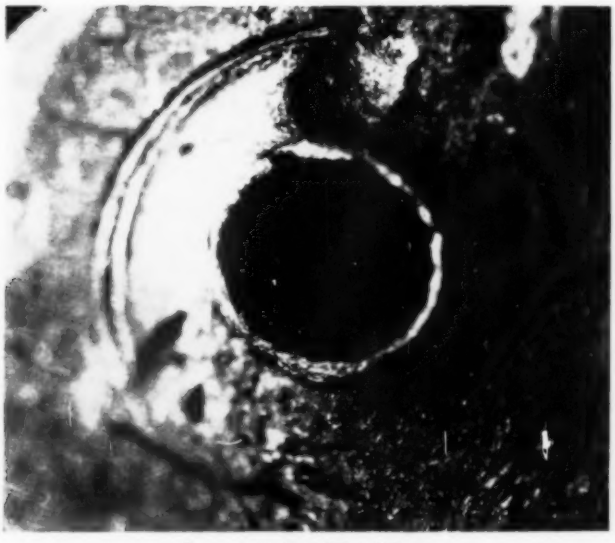

3 SURFACE VIEW

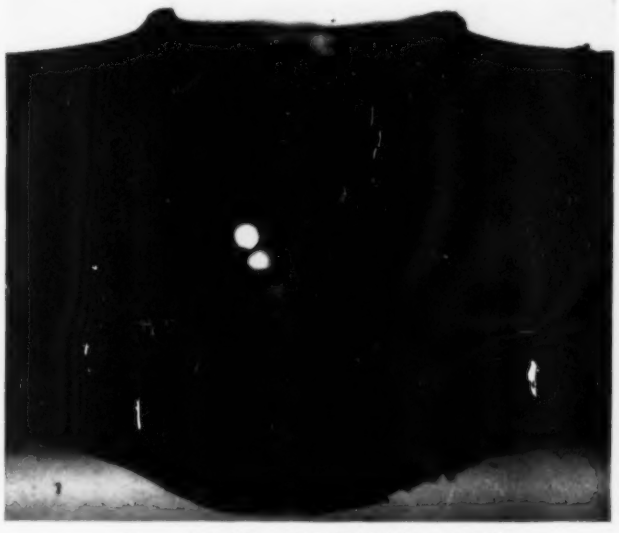

6 CROSS—SECTIONAL VIEW

IMPINGEMENT VELOCITY 2320 ft/sec

FIGURE 2. *Mercury-drop damage pits in 1100 aluminum.*

1 SURFACE VIEW

4 CROSS—SECTIONAL VIEW

IMPINGEMENT VELOCITY 695 ft/sec

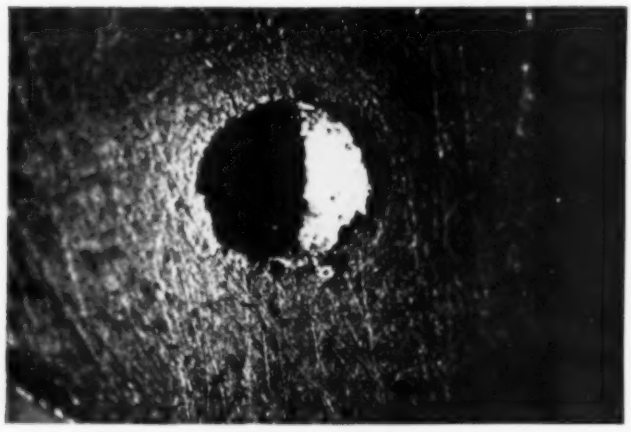

2 SURFACE VIEW

5 CROSS—SECTIONAL VIEW

IMPINGEMENT VELOCITY 1200 ft/sec

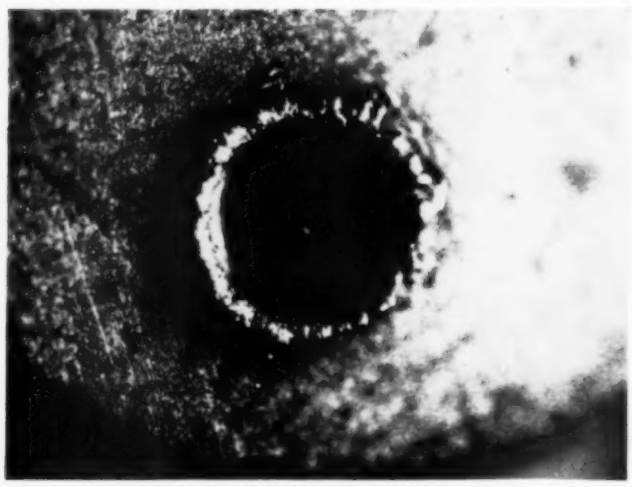

3 SURFACE VIEW

6 CROSS—SECTIONAL VIEW

IMPINGEMENT VELOCITY 2445 ft/sec

FIGURE 3. *Mercury-drop damage pits in copper*

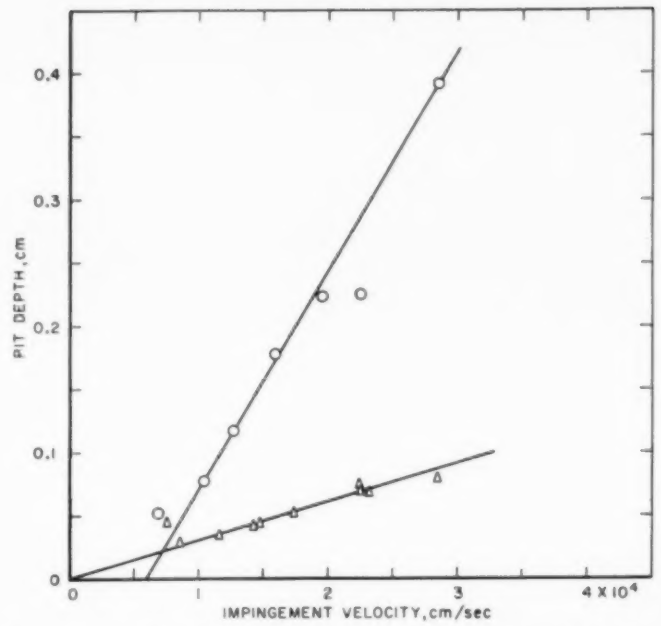

FIGURE 4. *Best-fit curves for collisions of 0.55-cm steel spheres against plates of 1100 aluminum.*

⊙ aluminum plate with edge support only; △ aluminum plate rigidly clamped to heavy steel plate.

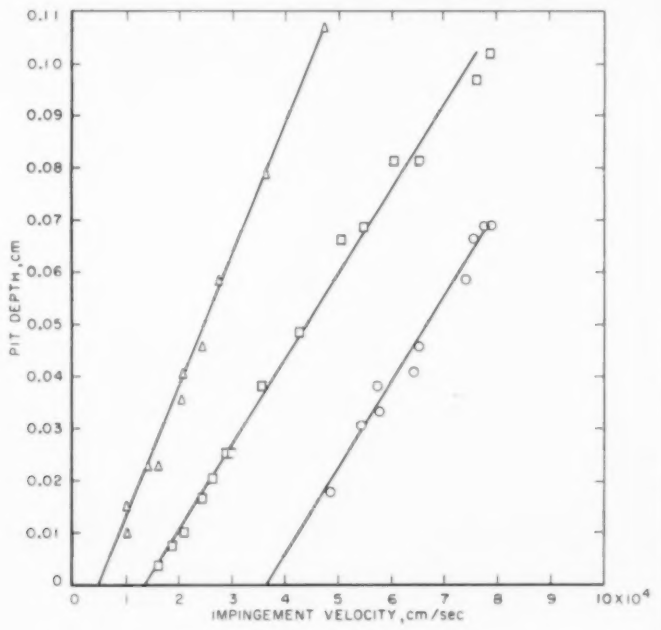

FIGURE 5. *Best-fit curves for collisions of mercury drops against plates of three different metals.*

△ 0.10-cm mercury drops against lead; ⊡ 0.10-cm mercury drops against copper; ⊙ 0.15-cm mercury drops against iron.

versus-velocity equation for materials of the response type being considered appears to be:

$$\delta' = K_1 V - K_2, \tag{9}$$

where K_1 and K_2 are constants.[5] It appears that

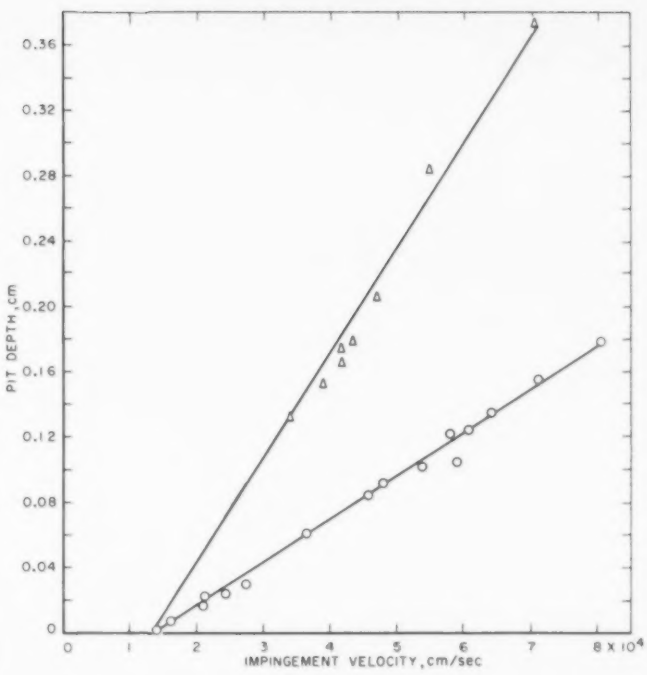

FIGURE 6. *Best-fit curves for collisions of mercury drops of two sizes against plates of 1100 aluminum.*

⊙ 0.10-cm mercury drops; △ 0.20-cm mercury drops.

this equation applies regardless of whether the pits are produced by the impingement of solid projectiles against solid targets or by firing solid target plates into liquid drops at very high velocities. However, because the amount of the kinetic energy delivered to the target depends upon whether or not the projectile flows during the collision, the constants K_1 and K_2 will be different for solid-target-versus-solid-projectile and for solid-target-versus-liquid-projectile collisions.

2.5. Pit-Depth-Versus-Velocity Equation for Medium-Thin Metal Targets

For targets that are metal plates, that have a thickness several times the diameter of the projectile, and that are mounted so that the reverse side of the plate is a free surface, a pit-depth-versus-velocity equation can be developed by considering the movement of a cylindrical core of material through the target plate under the area of contact involved during the collision. If the target plate is fired against the projectile, this core of target material is slowed down with respect to the remainder of the target plate as a result of the collision and there is a relative motion between this core and the remainder of the target plate, which moves forward with respect to it.

[5] Partridge, VanFleet, and Whited [11] also reported a linear relationship between pit depth and velocity; the linear relationship was established independently by the author on the basis of the Convair data.

If the reverse side of the target plate is a free surface and the core can move *freely* with respect to the remainder of the plate, the kinetic energy transformed as a result of the collision is largely converted into the work of moving the core against the bonding that holds it to the remainder of the target plate. For these conditions there is an intercept on the velocity axis. In terms of this model, it would appear that the intercept velocity is related to the shear yield strength of the material of the target plate. In the range of velocities that are just in excess of the threshold velocity required to produce any permanent damage at all (intercept velocity), it appears that the core may only be displaced with respect to the remainder of the target plate. For this case plastic deformation occurs only at the cylindrical boundary of the core. At higher velocities plastic deformation may occur within the core itself.

Consider that a small target plate moving at velocity V in a stationary coordinate system, which is located outside of the target plate, strikes a stationary liquid drop (see fig. 7). The result of the collision is that a wave of compression is initiated both in the solid material of the target plate and in the liquid of the drop. It is helpful to view the collision incident as it is seen by an observer located at the origin of the coordinate system in figure 7. This observer sees a target plate, all parts of which are moving forward uniformly at velocity V in the $(+y)$-direction, approach a spherical drop, all parts of which are stationary. After the collision has occurred, the observer sees a zone in which the particles of the material of the target plate have taken on a velocity, aV, in the $(-y)$-direction where a is a constant; this zone is indicated schematically with a dotted line and the letter A in figure 7. Similarly, the observer sees a zone in the liquid drop in which the particles of the liquid have taken on a velocity, bV, in the $(+y)$-direction where b is a different constant; this zone is indicated schematically with a dotted line and the letter B in figure 7. Zone A spreads at the characteristic sound velocity of the target material, c', through the thickness, d', of the target plate and zone B spreads at the characteristic sound velocity, c, of the liquid of which the drop is composed, through the diameter, d, of the liquid drop.

To the observer who looks first at a point A' that is in the target plate but outside the spreading boundary of zone A and who then looks at the material within zone A, it appears that the particles at A' have a velocity V and that the particles in zone A have a velocity $(1-a)V$. After a time t that is just long enough for zone A to complete one trip through the thickness of the target plate, the leading surface of the target plate at point A' in figure 7 has advanced a distance Vt, but in the same time t the area of the leading surface of the target plate that constitutes the upper boundary of zone A in figure 7, has advanced only by $(1-a)Vt$. If the average negative velocity of the core is taken to be $aV/2$, the displacement that exists between the leading surface of the target plate at point A' and the upper boundary of zone A after time t is $aVt/2$.

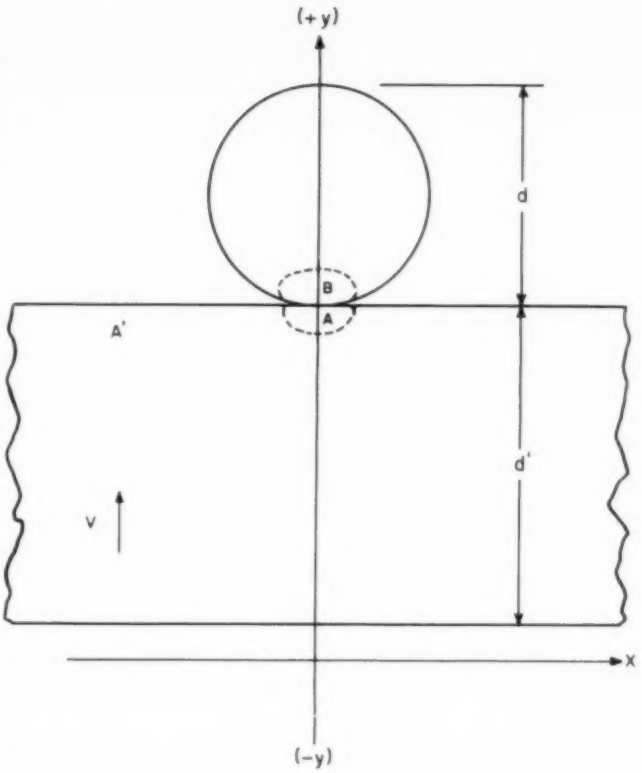

FIGURE 7. *Stationary coordinate system for a liquid-drop-versus-solid-specimen collision.*

If the observer watches zone B as it just spreads to the opposite side of the liquid drop, he sees that this zone reflects from the free air-liquid interface with change of sign, that is, he sees a tension wave begin to move toward him in the $(-y)$-direction of figure 7. Within the tension wave the particle velocity is $2bV$ in the $(+y)$-direction. The tension wave moves toward the observer at the characteristic speed of sound, c, of the liquid of which the drop is composed. In the zone of the liquid of the drop that has been traversed by the tension wave the particles of the liquid are unstressed and are moving at velocity $2bV$ in the $(+y)$-direction. At the instant that the tension wave returns to the collision surface, where radial flow of the liquid of the drop is occurring, all of the liquid of the drop is unstressed and moving at the velocity $2bV$ in the $(+y)$-direction.

It can be assumed that return to the collision surface of the tensile wave in the liquid provides a cutoff for the collision. At this instant all of the liquid of the drop is unstressed. The collision surface will appear to be a free surface to the compressed particles of the material of the target plate in zone A. A wave of relief (tension) will then be initiated in the material of the target plate and will begin to trail zone A which continues to spread through the thickness, d', of the target plate.

Let the arbitrary time t referred to previously now be the time that is required for zone B to make one round trip through the liquid drop. Then $t=2d/c$. The distance to which zone A has spread in this time is $c't$ and this determines the length of the compressed zone A which continues to move through the target plate. When zone A reaches the free trailing surface of the target plate, it also reflects as a tension wave. This tension wave moves in the $(+y)$-direction of figure 7. In that part of zone A that has been traversed by the returning tension wave the particles of the material of the target plate are under zero stress and have velocity $(1-2a)V$ in the $(+y)$-direction. When the reflected tension wave in the target plate reaches the leading surface of the plate it undergoes partial reflection back into the material of the target plate and partial transmission into the liquid of the drop which is running off radially around the central point of the collision.

a. Slope of the Pit-Depth-Versus-Velocity Curve

The compressional wave spreads slightly as it moves through the thickness of the target plate; consequently, the core of material through the target plate that is slowed down as a result of the collision is in reality somewhat conical in shape. For simplicity, the true situation may be idealized in two ways. First, the core may be regarded as a true cylinder which is free to move or slide in the direction of the collision blow but which is restrained laterally. A similar cylinder exists in the liquid of which the drop is composed. Secondly, the compressional waves that move through the cylinder in the target plate and through the cylinder in the drop may be regarded as plane waves.

For the case of plane waves, $a=z/(z+z')$ and $b=z'/(z+z')$ where $z=c\rho$ and $z'=c'\rho'$ are the acoustic impedances of the material of the drop and of the material of the target plate, respectively. The relations are found by equating the plane-wave stress in the material of the drop, σ, to the plane-wave stress in the material of the target plate, σ', that is,

$$\sigma=c\rho v=c'\rho'v'=\sigma', \tag{10}$$

where v, v' are the particle velocities in the zones traversed by the compressional waves initiated in the drop and in the target plate, respectively, and by imposing the condition that the impacting surfaces remain in contact, namely,

$$v+v'=V. \tag{11}$$

From eq (10) and (11),

$$\begin{aligned} v'&=c\rho V/(c\rho+c'\rho') \\ &=zV/(z+z') \\ &=aV \end{aligned}$$

and

$$\begin{aligned} v&=z'V/(z+z') \\ &=bV. \end{aligned} \tag{12}$$

This derivation is the same as that for the collision of two free rods except that, for the case that the rods are cylinders that are free to move in the collision direction but that are restrained laterally, the sound speed that must be used is the speed of sound in an infinite medium. This can be shown as follows.[6] According to Hooke's law:

$$E\epsilon_l=\sigma_l-\nu(2\sigma_r)=\sigma_l-2\nu\sigma_r, \tag{13}$$

where E is Young's modulus, ϵ_l is the longitudinal strain, σ_l is the longitudinal stress, ν is Poisson's ratio, and σ_r is the radial stress. Also,

$$E\epsilon_r=\sigma_r-\nu(\sigma_l+\sigma_r)=0, \tag{14}$$

where ϵ_r is the radial strain. From eq (14),

$$\sigma_r=\nu\sigma_l/(1-\nu). \tag{15}$$

By substituting the expression for σ_r given by eq (15) into eq (13) it is found that

$$\sigma_l=\frac{(1-\nu)E\epsilon_l}{(1-2\nu)(1+\nu)}, \tag{16}$$

and because, for plane waves, $c=[\sigma_l/\rho\epsilon_l]^{1/2}$

$$c=\left[\frac{(1-\nu)}{(1-2\nu)(1+\nu)}\ \frac{E}{\rho}\right]^{1/2}. \tag{17}$$

This is the sound speed for an infinite medium and it is the sound speed that must be used both for c and for c' in the expressions for a and for b.

The depth of pit produced at any relative impingement velocity is proportional to the negative velocity produced in the cylindrical core in the target plate as a result of the collision and to the time that this negative velocity exists. If it is assumed that the elastic wave that is induced in the cylindrical core as a result of the collision makes a round trip through the core in the time interval $2d/c$, then, at the end of this time interval, the cylindrical core is moving as a rigid body and the negative velocity that it has acquired with respect to the remainder of the target plate is given approximately by $2zV/(z+z')$. During this time interval the average negative velocity given to the material of the cylindrical core was $zV/(z+z')$. The slope K_1 of eq (9) is then $k_1(2d/c)\ [z/(z+z')]$ where k_1 is a new constant.

The experimental data for a number of target metals of widely different properties fired against drops of mercury, and for three target metals fired both against drops of mercury and drops of water, require that $k_1=3.6$. Because this value of the constant k_1 brings the calculated curve into good agreement with the experimental data for a number of target metals and for two drop liquids, it would appear that k_1 does not involve properties either of

[6] The author is indebted to Dr. John M. Frankland of NBS Mechanics Section for the proof in elasticity theory that it is the sound speed in infinite medium that is required.

the material of the target plate or of the liquid of the drop. Therefore, eq (9) is

$$\delta' = 7.2d\left(\frac{z}{z+z'}\right)\left(\frac{V}{c}\right) - K_2. \tag{18}$$

Substitution of $z = c\rho$, $z' = c'\rho'$, and division by d puts eq (18) in the dimensionless form

$$\frac{\delta'}{d} = \frac{7.2}{1+\left(\frac{c'}{c}\right)\left(\frac{\rho'}{\rho}\right)}\left(\frac{V}{c}\right) - K_2/d, \tag{19}$$

where K_2/d is a dimensionless intercept. Four of the dimensionless quotients predicted by eq (8) are found in eq (19).

b. Intercept on the Velocity Axis

The process previously postulated, namely, that the core of target material below the collision area is slowed down with respect to the remainder of the target plate so that the remainder of the target plate moves forward with respect to it, certainly occurs at all impingement velocities. However, no observable damage pit is produced at all below a critical velocity, and, if the liquid of the drop is kept constant, this critical velocity is different for each of the metals for which data are available. (See fig. 5.) The intercept velocity is also different on the same metal if the liquid of the drop is changed.

The fact that no permanent damage pit is formed below a given velocity which is characteristic for each metal, indicates that for velocities lower than this critical velocity the relative motion between the core and the remainder of the target plate is completely elastic and that no permanent shear deformation occurs in the material around the cylindrical wall of the core. The intercept of the pit-depth-versus-velocity curve appears to be a function of the shear yield strength of the material, that is, of the remaining dimensionless quotient $E'/(\rho V^2)$ of eq (8) taking E', the energy per unit volume absorbed by the target material without fracture or plastic yield, to be the shear yield strength.

It has been pointed out that the experimental pit-depth-versus-velocity curve is a straight-line function of the velocity. Therefore, the dimensionless quotient $E'/(\rho V^2)$ cannot be used for the intercept without eliminating the factor $1/V^2$. This can be accomplished by multiplying the dimensionless quotient $E'/(\rho V^2)$ by the square of the dimensionless quotient V/c of eq (8) to obtain $E'/(\rho c^2)$. If this expression is substituted for the dimensionless intercept K_2/d in eq (19) and if the intercept condition that $\delta'/d = 0$ is imposed, the expression that is found for the intercept velocity is not able to account for the observed ratio of experimental intercepts. It was found that the observed intercept velocities can be accounted for if the dimensionless quotient $E'/(\rho c^2)$ is multiplied by the dimensionless quotients $(\rho/\rho')^{1/2}$, z/z', c/c', and by a dimensionless numerical constant, k_2, having the value 136.8. Substitution of the resulting dimensionless quotient, $136.8\,E'z/(\rho^{1/2}\rho'^{1/2}cc'z')$, for the dimensionless intercept, K_2/d, in eq (19) and use of the acoustic impedance z for $c\rho$ produces the dimensionless pit-depth equation

$$\frac{\delta'}{d} = \frac{7.2z}{z+z'}\left(\frac{V}{c}\right) - \frac{136.8E'z}{\rho^{1/2}\rho'^{1/2}cc'z'}. \tag{20}$$

If the intercept condition that $\delta'/d = 0$ is imposed, the intercept velocity, V_i, is found to be given by

$$V_i = \frac{19E'(z+z')}{(\rho c'z'^3)^{1/2}}. \tag{21}$$

It is noteworthy that one would expect V_i to be given by $E'(z+z')/zz'$ multiplied by some constant, because the plane wave stress is given by $zz'V/(z+z')$. It was found, however, that this expected expression would not give the observed intercept velocities for both mercury drops and waterdrops if the same numerical constant was used for both drop liquids. Equation (21) appears at present to be the best expression for the intercept velocity. When more data are obtained and the problem is studied further, it may be found necessary to change it.

The numerical constants in eqs (20) and (21) have been chosen to give best fit to the pit-depth-versus-velocity data. The values used for the physical constants of the different materials are given in table 2. In choosing the constants, the speed of sound in infinite medium was used for c' and the dynamic compressive yield strength was used for E'. (In liquids there is only one speed of sound that can be used for c.) Dynamic rather than static strength values must be used for E' because the loading time is of the order of several microseconds. The strength that should be used for E' is the dynamic yield strength in shear. Unfortunately, the amount of work that has been done in determining the dynamic yield strengths of materials is very limited. Whiffin [7] has determined the dynamic yield strength in compression for a number of materials. In choosing the numerical constant for eq (21), the dynamic yield strength in compression was used for E' instead of the dynamic yield strength in shear. Some justification for this substitution may be found in the Von Mises strain energy theory according to which the tensile elastic limit, σ_y, is $\sqrt{3}\ \tau_y$ where τ_y is the yield strength in shear.

2.6. Test of the Equation

For pit-depth calculations, eq (20) may be put in the form

$$\delta' = \frac{7.2\ d\ z}{c(z+z')}\,[V - V_i], \tag{22}$$

where V_i is the intercept velocity for the particular liquid-drop-solid-target combination being used and where V_i is given by eq (21). Pit-depth-versus-velocity data obtained in another laboratory[2] were used to test the equations. In most cases the

TABLE 2. *Physical Constants*

Metal	Density, ρ	Sound speed, c (infinite medium)	Acoustic impedance, z	Static tensile yield strength, Y	Dynamic compressive yield strength, E'
	g/cm³	*cm/sec*	*g/sec·cm²*	*psi*	*d/cm²*
1100–0 aluminum	[a] 2.713	[d] 6.318×10^5	1.714×10^6	[f] 2,625 [e] 5,000	[g] 7.239×10^8 [h] 1.183×10^9
2024–0 aluminum	[a] 2.768	[d] 6.370×10^5	1.763×10^6	[f] 12,625	[g] 2.350×10^9
Copper, annealed electrolytic tough pitch	[b] 8.92	[d] 4.691×10^5	4.184×10^6	[f] 3,975	[h] 2.394×10^9
Lead, chemical	[b] 11.3437	[d] 2.277×10^5	2.583×10^6		[h] 4.324×10^8
Lead, pig		[d] 2.128×10^5	2.414×10^6		
Steel, cold rolled	[c] 7.859	[d] 5.786×10^5	4.547×10^6		[i] 8.274×10^9
Iron	[b] 7.86	[e] 5.850×10^5	4.598×10^6		[h] 7.660×10^9
Zinc	[b] 7.14	[e] 4.170×10^5	2.977×10^6		
Mercury	[b] 13.546	[e] 1.451×10^5	1.966×10^6		
Water, 25° C	[b] 0.99707	[e] 1.497×10^5	0.1493×10^6		

[a] Data from Aluminum Co. of America.
[b] Data from Handbook of Chemistry and Physics.
[c] Data from Metals Handbook, 1948.
[d] Measured in NBS Sound Section by Carroll Tschiegg.
[e] Data from L. Bergmann [12].
[f] Measured in NBS Engineering Mechanics Section by Lafayette K. Irwin.
[g] Data of A. C. Whiffin, communicated by letter.
[h] Data of A. C. Whiffin [7].
[i] Extrapolated from graph, figure 7e, given by Krafft and Sullivan [9].

physical properties of the metals used in the experiments were not determined. The physical constants used for these materials in eqs (21) and (22) are given in table 2.

a. Test of the Equation With Mercury Drops and Pure Metal Targets

Pit-depth-versus-velocity curves calculated by eq (22) for collisions of 0.10- and 0.15-cm mercury drops against copper are shown in figure 8. Experimental points for the two drop sizes are indicated in this figure with circles and with triangles, respectively. The material used in these experiments[2] was described as pure copper. Physical constants for electrolytic copper were used in the calculations. The intercept velocity, V_i, was calculated by use of eq (21). It can be seen that both the slope and intercept of the calculated curves are in good agreement with the experimental data.

Pit-depth-versus-velocity curves calculated by use of eq (22) for collisions of 0.10-, 0.15-, and 0.285-cm mercury drops against 1100-0 aluminum are shown in figure 9. Experimental points for the three drop sizes that were used are indicated in this figure with circles, triangles, and squares, respectively. The intercept velocity, V_i, was calculated by use of eq (21). The value of the dynamic compressive yield strength that was used for E' in eq (21) was calculated by means of a formula given by Whiffin [7] for the Duralumins. The static yield strength of the 1100–0 aluminum used was not known.[2] For the purpose of the calculation of E' it was taken to be 5,000 psi (table 2). The speed of sound in infinite medium, determined for a piece of 1100–0 aluminum of lower yield strength by Tschiegg (table 2) was used for c' and in computing z'. There is more scatter in the experimental data for the 0.15-cm drop size than for the other two drop sizes. Scatter could be caused by variation of the drop size from the reported value; it could also be caused by use of target plates cut from sheet material of different yield strength. The data for both the 0.15-cm and 0.285-cm drop sizes would fit the curves better if the intercept velocity were 1.1×10^4 cm/sec rather than 1.26×10^4 cm/sec, which was the value found by use of eq (21). The experimenters report [8] that the target plates were cut from 1100-aluminum sheets having thicknesses in the range of 0.185 to 0.210 in.; hence, they were not all cut from the same sheet stock and, consequently, some variation in yield strength, which would affect the intercept velocity directly, could have been present. In general, however, there is good agreement between the experimental data and the calculated curves.

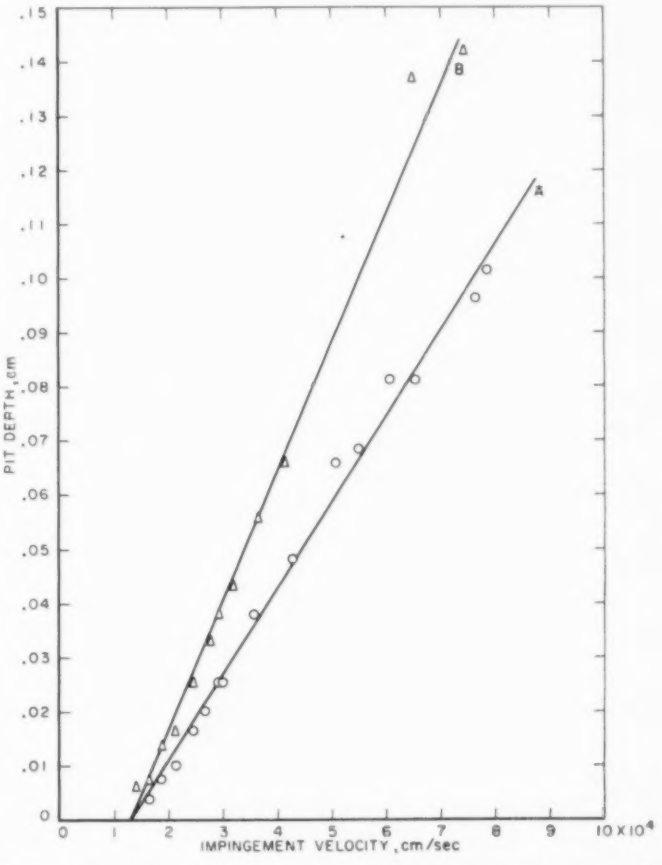

FIGURE 8. *Calculated curves for collisions of mercury drops of two sizes against plates of copper.*

⊙ observed depth for 0.10-cm drop; A, calculated curve for 0.10-cm drop; △ observed depth for 0.15-cm drop; B, calculated curve for 0.15-cm drop.

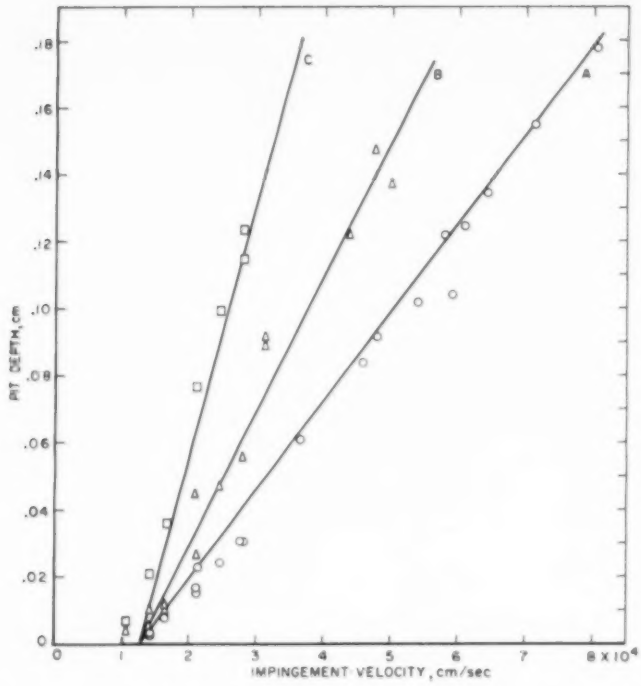

FIGURE 9. *Calculated curves for collisions of mercury drops of three sizes against plates of 1100 aluminum.*

⊙ observed depth for 0.10-cm drop; A, calculated curve for 0.10-cm drop; ▽△ observed depth for 0.15-cm drop; B, calculated curve for 0.15-cm drop; ⊡ observed depth for 0.285-cm drop; C, calculated curve for 0.285-cm drop.

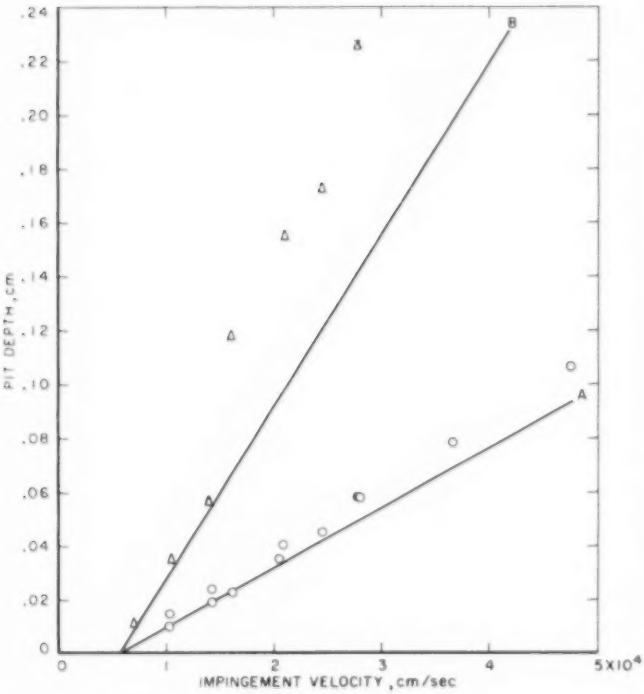

FIGURE 10. *Calculated curves for collisions of mercury drops of two sizes against lead target plates.*

⊙ observed depth for 0.10-cm drop; A, calculated curve for 0.10-cm drop; △ observed depth for 0.285-cm drop; B, calculated curve for 0.285-cm drop.

The pit-depth-versus-velocity curves calculated by use of eq (22) for collisions of 0.10-cm and for 0.285-cm mercury drops against lead are shown in figure 10. The experimental points for the two drop sizes are indicated with circles and with triangles, respectively. The intercept velocity, V_i, was calculated by use of eq (21). The value of the dynamic compressive yield strength used for E' in eq (21) was that given for 99.97 percent lead by Whiffin (table 2). The value of the speed of sound in infinite medium for pig lead measured by Tschiegg (table 2) was used for c' and in computing z'. The calculated curves are a good fit to the data at the lower velocities; at the higher velocities the depth of the pits is greater than that predicted by eq (22). The pits produced in lead by mercury drops are characterized by a heavier lip of metal around the mouth of the crater than is observed on pits in 1100–0 aluminum or on pits in copper. See figures 1, 2, and 3. It appears that for a metal that is as soft as lead the flow of a liquid-drop projectile at high collision velocities drags a notable amount of metal from the bottom of the pit and piles it up at the mouth of the crater. This extra mode of pit formation was neglected in the development of eq (22) and, therefore, this equation does not fully account for the depth of pits formed at very high velocities in metals as soft as lead.

b. Test of the Equation With Mercury Drops and Alloy Metal Targets

Experimental pit-depth-versus-velocity data were obtained for collisions of 0.15-cm mercury drops with steel targets in another laboratory.[2] It was reported that the target material was originally ¾H cold-rolled steel. After annealing above the alpha temperature it developed a case hardening. The case hardening was chipped off and the target plates were polished. It was reported that the resulting material had an average Rockwell E hardness of 90.96 and Brinell hardness of 90.98, which they stated corresponds to an ultimate tensile strength of 47,200 psi.

In order to calculate the intercept velocity by means of eq (21) it is necessary to know the dynamic compressive yield strength of the target metal. The manganese and carbon contents of steels strongly affect their dynamic yield strength; the manganese content is particularly important if it is low, for example, in the range from zero to 0.50 percent. A chemical analysis of the manganese and carbon content of one of the steel target plates was made in the NBS Analytical Chemistry Section. It revealed that the steel contained 0.70 percent manganese and 0.21 percent carbon. The value of the dynamic compressive yield strength used for E' in eq (21) was found by extrapolating a curve given by Krafft and Sullivan [9] for a steel containing 0.98 percent manganese and 0.22 percent carbon that was loaded in compression. The speed of sound in infinite medium determined for cold-rolled steel by Tschiegg (table 2) was used for c' and in computing z'.

The pit-depth-versus-velocity curve calculated by use of eqs (21) and (22) for collisions of 0.15-cm mercury drops against steel targets is shown in figure 11 along with the experimental points. It would appear that the intercept velocity is about correct. However, a straight line that would fit the experimental data would have a slope considerably less than that of the calculated curve. It would appear from this evidence that eq (22) does not predict pit depth with exactness for pits formed in targets of alloy steel.

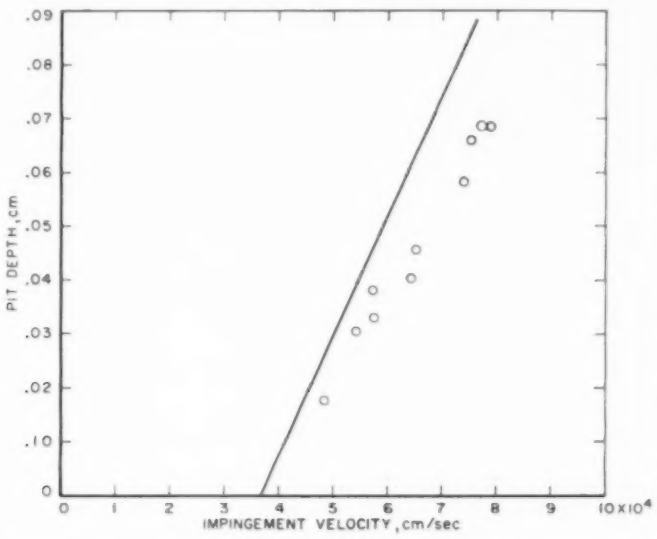

FIGURE 11. *Calculated curve for collisions of 0.15-cm mercury drops against steel.*

⊙ observed depth for 0.15-cm drop.

The pit-depth-versus-velocity curves calculated by use of eqs (21) and (22) for collisions of 0.10-cm and 0.20-cm mercury drops against 2024–0 aluminum targets are shown in figure 12 along with experimental points obtained elsewhere.[2] The experimental points for the two drop sizes are indicated with circles and triangles, respectively. The targets were prepared at the NBS. The average static yield strength (0.2% offset) of the metal used was found to be 12,625 psi from measurements made by Irwin (table 2). The dynamic compressive yield strength used for E' in eq (21) for this material was calculated from a ratio of the static to the dynamic yield strength of 2.7. This ratio was estimated by Whiffin [10] for the 2024–0 aluminum that was used for the targets. The speed of sound in infinite medium determined for 2024–0 aluminum by Tschiegg (table 2) was used for c' and in computing z'. The calculated curves differ from a best-fit line drawn through the experimental points in intercept but not in slope. If the intercept velocity had been $2\text{x}10^4$ cm/sec rather than $2.421\text{x}10^4$ cm/sec there would have been relatively good fit between the calculated curves and the experimental points.

In summarizing, it can be said that eqs (21) and (22) have not given calculated curves that show as

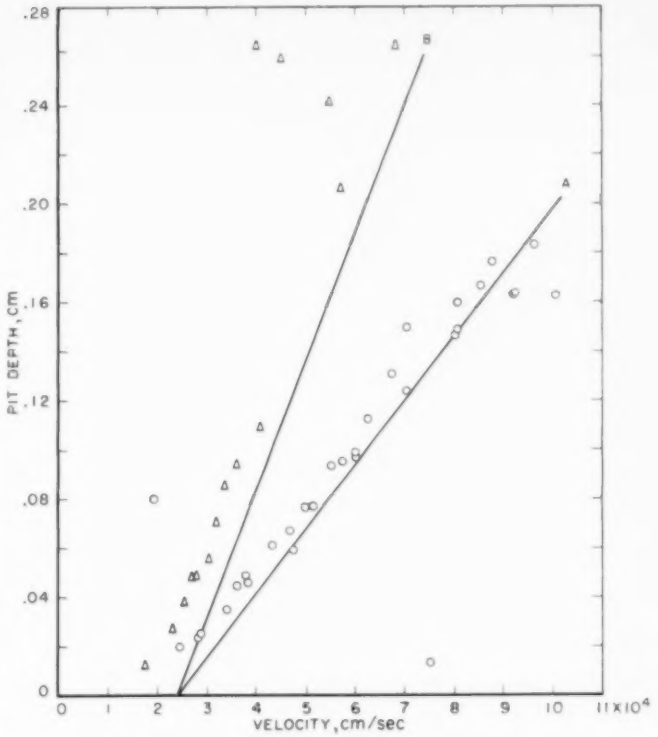

FIGURE 12. *Calculated curves for collisions of mercury drops of two sizes against target plates of 2024–0 aluminum.*

⊙ observed depth for 0.10-cm drop.
A, calculated curve for 0.10-cm drop.
△ observed depth for 0.20-cm drop.
B, calculated curve for 0.20-cm drop.

good agreement with experimentally determined points for collisions of target plates of alloy metals with mercury drops as that obtained for collisions of plates of pure metals with mercury drops.

c. Tests of the Equation With Waterdrops

Test results with waterdrops of constant size are available for some of the metals used in the experiments with mercury drops.

The pit-depth-versus-velocity curve calculated by use of eqs (21) and (22) for collisions of 0.2-cm waterdrops against targets of annealed electrolytic tough pitch copper is shown in figure 13 along with experimental points obtained elsewhere.[2] The targets were prepared at the NBS. The static yield strength (0.2% offset) of the metal used was determined by Irwin; the average value was 3,975 psi. The dynamic compressive yield strength used for E' in eq (21) was that given by Whiffin (table 2) for electrolytic copper. The speed of sound in infinite medium determined for electrolytic tough pitch copper by Tschiegg (table 2) was used for c' and in computing z'. There is quite a bit of scatter in the data plotted in figure 13. However, both the slope and intercept of the calculated line are in relatively good agreement with these data.

The pit-depth-versus-velocity curve calculated by use of eqs (21) and (22) for collisions of 0.2-cm waterdrops against targets of 2024–0 aluminum is

shown in figure 14 with experimental points obtained elsewhere.[2] The targets were prepared at the NBS. They were made of the same 2024 aluminum as the targets that were used for collisions with mercury drops (see sec. 2.6b and fig. 12), and the same values of E', c', and z' were used in calculating the pit-depth-versus-velocity curve. It can be seen from figure 14 that the calculated line fits the experimental points fairly well.

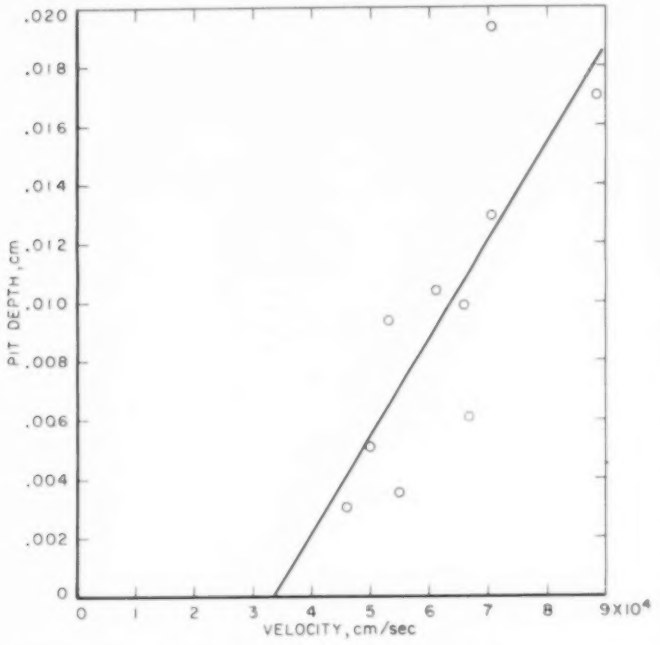

FIGURE 13. *Calculated curve for collisions of 0.20-cm waterdrops against target plates of electrolytic tough pitch copper.*

⊙ observed depth for 0.20-cm drop.

The pit-depth-versus-velocity curve calculated by use of eqs (21) and (22) for collisions of 0.2-cm waterdrops against lead targets is shown in figure 15. The experimental points shown in the graph were obtained elsewhere.[2] The kind of lead that was used for the targets is not known. The dynamic yield strength used for E' was that given by Whiffin (table 2) for 99.97 percent pure lead. The speed of sound in infinite medium for pig lead determined by Tschiegg was used for c' and in computing z'.

The amount of agreement that has been found between the calculated curves and experimental points for collisions of both mercury drops and waterdrops with targets of copper, 2024–0 aluminum, and lead may be favorable evidence for the possible usefulness of eq (22) in predicting corresponding velocities-for-equal-pit-depth for collisions of metal target plates with waterdrops and with mercury drops.

2.7. Corresponding Velocities-for-Equal-Pit-Depth

From the standpoint of the problem of high-speed rain erosion, the practical value of an equation giving the depth of damage pits as a function of impingement velocity is its use to extrapolate from the known depth of pit produced by collision of a solid target with a drop of high-density liquid at a relatively low impingement velocity to the depth of pit that would be produced on the same target material by collision with a drop of low-density liquid, such as water, at a very much higher impingement velocity. The purpose of carrying out this extrapolation is to bypass the necessity of firing target materials at the extremely high velocities for which test results are desired for collisions of solids with waterdrops.

If drops of a liquid A having diameter d_A collide with a solid material having acoustic impedance z' and dynamic yield strength E', eq (22) predicts that the pit depth will be

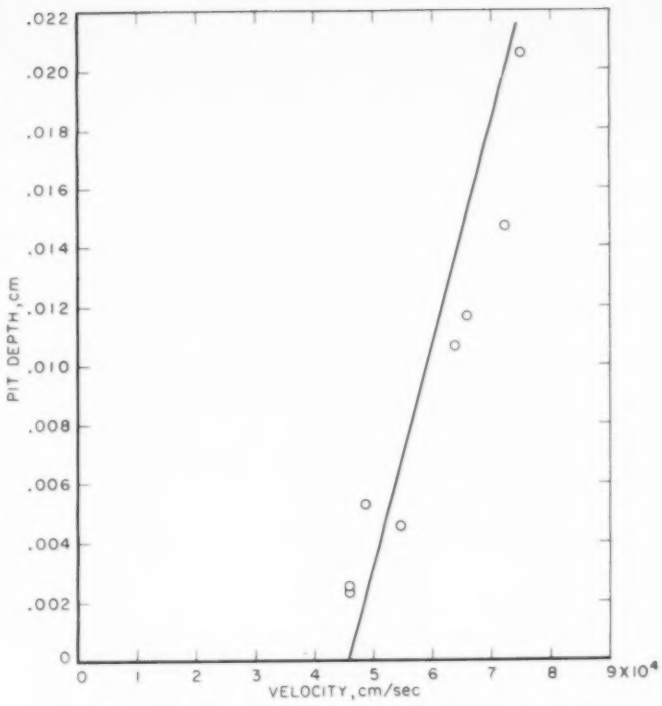

FIGURE 14. *Calculated curve for collisions of 0.20-cm waterdrops against target plates of 2024–0 aluminum.*

⊙ observed depth for 0.20-cm drop.

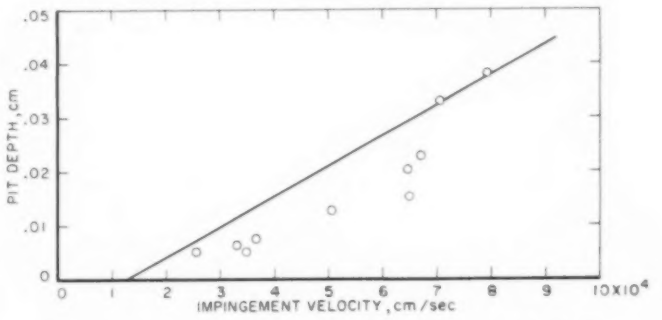

FIGURE 15. *Calculated curve for collisions of 0.20-cm waterdrops against target plates of lead.*

⊙ observed depth for 0.20-cm drop.

$$\delta_A' = \frac{7.2 d_A z_A}{c_A(z_A + z')}[V_A - V_{tA}], \quad (23)$$

where V_{tA} is the intercept velocity calculated with use of eq (21) and with use of the density and acoustic impedance of liquid A for ρ and z, respectively. The depth of pits resulting from collisions of drops of liquid B with the same solid material will be

$$\delta_B' = \frac{7.2 d_B z_B}{c_B(z_B + z')}[V_B - V_{tB}], \quad (24)$$

where V_{tB} is the intercept velocity calculated with use of eq (21) and with use of the density and acoustic impedance of liquid B for ρ and z, respectively.

If the depth of pits produced by collision of the solid target with drops of liquid A is to be the same as that produced by collision of the solid target with drops of liquid B, then, by equating δ_A' and δ_B' given by eqs (23) and (24),

$$V_A = \frac{d_B z_B c_A (z_A + z')}{d_A z_A c_B (z_B + z')} V_B - \frac{d_B z_B c_A (z_A + z')}{d_A z_A c_B (z_B + z')}\left[\frac{19 E'(z_B + z')}{(\rho_B c' z'^3)^{1/2}}\right] + \frac{19 E'(z_A + z')}{(\rho_A c' z'^3)^{1/2}}. \quad (25)$$

All quantities are expressed in cgs units. The dynamic compressive yield strength must be used for E' and the sound speed in infinite medium must be used for c' and in computing z' in making calculations with this equation.

2.8. Applicability of the Damage Equation

It was remarked in section 2.2 that the extent and type of damage produced on solids as a result of collision with liquid drops depends strongly on the characteristic properties of the solid, and that if the damage is to be described by an equation, it will be necessary to develop separate equations for the damage produced on solid materials that have widely different properties. It was pointed out that the simplest case to consider is that of materials such as the soft and medium hard metals that undergo permanent plastic flow without fracture as a result of collision with liquid drops. Equation (22) has been developed to describe the depth of pits that will be produced in materials of this kind as a result of such collisions. It cannot validly be applied beyond the limits of the model on which it was constructed.

Equation (22) is restricted to damage associated with the impact pressure that results when a solid target collides with a liquid drop at high speed. The dimensionless Reynolds number, Weber number, and surface tension quotient, which are associated with the radial flow of the drop, were deleted from eq (7) to produce eq (8), and eq (22) contains only the dimensionless quotients that appear in eq (8). In view of this restriction on eq (22) it can be expected that there will be limits on its application even to the soft and medium hard metals.

In discussing the agreement of the calculated curve with the experimental points for lead target plates it was pointed out that for metals as soft as lead at very high collision velocities the radial flow of a mercury drop drags metal up the walls of the damage pit and piles it up at the mouth of the crater. This mode of forming, or of deepening, a pit was not considered in the development of eq (22), and eq (22) will not adequately describe pits that were produced either wholly or appreciably by this mechanism. It is noteworthy that where this additional pit-forming mechanism does not operate (in the low-velocity range), eq (22) does adequately describe the pits that are formed in lead.

Two other points should be mentioned with regard to the valid use of eq (22) for determining the depth of pits that will be produced in collisions between target plates of the medium hard metals (to which it applies) and liquid drops. One is the mode of mounting the plate of solid material with which the liquid drops collide; the other is the thickness of this plate. The reverse side of the plate must be maintained as a free surface for otherwise the core of solid material through the metal plate under the contact or collision area cannot move freely with respect to the remainder of the plate, which is an essential of the model on which eq (22) is based. The bulge on the reverse side of the 1100-aluminum plate shown in picture 6 of figure 2 appears to indicate that this condition was sufficiently realized in the mounting of the metal plates that were used for the mercury drop experiments.[2] If this condition is not realized, eq (22) cannot be applied to the pit depths that are obtained. The thickness of the plate should not be less than 1.5 to 2.0 times nor greater than 4 to 5 times the diameter of the impinging liquid drops. If the plate is too thin, the model on which eq (22) is based will break down because the plate will bend as a unit under the collision blow. If the plate is too thick, the spreading of the compressional wave on passing through it may cease to be negligible.

Equation (22) was constructed on the assumption of permanent plastic flow of the material of the target plate. The dimensionless quotient e'/E' of eq (7), which represents the resilience of the plate material, has been neglected. Consequently, eq (22) cannot validly be applied to determine the depth of pits that will form in highly resilient materials such as the polymers and rubbers when they collide with liquid drops. In the case of such materials the core of target material depressed as a result of the collision tends to spring back into its original position; the permanent damage mark that remains after the collision is more nearly a circular cut than a pit.

Equation (22) has been constructed using a very simple model. To determine how the Reynolds number and the Weber number should be introduced into eq (22), pit-depth-versus-velocity data should be obtained on a single metal for the condition that

the viscosity and surface tension of the drop liquid are gradually changed (such as by the use of glycerol-water solutions). To determine how the sound speed, c, of the liquid should appear in the expression for the intercept velocity, data should be obtained using the same metals that have been used already and a liquid that has a sound speed different from those of water and mercury, which are nearly the same. Chloroform has a sound speed about 68 percent that of water. The sound speed of water can be increased by adding sodium chloride. The speed of sound in a 20 percent sodium chloride solution is about 13 percent greater than that in fresh water and it is indicated that increase in the salt concentration will further increase the sound speed.

Finally, more pit-depth-versus-velocity data should be obtained for collision of both mercury drops and waterdrops against target metals whose dynamic compressive yield strengths are known. Whiffin [7] has determined the dynamic compressive yield strength of standard silver (7.5% Cu, 92.5% Ag), electrolytic copper, 99.97 percent lead ,and Armco iron (0.016% C, 0.006% Si, 0.017% S, 0.003% P, and 0.030% Mn). In the process of verifying eq (22) it is important to use target materials whose dynamic compressive yield strengths are known, and the same target material should be used throughout where drops of different liquids are used. If eq (22) is fully verified, it can be used to determine the dynamic compressive yield strength of other metals.

3. Collisions Between Metal Plates and Flowing Metal Spheres

Partridge, VanFleet, and Whited [11] fired spheres of zinc, tin, copper, lead, aluminum, and iron against targets of the same material at collision velocities up to 24×10^4 cm/sec (7,900 ft/sec) and maintained conditions such that the spherical pellet lost no mass before striking the target. They found that the penetration varied linearly with velocity for the materials used and the velocity range investigated. They reported that the pellets flowed during the collisions.

In the light of the fact that the pellets flowed during the collisions, it is reasonable to suppose that the pit-depth-versus-velocity equation that was developed for collisions of metal targets with liquid drops, eqs (21) and (22), should apply to this case without modification. When the material of the target is the same as the material of the projectile, eqs (21) and (22) simplify to

$$\delta' = 3.6\, d\, (V - V_i)/c \qquad (26)$$

and

$$V_i = 38\, E'/z \qquad (27)$$

Some of the pit-depth-versus-velocity data [11] are plotted in figures 16, 17, 18, 19, and 20 along with curves calculated by use of eqs (26) and (27). The physical properties of the metals used by Partridge et al. [11] were not determined. The physical constants used for these materials in eqs (26) and (27) are given in table 2.

3.1. Collisions of Iron Spheres Against Iron Targets

It is assumed that soft, relatively pure iron was used in these experiments [11] because the spherical pellets fired were made by placing fragments of the metal in the hemispherical cavities of a case-hardened steel tool and pressing the two sections together. The diameter of the pellets for which the experimental pit-depth-versus-velocity data are given in figure 16 was 0.483 cm. The calculated curve is shown in figure 16 along with the experimental points which are indicated with circles. The observed pit depths for iron spheres colliding with iron targets are in good agreement with the calculated curve up to a collision velocity of 24×10^4 cm/sec (7,900 ft/sec). This velocity is, however, less than half the speed of sound in infinite medium for iron (58.5×10^4 cm/sec).

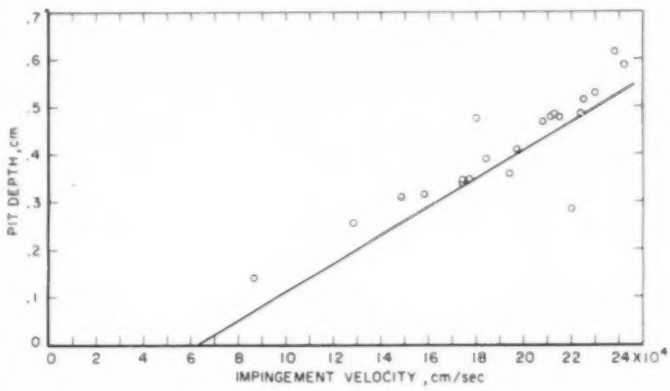

FIGURE 16. *Calculated curve for collisions of 0.483-cm iron spheres against iron targets.*

⊙ observed depth for 0.483-cm sphere.

3.2. Collisions of Aluminum Spheres With Aluminum Targets

Values for physical constants of 1100–0 aluminum were used in eqs (26) and (27). The value of the dynamic compressive yield strength used for E' in eq (27) was computed from a ratio of the dynamic to the static yield strength of 4; this is a rough ratio estimated by Whiffin [10] for an 1100–0 aluminum having an average static yield strength of 2,625 psi.

Very few experimental pit depths were given by Partridge et al. [11] for collisions of 0.483-cm aluminum spheres with aluminum targets. The data available contain quite a bit of scatter. They are plotted in figure 17 along with the curve calculated using eqs (26) and (27). There is reasonably good agreement with the calculated curve. The highest collision velocity for which a pit depth was reported is approximately one-third of the speed of sound in aluminum.

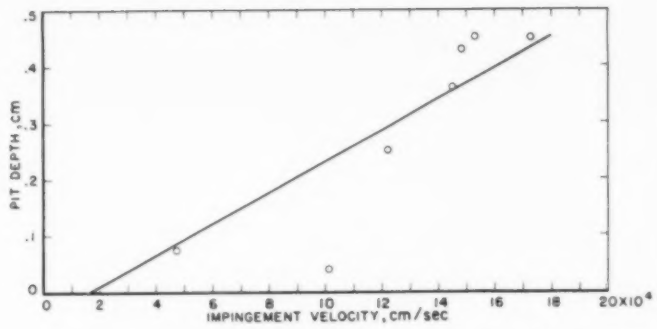

FIGURE 17. *Calculated curve for collisions of 0.483-cm aluminum spheres against aluminum targets.*

⊙ observed depth for 0.483-cm sphere.

3.3. Collisions of Lead Spheres Against Lead Targets

Whiffin [7] determined the dynamic compressive yield strength of lead that was 99.97 per cent pure and this value of the dynamic compressive yield strength was used for E' in eq (27). The sound speed in infinite medium was determined by Tschiegg (table 2) both for chemical lead and for pig lead. The theoretical curve computed using the sound speed for pig lead is shown in figure 18 along with the pit-depth-versus-velocity data obtained by Partridge et al. [15] for 0.483-cm lead spheres impinging against lead targets.

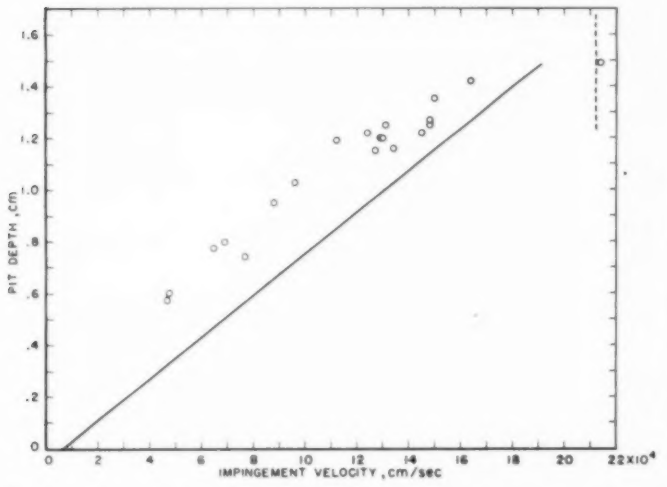

FIGURE 18. *Calculated curve for collisions of 3/16-in. lead spheres against lead targets.*

⊙ observed depth for 3/16-in. sphere.

The experimental pit depths found at the high velocities used are all greater than eq (26) would predict. No data were obtained in the low velocity range where the calculated curve was found to fit the data for collisions of lead target plates with mercury drops. See section 2.6a, where the possibility that two mechanisms contribute to the formation of pits in lead at high collision velocities is discussed.

The speed of sound in infinite medium for pig lead is marked with a vertical dotted line in figure 18. It would appear from the empirical data at the highest velocities used that the experimental pit-depth-versus-velocity curve for lead is flattening at velocities above the speed of sound in lead.

It appears from the data that have been presented in the preceding sections that, at collision velocities for which an originally solid target remains solid during the collision, pit depth is a straight-line function of collision velocity if the rear face of the target plate is a free surface. This appears to be the case regardless of whether the projectile was originally solid and remains solid during the collision (low-speed solid-to-solid collisions), whether the projectile was originally solid but flows during or as a result of the collision (high-speed solid-to-solid collisions), or whether the projectile was originally a liquid drop (liquid-to-solid collisions). At extremely high (meteoric) collision velocities it appears that an originally solid target may be expected to behave like a liquid during the collision because of the enormous impact pressure developed. With regard to collisions of this kind Öpik [13] has stated that the aerodynamic ($1/2\ \rho V^2$) pressure at the penetration of a meteor into rock is more than 1,000 times the plastic limit of steel; he has hypothesized that all solid materials under such pressures must behave like liquids and that the problem of meteor impact is the case of the impact of a liquid drop of one density into a liquid medium of a different density. Under such conditions the penetration or pit depth may become independent of the collision velocity, or may become essentially so, and the pit-depth-versus-velocity curve may approach a horizontal line parallel to the velocity axis. A trend in this direction may be indicated by the flattening of the experimental pit-depth-versus-velocity curve for lead. Whenever this condition is realized, either partially or completely, the pit-depth-versus-velocity equation developed in this paper will no longer be applicable.

3.4. Collision of Copper Spheres Against Copper Targets

The data for impingement of 0.483-cm copper spheres against copper targets [11] are shown in figure 19 along with the theoretical curve calculated by eqs (26) and (27) using physical constants for electrolytic copper (table 2).

The empirical pit-depth-versus-velocity curve for copper appears as though it may be flattening at the highest collision velocities for which data were obtained, as was found in the case of lead. If this is indeed true, it raises the question as to what determines the flattening of the curve. In the case of lead it happened at collision velocities equal to the speed of sound in lead. If it is happening for copper at velocities of 16×10^4 to 18×10^4 cm/sec, it is happening at velocities that are about half the speed of sound in copper. The speed of sound in infinite medium for electrolytic tough pitch copper is 46.91 $\times10^4$ cm/sec. It does not, furthermore, seem to be

related to the melting point of the target material because copper has a high melting point and lead has a very low one. A possible explanation is the relative susceptibility of the target material to flow by translational slip of the target atoms on their lattice planes at high rates of loading. With regard to the use of copper as a liner for shaped charges, Rinehart and Pearson [14] state that copper flows readily at high rates of loading.

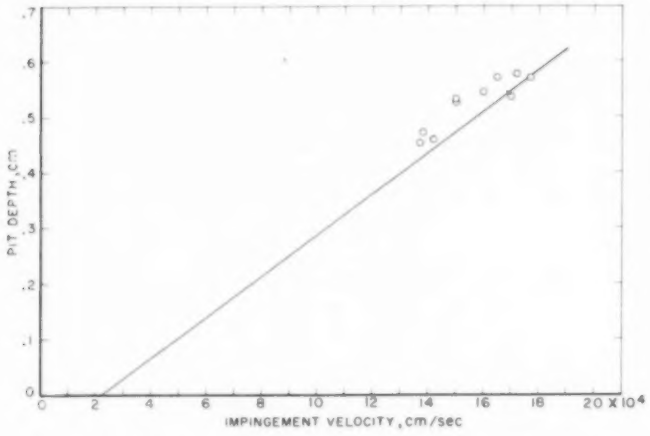

FIGURE 19. *Calculated curve for collisions of 0.483-cm copper spheres against copper targets.*

⊙ observed depth for 0.483-cm sphere.

3.5. Collisions of Zinc Spheres Against Zinc Targets

No value of the dynamic compressive yield strength of zinc was obtainable. One of the possible uses of the pit-depth-versus-velocity equation reported in this paper is the calculation of the dynamic compressive yield strength from pit-depth-versus-velocity data. By trial it was found that to obtain an acceptable value of the intercept velocity for zinc with the pit-depth-versus-velocity data of Partridge et al. [11], the value of the dynamic compressive yield strength for zinc would be 1.546×10^9 d/cm^2. The experimental pit-depth-versus-velocity data for zinc and the line calculated from eqs (26) and (27) using this value of the dynamic compressive yield strength and the physical constants given in table 2 are shown in figure 20. The agreement between the experimental points and the theoretical curve is reasonably good. The two points obtained at the highest velocities used seem to show a flattening of the curve. More experimental data are needed to determine whether this is the case.

WASHINGTON, January 29, 1959.

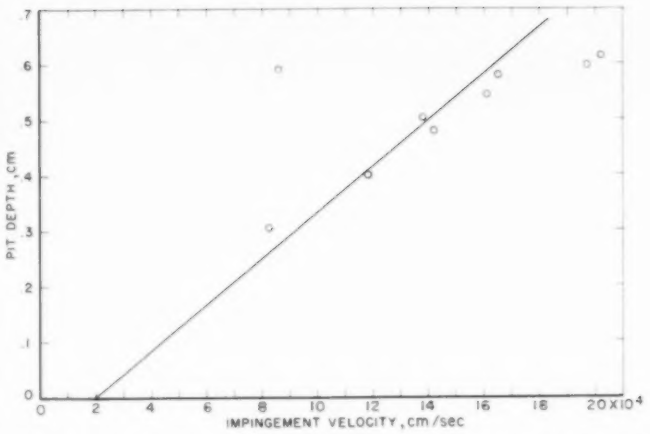

FIGURE 20. *Calculated curve for collisions of 0.483-cm zinc spheres against zinc targets.*

⊙ observed depth for 0.483-cm sphere.

3.6. Collisions of Tin Spheres Against Tin Targets

Partridge et al. [11] also obtained pit-depth-versus-velocity data for collisions of tin spheres against tin targets. The tin appeared to crack and break off rather than to flow plastically around the crater. This interesting fact recalls the similarity in behavior of materials at low temperature and at high rates of loading. At low temperature tin tends to exist in the brittle gray tin form. It is doubtful whether the pit-depth-versus-velocity equation can be validly applied to tin because of the energy that is diverted from pit formation into crack formation (see section 2.8).

4. References

[1] Olive Engel, NBS J. Research **61,** 47 (1958).
[2] Olive Engel, NBS J. Research **54,** 281 (1955).
[3] E. Buckingham, Phys. Rev. **4,** 345 (1914).
[4] E. Buckingham, Phil. Mag. **42,** 696 (1921).
[5] P. W. Bridgman, Dimensional Analysis (Yale University Press, 1931).
[6] Garrett Birkhoff, Hydrodynamics (Princeton University Press, 1950).
[7] A. C. Whiffin, Proc. Roy. Soc. [A] **194,** 300 (1948).
[8] Communicated by letter.
[9] J. M. Krafft and A. M. Sullivan, Trans. Am. Soc. Metals **51,** (1957) (Preprint).
[10] Communicated by letter.
[11] William S. Partridge, Howard B. VanFleet, and Charles R. Whited, J. Appl. Phys. **29,** 1332 (1958).
[12] L. Bergmann, Der Ultraschall, S. Hirzel, Stuttgart (1954).
[13] Ernst Öpik, Researches on the physical theory of meteor phenomena I, Toimetused, Acta et Commentationes (Universitatis Tartuensis XXX [A] **4,** (1936, Tartu, Estonia).
[14] John S. Rinehart and John Pearson, Behavior of metals under impulsive loads, Am. Soc. Metals (1954).
[15] Howard B. VanFleet, Charles R. Whited, and William S. Partridge, High velocity impact craters in lead-tin alloys, Tech. Rpt. No. ONR–13, Dept. of Elec. Eng., University of Utah, Salt Lake City, Utah (Jan. 1958).

Journal of Research of the National Bureau of Standards Vol. 62, No. 6, June 1959 Research Paper 2959

Earth Currents Near a Monopole Antenna With Symmetrical Top Loading

James R. Wait

Expressions for the fields are developed for a vertical ground-based monopole with a cone or disk located at the top of the antenna to simulate umbrella top loading. The current distribution on the structure is assumed. Using spherical-wave functions, the magnetic-field distribution on the ground plane near the base of the antenna is computed and illustrated by graphs. For the case where the antenna is electrically small, the currents flowing on the cone or disk are shown to contribute only slightly to the total field.

1. Introduction

Transmitting antennas at low radiofrequencies usually take the form of a vertical current-carrying wire loaded by extensive overhead wires which sometimes take the shape of an umbrella. At the risk of oversimplification, a model for field calculations might be a vertical monopole with the umbrella being represented by a continuous cone. In other words, any asymmetry about the vertical axis is neglected. It is the purpose of the present note to investigate the expected influence of the umbrella or cone loading on the fields produced by the antenna with an assumed current distribution.

2. List of Principal Symbols

r_1, θ_1, and ϕ_1 = spherical coordinates of a variable point on the conical sheet.
a = distance from the apex to the rim of the cone.
I_0 = current at the base of the vertical member.
$F(z)$ = current distribution along the vertical member.
h = height of the antenna or length of the vertical member.
Π_z^v = z component of the Hertz vector of the currents on the vertical member.
K = the slope of the current distribution on the vertical member (assumed constant).
$f(r_1)$ = the current distribution along a generator of the cone.
A_q = coefficient for the power series expansion of $f(r_1)$.
z' = a variable point on the vertical member (the integration variable).
ρ, ϕ, z = cylindrical coordinates of the observation point P.
H_t^v = tangential magnetic field on the ground plane resulting from the currents on the vertical member.
Π_ρ^c and Π_z^c = the ρ and z components of the Hertz vector of the currents on the cone.
R = distance from the variable point Q on the cone to the observation point P.
r, θ, z = spherical coordinates of the point P.
$P_n^m(\cos\theta)$ = associated Legendre polynomial of argument $\cos\theta$ and orders n and m.
$jn(kr)$ = spherical Bessel function of the first type of argument kr and argument n.
$h_n^{(2)}(kr)$ = spherical Hankel function of the second kind of argument kr and order n.
$T_n(r_1, r) = jn(kr_1)h_n^{(2)}(kr)$.
H_t^d = tangential magnetic field on the ground plane resulting from the currents on the disk or the cone of angle $\theta_1 = 90°$.
$A_n(r_0)$, $B_n(r_0)$, $C_n(r_0)$ = coefficients for the spherical-harmonic expansion of H_t^d.
r_0 and θ_0 = spherical coordinates of a variable point on the ground plane for the origin at O in figure 1, $r_0 = (\rho^2 + h^2)$ and $\theta_0 = \arctan(\rho/h)$.

$j^r = -aH_t^r/I_0$ . . . = earth current (dimensionless) on the ground plane resulting from the currents on the vertical member.

$j^d = -aH_t^d/I_0$ . . . = earth current (dimensionless) on the ground plane resulting from the currents on the disk.

$\bar{r}$, $\bar{\theta}$ = new spherical coordinates for describing the radiation pattern (see fig. 3).

$J_0(S)$, $J_1(S)$, and $J_2(S)$ are cylindrical Bessel functions of the first type of orders 1, 2, and 3 of the argument S.

3. Some Preliminary Considerations

The top-loaded antenna in its idealized form is shown in figure 1. It consists of a vertical current-carrying wire extending from the point O, at $z=0$, along the axis of a cylindrical coordinate system to the ground surface at $z=h$. The point O is also the apex of a cone which is generated by a line of length, a, at an angle θ_1 to the z axis. With respect to a spherical coordinate system with the origin at O, the coordinates of the bottom rim of the cone are (a, θ_1, ϕ) and those of a variable point Q on the cone are (r_1, θ_1, ϕ_1). The upward current on the central wire filament is taken to be $I_0F(z)$ where I_0 is the current at the apex, i.e., $F(0)=1$, and $I_0F(h)$ is the current at the base. The outward current on an element $dr_1d\phi_1$ on the conical surface is then $(I_0/2\pi)d\phi_1 f(r_1)$ where $f(0)=1$ and $f(a)=0$. Because of symmetry the current on the conical sheet has only a component in the direction of increasing r_1.

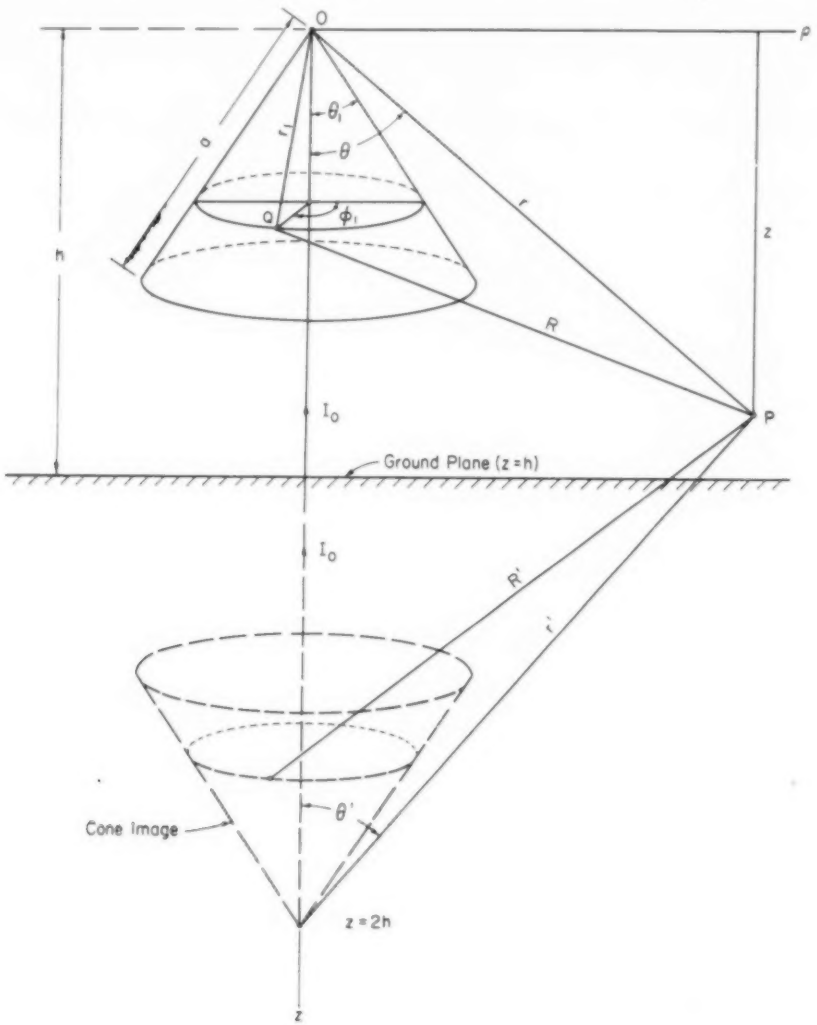

FIGURE 1. *Coordinate system for monopole with cone loading.*

The current distributions, characterized by the functions $F(z)$ and $f(r_1)$, in general, have a very complicated dependence on the antenna dimensions. In the absence of a top loading and where the vertical member can be approximated by a circular cylinder, current distributions can be expressed in terms of an expansion parameter which is proportional to log $(h/2\pi c)$ where c is the radius of the conductor [1].[1] When h is less than one-half wavelength, the distribution is very close to being sinusoidal so long as h is greater than about 100 c. In fact, at very low frequencies where h becomes small compared with the wavelength, the current is then almost a linear function of height. It would not be expected that the cone would modify this conclusion. Therefore

$$F(z) \approx I_0(1-K\ z/h), \tag{1}$$

where K is a constant which depends on the extent of the top loading. For example, in the unloaded case, $K=1$, and in the ideally loaded case, $K=O$, corresponding to a constant current on the vertical member. In most applications where top loading is employed it is known on experimental grounds [3] that $K \approx O$. This is particularly so for high-power installations at low radiofrequencies where the effective dimension of a is comparable to or greater than h, and θ_1 is near 90°.

Information regarding the current distribution function $f(r_1)$ for the conical sheet is apparently not available in the literature. However, if each individual wire making up the cone acts independently, it could be expected that the total current flowing towards the rim of the cone would vary in a linear manner with r, if a is small compared to the wavelength. On the other hand, when the cone degenerates into a disk (i.e., $\theta_1 \approx 90°$) and, if h is somewhat smaller than a, it can be expected the total current flowing towards the rim will vary with the square of r_1. This conclusion is based on the idea that the shunt displacement current density between the circular disk and the ground is a constant if fringing effects at the edges are neglected. A plausible assumed distribution would be

$$f(r_1)=\sum_q \left(\frac{r_1}{a}\right)^q A_q, \tag{2}$$

where the summation could be over $q=0$ and 1 and $A_0=1$, $A_1=-1$ for the linear current approximation; whereas $q=0$ and 2 with $A_0=1$ and $A_2=-1$ for the squared current approximation. It would be possible to employ more elaborate forms of $f(r_1)$ by utilizing more than two values of q. A prime requirement is always

$$\sum_q A_q=0, \tag{3}$$

since $f(a)=0$.

4. Field of the Vertical Member

The Hertz vector $\vec{\Pi}^v$ at the point $P(\rho, 0, z)$ due to the current flowing only on the vertical member is given by $\vec{\Pi}^v=(0, 0, \Pi_z^v)$, where

$$\Pi_z^v=\frac{I_0}{4\pi i\omega\epsilon_0}\left\{\int_0^h \frac{\exp\left[-ik[(z-z')^2+\rho^2]^{1/2}\right]}{[(z-z')^2+\rho^2]^{1/2}}F(z')dz'+\int_0^h \frac{\exp\left[-ik[(2h-z'-z)^2+\rho^2]^{1/2}\right]}{[(2h-z'-z)^2+\rho^2]^{1/2}}F(z')dz'\right\}, \tag{4}$$

when $k=2\pi/\text{wavelength}$ and $\epsilon_0=8.854\times10^{-12}$. The fields are then given by

$$E_\rho^v=\frac{\partial^2\Pi_z^v}{\partial\rho\partial z},\quad E_z^v=\left(k^2+\frac{\partial^2}{\partial z^2}\right)\Pi_z^v,\quad \text{and}\quad H_\phi^v=-i\epsilon_0\omega\frac{\partial\Pi_z}{\partial\rho}. \tag{5}$$

[1] Figures in brackets indicate the literature references at the end of this paper.

The second integral in eq (4) can be identified with the image of the vertical member below the plane $z=h$. It can be verified that $E_\rho^v=0$ at $z=h$, which is the required boundary condition for the ideally conducting ground.

The tangential magnetic field, H_t, on the ground plane is then explicitly given by

$$H_t^v=-\frac{I_0}{2\pi}\frac{\partial}{\partial\rho}\int_0^h \frac{F(z')\exp\{-ik[(z'-h)^2+\rho^2]^{1/2}\}}{[(z'-h)^2+\rho^2]^{1/2}}\,dz'. \tag{6}$$

Considering the important case where $\beta h<<1$ and $F(z')\approx 1$, it follows that

$$H_t^v\approx-\frac{e^{-ik\rho}\rho I_0}{2\pi}\int_0^h\left[\frac{1}{[\rho^2+(z')^2]^{3/2}}+\frac{ik}{\rho^2+(z')^2}\right]dz'$$

$$\approx-\frac{e^{-ik\rho}I_0}{2\pi\rho}\left[\frac{h}{(\rho^2+h^2)^{1/2}}+ik\rho\tan^{-1}\left(\frac{h}{\rho}\right)\right]. \tag{7}$$

This can be expanded in a power series in (h/ρ), so that

$$H_t^v\approx-\frac{e^{-ik\rho}I_0}{2\pi\rho}\left[\left(\frac{h}{\rho}\right)(1+ik\rho)-\left(\frac{h}{\rho}\right)^3\left(\frac{1}{2}+\frac{i}{3}k\rho\right)+\text{ . . . terms containing }\left(\frac{h}{\rho}\right)^5,\ \left(\frac{h}{\rho}\right)^7,\ \text{etc.}\right]. \tag{8}$$

The first term of this expansion corresponds to the field of a hertzian dipole radiator. The additional terms can be regarded corrections to account for the finite value of the antenna height and can be called multipole terms. Sufficiently close to the base, such that $k\rho<<1$, the following expression will suffice

$$H_t^v\approx-\frac{I_0}{2\pi}\frac{h}{\rho(\rho^2+h^2)^{1/2}}, \tag{9}$$

which is a quasi-static approximation. A check on this result is obtained by noting that

$$\lim_{\rho\to 0}H_t^v=-\frac{I_0}{2\pi\rho},$$

which could be predicted from Ampere's law.

5. Field of the Conical Currents

From an argument based on symmetry, it can be seen that the Hertz vector $\vec{\Pi}^c$ at P, due to the currents flowing in the cone, has a vanishing ϕ component. The ρ and z components, however, are, in general, nonvanishing. These can be expressed as an integration over the area of the cone, such that,

$$\Pi_\rho^c=\frac{(I_0/2\pi)\sin\theta_1}{4\pi i\epsilon_0\omega}\int_0^{2\pi}d\phi_1\int_0^a dr_1\cos\phi_1\frac{e^{-ikR}}{R}f(r_1), \tag{10}$$

and

$$\Pi_z^c=\frac{(I_0/2\pi)\cos\theta_1}{4\pi i\epsilon_0\omega}\int_0^{2\pi}d\phi_1\int_0^a dr_1\frac{e^{-ikR}}{R}f(r_1), \tag{11}$$

where $R^2=r^2+r_1^2-2rr_1\cos\Omega$ and $\cos\Omega=\cos\theta\cos\theta_1+\sin\theta\sin\theta_1\cos\phi_1$. Now the factor $1/R$ is a solution of Laplace's equation and can be written in terms of spherical harmonics, as is well known [2],

$$\frac{1}{R}=\sum_{n=0}^{\infty}\sum_{m=0}^{n}\epsilon_m\frac{(n-m)!}{(n+m)!}P_n^m(\cos\theta)\,P_n^m(\cos\theta_1)\cos m\phi_1\begin{cases}r_1^n/r^{n+1};\ r>r_1\\ r^n/r_1^{n+1};\ r_1>r.\end{cases} \tag{12}$$

where $\epsilon_0=1$, $\epsilon_m=2$ if $(m\neq 0)$, and where the P_n^m are associated Legendre polynomials. The factor e^{-ikR}/R, on the other hand, is a solution of the wave equation and an expansion for it in terms of spherical wave functions can be expected. Such an expansion does not seem to be available;

it can be obtained, somewhat heuristically, by noting that it should reduce to eq (12) for kr and kr_1 small, and should give rise to outgoing wave at infinity. Such an expansion is

$$\frac{e^{-ikR}}{R}=-ik\sum_{n=0}^{\infty}\sum_{m=0}^{n}\epsilon_m\frac{(n-m)!}{(n+m)!}(2n+1)P_n^m(\cos\theta)P_n^m(\cos\theta_1)\cos m\phi_1\begin{cases}jn(kr_1)h_n^{(2)}(kr);\ r>r_1\\ jn(kr)h_n^{(2)}(kr_1);\ r_1>r,\end{cases}\tag{13}$$

where $jn(kr_1)$ is a spherical Bessel function and $h_n^{(2)}(kr)$ is a spherical Hankel function of the second kind. These are defined by

$$jn(x)=(-1)^n x^n\left(\frac{d}{x\,dx}\right)^n\left(\frac{\sin x}{x}\right),\tag{14}$$

and

$$h_n^{(2)}(x)=i(-1)^n\left(\frac{d}{x\,dx}\right)^n\left(\frac{e^{-ix}}{x}\right).\tag{15}$$

The integration, with respect to ϕ_1, in eq (10) and (11) requires the evaluation of

$$I_1(r,\theta)=\frac{1}{2\pi}\int_0^{2\pi}\frac{e^{-ikR}}{R}\cos\phi_1 d\phi_1\tag{16}$$

and

$$I_2(r,\theta)=\frac{1}{2\pi}\int_0^{2\pi}\frac{e^{-ikR}}{R}d\phi_1,\tag{17}$$

which can now be rewritten

$$I_1(r,\theta)=-ik\sum_{n=1}^{\infty}\frac{(2n+1)}{n(n+1)}P_n^1(\cos\theta)P_n^1(\cos\theta_1)\begin{cases}T_n(r_1,r);\ r>r_1\\ T_n(r,r_1);\ r_1>r\end{cases}\tag{18}$$

and

$$I_2(r,\theta)=-ik\sum_{n=0}^{\infty}(2n+1)P_n^0(\cos\theta)P_n^0(\cos\theta_1)\begin{cases}T_n(r_1,r);\ r>r_1\\ T_n(r,r_1);\ r_1>r\end{cases}\tag{19}$$

where $T_n(r_1,r)=jn(kr_1)h_n^{(2)}(kr)$.

The circumferential field H_ϕ^c due to the conical currents is given by

$$H_\phi^c=i\epsilon_0\omega\left[\frac{\partial\Pi_p^c}{\partial z}-\frac{\partial\Pi_z^c}{\partial\rho}\right],\tag{20}$$

$$H_\phi^c=i\epsilon_0\omega\left[\frac{\partial\Pi_p^c}{\partial r}\cos\theta-\frac{\partial\Pi_p^c}{r\partial\theta}\sin\theta-\frac{\partial\Pi_z^c}{\partial r}\sin\theta-\frac{\partial\Pi_z^c}{r\partial\theta}\cos\theta\right],\tag{21}$$

where

$$i\epsilon_0\omega\Pi_\rho^c=\frac{I_0\sin\theta_1}{4\pi}\int_0^a f(r_1)I_1(r,\theta)dr_1,\tag{22}$$

and

$$i\epsilon_0\omega\Pi_z^c=\frac{I_0\cos\theta_1}{4\pi}\int_0^a f(r_1)I_2(r,\theta)dr_1.\tag{23}$$

To satisfy the boundary conditions at the ground plane, $z=h$, the fields of the mirror image of the cone must be added to H_ϕ^c. For these fields $I_1(r,\theta)$ must be replaced by $-I_1(r',\theta')$ and $I_2(r,\theta)$ by $+I_2(r',\theta')$ where $\theta'=\mathrm{M}-\theta$, $r'=[(2\mathrm{h}-z)^2+\rho^2]^{\frac{1}{2}}$, and $\cos M=[(r)^2+(r')^2-4h^2]/2rr'$.

The preceding equations, along with eq (7) and (8), constitute the complete formal solution for the fields of a cone-loaded monopole for a specified current distribution on the structure.

6. Disk-Loaded Monopole

When the angle θ_1 approaches 90°, the cone degenerates into a disk. It is this case that will be considered in some detail here. Of particular interest is the behavior of the currents excited on the ground plane in the vicinity of the disk. In fact, for vlf antennas these near-zone currents have, associated with them, considerable ohmic losses due to the imperfect conduc-

tivity of the soil [4]. The surface current density is by definition numerically equal to the tangential magnetic field H_t^d on the ground plane. For the case $kr<<1$, it follows that

$$H_t^d=\frac{I_0}{2\pi}\sum_{n=1}^{\infty}[A_n(r_0)P_{n+1}^1(\cos\theta_0)+B_n(r_0)P_{n-1}^1(\cos\theta_0)]P_n^1(0) \text{ for } r_0<a \tag{24}$$

and

$$H_t^d=\frac{I_0}{2\pi}\sum_{n=1}^{\infty}C_n(r_0)P_{n+1}^1(\cos\theta_0)P_n^1(0) \text{ for } r_0>a, \tag{25}$$

where

$$A_n(r_0)=-\int_0^{r_0}\frac{f(r_1)r_1^n}{(n+1)r_0^{n+2}}dr_1, \tag{26}$$

$$B_n(r_0)=\int_{r_0}^{a}\frac{f(r_1)r_0^{n-1}}{nr_1^{n+1}}dr_1, \tag{27}$$

$$C_n(r_0)=-\int_0^{a}\frac{f(r_1)r_1^n}{(n+1)r_0^{n+2}}dr_1, \tag{28}$$

and $r_0=(\rho^2+h^2)^{1/2}$ and $\theta_0=\arctan(\rho/h)$.

Setting

$$f(r_1)=\sum_q A_q(r_1/a)^q, \tag{29}$$

it is a simple matter to arrive at

$$A_n(r_0)=-\frac{1}{r_0}\sum_q\frac{(r_0/a)^qA_q}{(n+1)(n+q+1)}, \tag{30}$$

$$B_n(r_0)=\sum_q\frac{1}{nr_0(q-n)}\left[\left(\frac{r_0}{a}\right)^n-\left(\frac{r_0}{a}\right)^q\right]A_q, \tag{31}$$

$$C_n(r_0)=-\sum_q\frac{1}{r_0}\frac{(a/r_0)^{n+1}A_q}{(n+q+1)(n+1)}. \tag{32}$$

Setting $A_0=1$, $A_2=-1$ and the other A_q's equal to zero, the squared current distribution, $f(r_1)=1-(r_1^2/a^2)$, is attained. Numerical values of the normalized current, $j^d=-aH_t^d/I_0$ and $j^v=-aH_t^v/I_0$ are shown plotted in figure 2 as a function of ρ/a for the squared current distribution on the disk and a constant current on the vertical member. The values of the ratio h/a are shown on the curves. The resultant current j on the ground plane which is radially directed is given simply by j^d+j^v in the near-zone region where ρ is small compared to the wavelength.

It is of interest to examine the radiation field such that $r>>$wavelength. The spherical Hankel functions can then be well approximated by the first term of their asymptotic expansion. The radiation field H_ϕ^d of the disk by itself is then given by

$$H_\phi^d\approx-\frac{ikI_0e^{-ikr}}{4\pi r}\cos\theta\sum_{n=1}^{\infty}\frac{(2n+1)}{n(n+1)}P_n^1(\cos\theta)P_n^1(0)\int_{r_1=0}^{a}jn(kr_1)f(r_1)dr_1. \tag{33}$$

The radiation of the disk and its image is obtained by adding $H_\phi^{d'}$ to the preceding equation which is of the same form as $-H_\phi^d$ with $\pi-\theta$ replacing θ, and $r-2hk\cos\theta$ replacing r. The summation in the preceding can be converted to a Bessel function by first starting with the addition theorem;

$$\exp(ikr_1\sin\theta\cos\phi)=\sum_{m=0}^{n}\sum_{n=0}^{\infty}\epsilon_m\frac{(n-m)!}{(n+m)!}(2n+1)P_n^m(\cos\theta)P_n^m(0)\cos m\phi\, jn(kr_1), \tag{34}$$

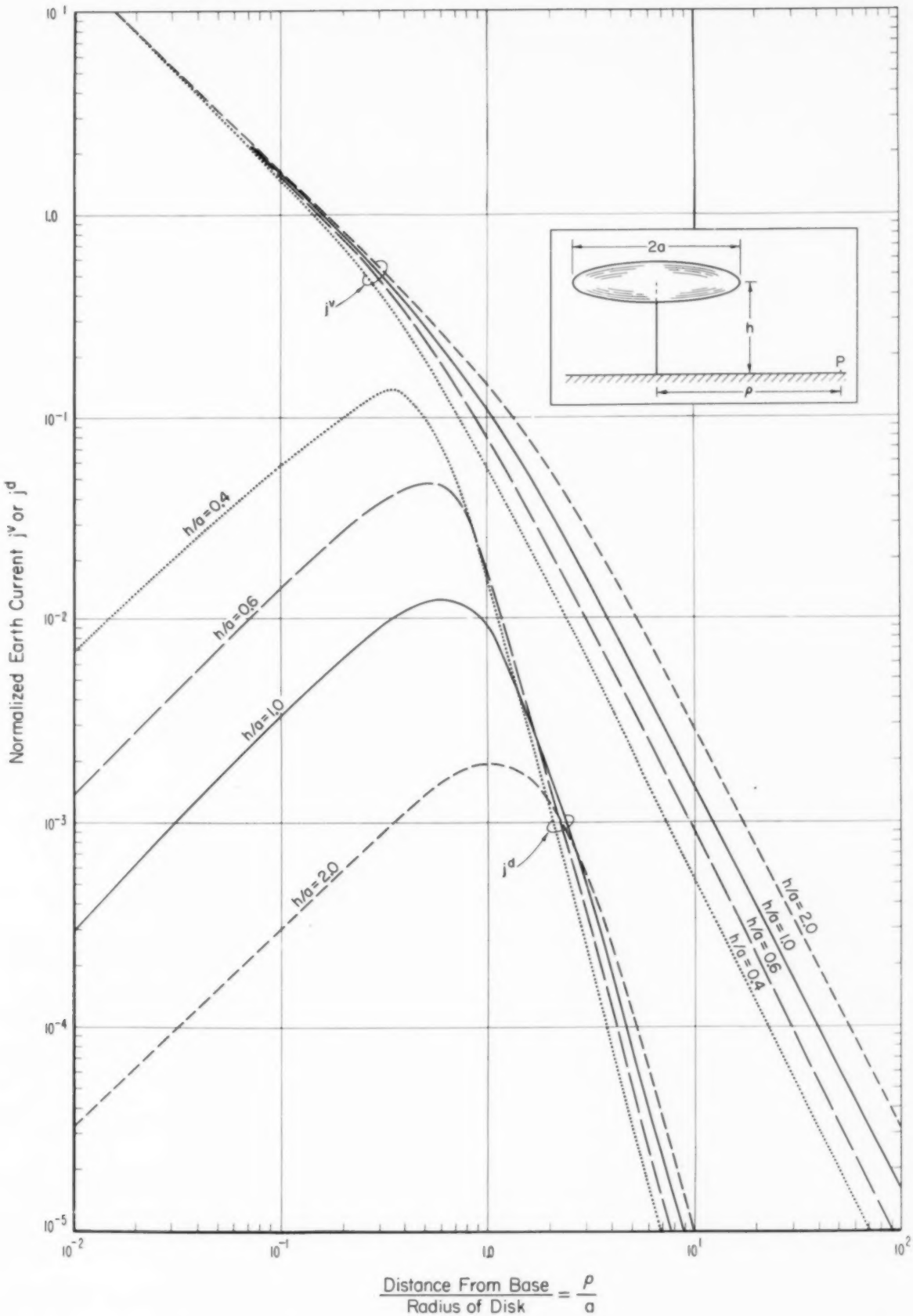

FIGURE 2. *Earth current distribution below a disk-loaded monopole.*

and then multiplying each side by $\cos \phi$ and integrating with respect to ϕ from 0 to 2π. This leads to the interesting relation

$$iJ_1(kr_1 \sin \theta) = \sum_{n=1}^{\infty} \frac{(2n+1)}{n(n+1)} P_n^1(\cos \theta) P_n^1(0) jn(kr_1). \tag{35}$$

Therefore

$$H_\phi^d \approx \frac{kI_0 e^{-ikr}}{4\pi r} \cos \theta \int_{r_1=0}^{a} f(r_1) J_1(kr_1 \sin \theta) dr, \tag{36}$$

subject, of course, to $kr >> 1$. The squared-current assumption, $f(r_1) = 1 - (r_1^2/a^2)$ is now introduced in the above which fortunately enables the integration to be carried out to yield

$$H_\phi^d = \frac{I_0 ka\epsilon^{-ikr}}{4\pi r} \cos \theta \, T(S), \tag{37}$$

where $T(S) = [1 - J_0(S) - J_2(S)]S^{-1}$ with $S = ka \sin \theta$. The field of disk plus its image can then be written

$$H_\phi^d + H_\phi^{d'} \approx \frac{I_0 ka\epsilon^{-ik\bar{r}}}{2\pi \bar{r}} \cos \bar{\theta} \; i \sin (kh \cos \bar{\theta}) T(ka \sin \bar{\theta}), \tag{38}$$

in terms of the spherical coordinates $\bar{r}$, $\bar{\theta}$ with the origin at the base of the vertical member as indicated in figure 3. For the usual case where $ka \sin \theta << 1$, it follows from the power series expansions of the Bessel functions J_0 and J_2, that

$$T(ka \sin \bar{\theta}) \approx \frac{ka \sin \bar{\theta}}{8}, \tag{39}$$

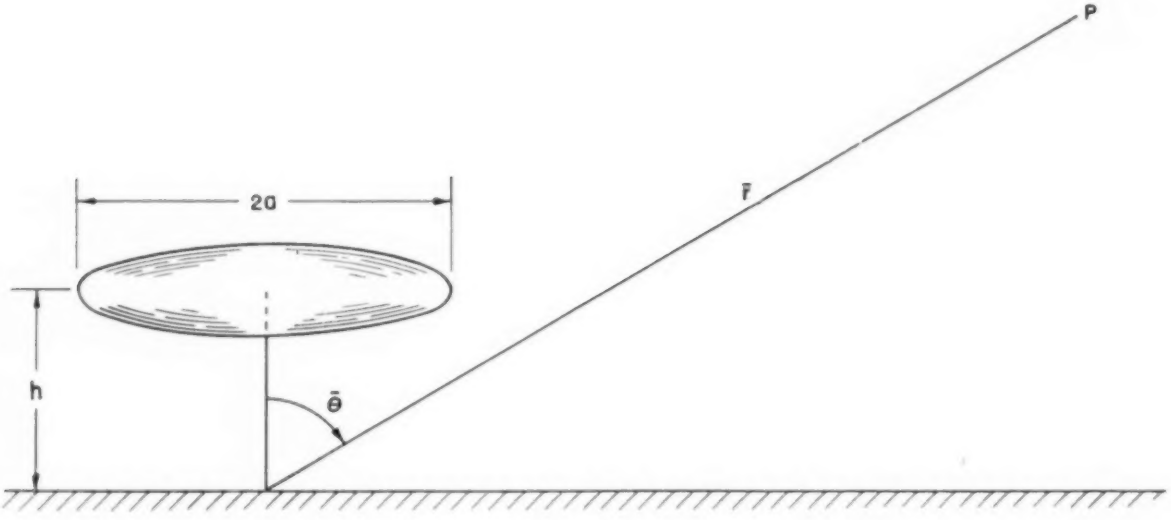

FIGURE 3. *Coordinate system for describing radiation pattern.*

where terms in $(ka \sin \bar{\theta})^3$, etc. have been neglected. Noting that the radiation field for the vertical member in an $\bar{r}$, $\bar{\theta}$ coordinate system can be written

$$H_\phi^v = \frac{ikI_0 he^{-i\beta\bar{r}}}{2\pi\bar{r}} \sin \bar{\theta}, \tag{40}$$

it follows that the resultant radiation field is given simply by

$$H_\phi \approx H_\phi^v \left(1 - \frac{(ka)^2 \cos^2 \bar{\theta}}{8}\right), \tag{41}$$

neglecting terms of order $(ka)^4$.

7. Conclusion

The results indicate that the earth currents near a monopole antenna are not significantly modified by the presence of a symmetrical top loading. Therefore, in any calculation [4] of the energy absorbed in the ground system, it is usually sufficient to consider only the contribution from the currents in the vertical members (downleads). Furthermore, the radiation pattern of a loaded monopole at low radiofrequencies is essentially a dipole pattern being modified to small order by the currents in the top-loading structure. The effect of unsymmetrical top loading is considered in a sequel to this paper [5].

The author thanks Mrs. A. Murphy for carrying out the calculations and W. W. Brown, A. D. Watt, and H. A. Wheeler for informative discussions.

8. References

[1] Ronold W. King, Theory of linear antennas (Harvard Univ. Press, Cambridge, Mass., 1956).
[2] P. M. Morse and H. Feshbach, Methods of theoretical physics, Vol. II, p. 1326 (McGraw-Hill Book Co., New York, N.Y., 1953).
[3] C. E. Smith and E. M. Johnson, Performance of short antennas, Proc. IRE **35,** 1026 (1947).
[4] J. R. Wait and W. A. Pope, Input resistance of l. f. unipole aerials with radial wire earth systems, Wireless Engr. (London) **32,** 131 (1955).
[5] H. L. Knudsen, Earth currents near a top-loaded monopole antenna with special regard to electrically small L- and T-antennas, J. Research NBS **62,** 283 (1959) RP2961.

Boulder, Colo., January 27, 1959.

Journal of Research of the National Bureau of Standards Vol. 62, No. 6, June 1959 Research Paper 2960

Infrared Absorption Spectra of Some Cyclic Acetals of Sugars[1]

R. Stuart Tipson, Horace S. Isbell, and James E. Stewart[2]

The infrared absorption spectra of twenty-eight 1-methoxyethylidene and isopropylidene acetals of sugars have been recorded and analyzed. The formulas of the compounds were grouped according to structure, and the absorption bands for each group were considered in relation to the bands found for the other structurally related compounds. No bands were found for the unequivocal detection of the 1,3-dioxolane ring attached respectively to an aldopentofuranose or a ketopentofuranose, an aldopentopyranose, an aldohexofuranose, an aldohexopyranose or a ketohexopyranose, a uronic acid salt or lactone, a sugar alcohol, or a sugar keto-acid salt. Regardless of the fine structure of the dioxolane compounds, certain strong bands were observed, but the bands are not easily recognized from an inspection of one or two spectra and are not characteristic of these compounds only.

1. Scope and Purpose of the Project

For the purpose of discovering correlations that might be of value in structural analysis, this project was primarily undertaken with the object of providing infrared spectrograms of sugar derivatives containing the 1,3-dioxolane ring (I).

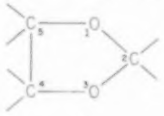

I

It seemed probable that the vibrations of the dioxolane ring of such compounds would be relatively insensitive to changes in the rest of the molecule; and that it should, accordingly, be possible to identify certain bands in their spectra as being characteristic of this ring. Their spectra have, therefore, been recorded; and the bands have been compiled and studied by statistical and comparative methods.

2. Compounds Investigated

In the application of infrared absorption spectra to the determination of structure, it is necessary to have reference spectra for substances of known configuration and conformation. The pyranose ring in simple carbohydrate derivatives is flexible; hence, for some pyranose derivatives, there is much uncertainty concerning the conformation adopted by the ring. In contrast, the conformation of molecules containing fused or bridged rings[3] is more rigid; and consequently, less uncertainty exists as to the relative steric positions of the atoms and groups within their molecules. For this reason, attention has now been directed to the study of a group of cyclic acetals (of cyclic sugars) having bicyclic and tricyclic structures.

Table 1 gives a list of the compounds, their code numbers [1][4,5] and properties, and an index to the spectrograms (the serial number of a compound is the same as the number of its spectrogram). The spectra were measured in the 2- to 15-μ region (5,000 to 667 cm^{-1}; sodium chloride optics) and in the 15- to 40-μ region (667 to 250 cm^{-1}; cesium bromide optics). Inasmuch as a detailed study of all the bands is not possible at present, the spectrograms are given together with a discussion of (a) the structure of the compounds and (b) some of the outstanding features of their spectra.

[1] Presented, in part, before the Division of Carbohydrate Chemistry at the 134th Meeting of the American Chemical Society, at Chicago, Ill., on September 9, 1958. Part of this work was supported by the Chemistry Branch of the Office of Naval Research.

[2] Present address: Beckman Instruments, Inc., Fullerton, Calif.

[3] Fused rings have two adjacent atoms in common, whereas bridged rings have nonadjacent atoms in common.

[4] Figures in brackets indicate the literature references at the end of this paper. The references for table 1 are given at the end of the table.

[5] Code numbers are assigned according to a previously published classification system [1], for use with punched-card techniques.

TABLE 1. *Compounds measured and index to spectrograms*

Code	Compound	Constants reported				Constants found			Spectrogram
		mp, ° C	Specific rotation $[\alpha]_D$	Rotation solvent	Reference	mp, ° C	Specific rotation $[\alpha]_D$	Rotation solvent	
PYRANOSE DERIVATIVES									
A. 1,2-*O*-(1-METHOXYETHYLIDENE) ACETALS									
12.22563(3,4,6)21	D-Mannopyranose 1,2-(methyl orthoacetate) triacetate.[a]	105	−26.6	$CHCl_3$	1	105 to 105.5	−26.8	$CHCl_3$	1
12.22563(3,4)21(6)80	6-Deoxy-L-mannopyranose 1,2-(methyl orthoacetate) diacetate.[a]	83 to 84	+35	$CHCl_3$	2	86 to 86.5	+33.9	$CHCl_3$	2
10.22563(6)80	6-Deoxy-L-mannopyranose 1,2-(methyl orthoacetate).[a]	143 to 144	+16.3	H_2O	3	143 to 144	+16.0	H_2O	3
12.24563(3,4,6)21	D-Talopyranose 1,2-(methyl orthoacetate) triacetate.[a]	91.5 to 92.5	+3.7	$CHCl_3$	4	[b] 77 to 83	(c)		4
22.215(2,3,4,6)21*(1–4).—22263(3,6)21.	β-D-Glucopyranosyl-(1→4)-D-[a] mannopyranose 1,2-(methyl orthoacetate) hexaacetate.	165 to 167	−13.2	$CHCl_3$	5	171 to 172	−13.0	$CHCl_3$	5
22.235(2,3,4,6)21*(1–4).—27263(3,6)21.	β-D-Galactopyranosyl-(1→4)-D-[a] altropyranose 1,2-(methyl orthoacetate) hexaacetate.	121 to 122	+25.3	?	6	121 to 122	+25.0	$CHCl_3$	6
B. ISOPROPYLIDENE ACETALS									
10.235(1,2)61	1,2-*O*-Isopropylidene-D-galactopyranose.[d,a]	157	−10.9	EtOH	7	156 to 157	−11.3	EtOH	7
19.135(1,2:3,4)61	1,2:3,4-Di-*O*-isopropylidene-L-arabinopyranose.[a]	41.5 to 43	+5.4	H_2O	8	42	+5.1	H_2O	8
19.235(1,2:3,4)61(6)21	1,2:3,4-Di-*O*-isopropylidene-D-galactopyranose6-monoacetate.[d]	108	−48.1	$CHCl_3$	9	110 to 112	−49.1	$CHCl_3$	9
19.735(2,3:4,5)61	2,3:4,5-Di-*O*-isopropylidene-D-fructopyranose.[a]	97	−33.7	?	8	97	−33.6	H_2O	10
19.735(1,2:4,5)61	1,2:4,5-Di-*O*-isopropylidene-D-fructopyranose.[f]	118 to 119	−146.6	$CHCl_3$	10	117 to 119	−146.2	$CHCl_3$	11
FURANOSE DERIVATIVES ISOPROPYLIDENE ACETALS									
10.116(1,2)61	1,2-*O*-Isopropylidene-D-xylofuranose.[d]	41 to 43	−17.3	0.2% HCl	11, 12	43 to 45	−17.5	H_2O	12
10.216(1,2)61	1,2-*O*-Isopropylidene-D-glucofuranose.[d]	161 to 162.5	−11.8	H_2O	13	159 to 161	−11.8	H_2O	13
10.256(1,2)61	1,2-*O*-Isopropylidene-L-idofuranose.[a]	113 to 114	−28.7	H_2O	14, 15	113 to 115	−29.0	H_2O	14
10.216(1,2)6175	Lithium 1,2-*O*-isopropylidene-D-glucofuranuronate.[d]	dec.	−3.8	H_2O	16	dec.	−3.8	H_2O	15
10.216(1,2)617599	Barium 1,2-*O*-isopropylidene-D-glucofuranuronate[d] monohydrate.				17	dec.	−2.9	H_2O	16
10.256(1,2)617599	Calcium 1,2-*O*-isopropylidene-L-idofuranuronate[a] dihydrate.		−11.8	H_2O	18	dec.	−11.8	H_2O	17
19.116(1,2:3,5)61	1,2:3,5-Di-*O*-isopropylidene-D-xylofuranose.[d,g]	44 to 45	+19.5	Me_2CO	19, 20	44 to 45	+19.8	Me_2CO	18
19.216(1,2:5,6)61	1,2:5,6-Di-*O*-isopropylidene-D-glucofuranose.[d]	110 to 111	−18.5	H_2O	8, 13	111 to 113	−19.7	H_2O	19
10.216(1,2)61(6,3)72	1,2-*O*-Isopropylidene-D-[d] glucofuranurono-6,3-lactone.	119 to 120	+70.	H_2O	21	118 to 119	+68.7	H_2O	20
10.256(1,2)61(6,3)72	1,2-*O*-Isopropylidene-L-[a] idofuranurono-6,3-lactone.	137 to 138	+91.	Me_2CO	14	[b] 134 to 136	(c)		21
10.126(2,3)761	2,3(or3,5)-*O*-Isopropylidene-D-lyxo(furano?)se.[f,h]	79 to 80	+26.0	Me_2CO	20	79 to 80	+26.1	Me_2CO	22
19.2260(2,3:5,6)61	2,3:5,6-Di-*O*-isopropylidene-D-mannofuranose.[f]	122	+26.8	Me_2CO	22	125 to 126.5	+25.0	Me_2CO	23
19.229(2,3:5,6)61(1,4)72	2,3:5,6-Di-*O*-isopropylidene-D-mannono-1,4-lactone.	126	+51.	$CHCl_3$	23	124	+50.2	$CHCl_3$	24
10.626(2,3)61	2,3-*O*-Isopropylidene-D-*threo*-pentulofuranose.[a]	70 to 71	+1.7	Me_2CO	20	69 to 70	(c)		25
19.716(2,3:4,6)61	2,3:4,6-Di-*O*-isopropylidene-L-*xylo*-hexulofuranose.[d,i]	77 to 78	−18.1	Me_2CO	24	78.5 to 80	−17.0	Me_2CO	26
19.71675(2,3:4,6)61	Potassium 2,3:4,6-di-*O*-isopropylidene-L-*xylo*-hexulofuranonate.[d,j]	>260	−13.8	H_2O	24	>300, dec.	−14.0	H_2O	27
ACYCLIC DERIVATIVE ISOPROPYLIDENE ACETAL									
19.227(1,2:5,6)61	1,2:5,6-Di-*O*-isopropylidene-D-mannitol.	122	+1.2	H_2O	25	115 to 117	+1.0	H_2O	28

[a] Commonly designated as β, although no α anomer is possible. [b] Insufficient material available for recrystallization. [c] Insufficient material available for this determination. [d] Commonly designated as α, although no β anomer is possible. [e] Sample from the P. A. Levene Memorial Collection at the Rockefeller Institute for Medical Research, through the courtesy of Dr. Lyman C. Craig. [f] This compound should be capable of existence in anomeric forms. [g] Nucleating crystals used were from a sample (see footnote e) prepared by one of us (R.S.T.) in 1935. [h] Structure uncertain. [i] Trivial name: 2,3:4,6-di-*O*-isopropylidene-α-L-sorbofuranose. [j] Trivial name: potassium 2,3:4,6-di-*O*-isopropylidene-2-keto-α-L-gulonate.

References for table 1

1. J. K. Dale, J. Am. Chem. Soc. **46,** 1046 (1924).
2. W. N. Haworth, E. L. Hirst, and H. Samuels, J. Chem. Soc. **1931,** 2861.
3. E. Fischer, M. Bergmann, and A. Rabe, Ber. deut. chem. Ges. **53,** 2362 (1920).
4. W. W. Pigman and H. S. Isbell, J. Research NBS **19,** 189 (1937) RP1021.
5. H. S. Isbell, BS J. Research **7,** 1115 (1931) RP392.
6. H. L. Frush and H. S. Isbell, J. Research NBS **27,** 413 (1941) RP1429.
7. P. A. Levene and G. M. Meyer, J. Biol. Chem. **64,** 473 (1925).
8. E. Fischer, Ber. deut. chem. Ges. **28,** 1145 (1895).
9. H Ohle and G. Berend, Ber. deut. chem. Ges. **58,** 2585 (1925).
10. D. H. Brauns and H. L. Frush, BS J. Research **6,** 449 (1931) RP287.
11. O. Svanberg and K. Sjöberg, Ber. deut. chem. Ges. **56,** 863 (1923).
12. W. N. Haworth and C. R. Porter, J. Chem. Soc. **1928,** 611.
13. E. Fischer and C. Rund, Ber. deut. chem. Ges. **49,** 88 (1916).
14. F. Shafizadeh and M. L. Wolfrom, J. Am. Chem. Soc. **77,** 2568 (1955).
15. A. S. Meyer and T. Reichstein, Helv. Chim. Acta **29,** 152 (1946).
16. R. Schaffer and H. S. Isbell, J. Research NBS **56,** 191 (1956) RP2667.
17. C. L. Mehltretter, B. H. Alexander, R. L. Mellies, and C. E. Rist, J. Am. Chem. Soc. **73,** 2424 (1951).
18. R. Schaffer and H. S. Isbell, J. Am. Chem. Soc. **79,** 3867 (1957).
19. P. A. Levene and A. L. Raymond, J. Biol. Chem. **102,** 317 (1933).
20. P. A. Levene and R. S. Tipson, J. Biol. Chem. **115,** 731 (1936).
21. L. N. Owen, S. Peat, and W. J. G. Jones, J. Chem. Soc. **1941,** 339.
22. J. C. Irvine and A. F. Skinner, J. Chem. Soc. **1926,** 1089.
23. H. Ohle and G. Berend, Ber. deut. chem. Ges. **58,** 2590 (1925).
24. T. Reichstein and A. Grüssner, Helv. Chim. Acta **17,** 311 (1934).
25. L. von Vargha ,Ber. deut. chem. Ges. **66,** 1394 (1933).

As a common structural feature, these compounds have the substituted 1,3-dioxolane ring:

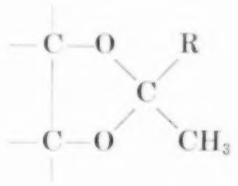

where R=OCH_3 in the 1-methoxyethylidene acetals (methyl orthoacetates), and R=CH_3 in the isopropylidene acetals. All of the compounds have at least one dioxolane ring; and, except for 1,2:5,6-di-*O*-isopropylidene-D-mannitol (compound 28), this ring is fused to either a five- or a six-membered ring.

The precise shape of the dioxolane ring is not known. The bond lengths and bond angles of the atoms comprising the ring are, however, compatible with a planar conformation. The abundance of compounds of this kind having structures explicable by a planar or nearly planar dioxolane ring would tend to support the hypothesis that the ring ordinarily has a planar conformation.

3. Structures of the Compounds

3.1. Methyl Orthoacetates

The 1-methoxyethylidene acetals or 1,2-(methyl orthoacetate(s)), compounds 1 to 6, were prepared in the course of investigations on the mechanisms of replacement reactions conducted over the course of many years [2, 3, 4]. They are acetals containing the

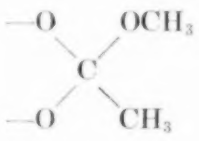

group fused to C1 and C2 of a pyranose ring. In both chair conformations,[6] the *cis* pair of hydroxyl groups at C1 and C2 of the parent sugars is equatorial–axial. Spanning them with a planar dioxolane ring would introduce strain. Hence the pyranose ring or the dioxolane ring, or both, would be somewhat distorted. The following depicts the skeletal structure of a possible sofa conformation:

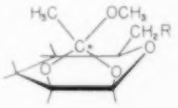

For compounds 1, 4, 5, and 6, R=OAc; for compounds 2 and 3, R=H, and the structure is the mirror image of that depicted.

Although the pyranose ring normally assumes a chair conformation, spanning of C1 and C2 of a boat form of the pyranose ring with a planar dioxolane ring tends to place C1, C2, C3, and the oxygen atom (of the pyranose ring) in a plane at an angle of 120° to the dioxolane ring. Two conformations of this type seem possible, depending on the positions of C4 and C5 of the boat. In one conformation, hereafter designated *endo*, they are directed toward the dioxolane ring, with C6 in an axial position; in the other conformation, designated *exo*, these carbon atoms (C4 and C5) are directed outward from the dioxolane ring, with C6 in an equatorial position.[7] The two skeletal structures are depicted in the following formulas:

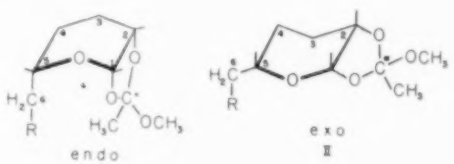

endo

exo

II

In forming the 1,2-(methyl orthoacetate) from the poly-*O*-acetylglycosyl halide by the opposite-face mechanism [6], the *endo* structure would arise by turning the nascent dioxolane ring (in the transition

[6] A discussion of the chair conformations of pyranoid rings is given in a previous article [1].

[7] An *endo* substituent lies in the V of a bicyclic structure, whereas an *exo* substituent lies outside it [5].

state) inward toward C6; and the *exo* structure (II) would arise by turning it outward. The *exo* form would seem to be the more probable for the methyl orthoacetates, because the overall structure is more nearly planar and there is less crowding of the atoms.

All of the orthoacetates studied have essentially the same ring structures. A summary of the positions of the reference groups in the *exo*-boat form (II) of each of these methyl orthoacetates is given in table 2. The ester carbon atom (marked with an asterisk) of the orthoacetates is asymmetric; there is no experimental basis for assigning configuration to it, but since the methoxyl group is larger than the methyl group, it would tend to be directed away from the V of the bicyclic structure.

Decision between the possible conformations indicated must await the outcome of further experimental work.

Isopropylidene derivatives analogous to compounds 1 to 6 (having a methyl group in place of the methoxyl group) seem feasible, but are not known at present. The 1,2-*O*-isopropylidene-D-galactopyranose considered in the next section is closely related; however, it differs in having the opposite configuration at C1 and C2. The 1,2:3,4-di-*O*-isopropylidene derivatives discussed in the next section are also related to the orthoacetates studied, but they may have a more rigid structure because of the stabilizing effect of the second dioxolane ring.

3.2. *O*-Isopropylidene—Pyranose Acetals

Compound 7 of table 1 has one dioxolane ring fused to a pyranose ring. The latter could have a boat (probably *exo*) conformation; however, it might have a distorted sofa conformation in which, at C2, C3, and C4, both *exo*cyclic bonds are approximately quasi instead of being axial—equatorial. The sofa conformation (III) that is equatorially 5-substituted is depicted.

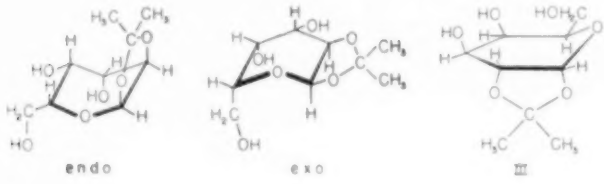

7. 1,2-*O*-Isopropylidene-D-galactopyranose

Compounds 8 to 10 are isopropylidene acetals which, unlike the orthoacetates, have two dioxolane rings fused, on opposite sides, to a pyranose ring. The presence of two nearly planar dioxolane rings in this position is not compatible with the *exo*-boat conformation of the pyranose ring most probably present in the orthoacetates (compounds 1 to 6). The two pairs of *cis* hydroxyl groups (at C1 and C2, and at C3 and C4, for compounds 8 and 9) of the parent sugars are each axial—equatorial in both chair-conformations;[6] and spanning them with a planar dioxolane ring would introduce strains (see IVa). A sofa conformation, in which the pyranose ring or the dioxolane rings (or both) may be somewhat distorted, seems possible. One structure with very little strain is shown in formula IVb.

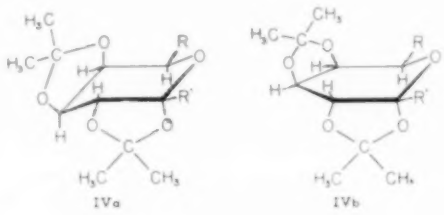

Compounds 8, 9, and 10 presumably have one or the other of the above general structures, with the following substituents.

8. 1,2:3,4-Di-*O*-isopropylidene-L-arabinopyranose, R = H; R′ = H.

9. 1,2:3,4-Di-*O*-isopropylidene-D-galactopyranose monoacetate, R = CH_2OAc; R′ = H.

10. 2,3:4,5-Di-*O*-isopropylidene-D-fructopyranose [1-*C*-(hydroxymethyl)-1,2:3,4-di-*O*-isopropylidene-D-arabinopyranose], R = H; R′ = CH_2OH; and the molecule is the mirror image of that depicted.

1,2:4,5-Di-*O*-isopropylidene-D-fructopyranose (compound 11) differs from the four other derivatives in this group in having a spirane structure at C2, instead of a fused-ring structure. The boat conformation

TABLE 2. *Reference groups* [a] *on the carbon atoms of the pyranoid ring of the* exo*-boat conformation* (II) *of some 1,2-(methyl orthoacetates)*

Compound	C1		C2		C3		C4		C5	
	Group	Position [b]	Group	Position	Group	Position [b]	Group	Position [b]	Group	Position
1	(c)	e	(c)	e	OAc	a	OAc	a	CH_2OAc	e
2	(c)	e	(c)	e	OAc	a	OAc	a	CH_3	e
3	(c)	e	(c)	e	OH	a	OH	a	CH_3	e
4	(c)	e	(c)	e	OAc	a	OAc	e	CH_2OAc	e
5	(c)	e	(c)	e	OAc	a	O(AcG)[d]	a	CH_2OAc	e
6	(c)	e	(c)	e	OAc	e	O(AcGal)[e]	a	CH_2OAc	e

[a] A reference group is any group, other than hydrogen, attached to a carbon atom of the skeletal structure.
[b] The symbols a and e are used to designate axial and equatorial positions, respectively, of the reference groups.
[c] The oxygen atoms of C1 and C2 share a 1-methoxyethylidene grouping.
[d] (AcG) represents a tetra-*O*-acetyl-β-D-glucopyranosyl group.
[e] (AcGal) represents a tetra-*O*-acetyl-β-D-galactopyranosyl group.

shown seems plausible; it somewhat resembles the *exo* form of the methyl orthoacetates (compounds 1 to 6), but differs in the position of the fused ring

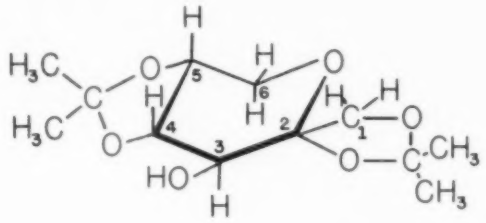

11. 1,2:4,5-Di-*O*-isopropylidene-D-fructopyranose

and in having the spirane structure. It may be noted that, whereas the pyranose compounds 1 to 10 cannot exist in anomeric forms, α and β anomers of compound 11 should be capable of existence.

3.3. *O*-Isopropylidene-Furanose and *O*-Isopropylidene-γ-lactone Derivatives

Compounds 12 to 27 have either one or two dioxolane rings fused onto a furanose or a γ-lactone structure, or both. Because these compounds have 5-membered rings only, the molecules are more rigid than those having fused dioxolane-pyranose structures. Each ring is substantially planar, and hence only one conformation seems probable. In compounds 12 through 21, carbon atoms 1 and 2 are shared by the rings, and in 22,[8] 23, and 24, carbon atoms 2 and 3 are shared. In each case, the fused rings are inclined at an angle of 120° to each other.

Compounds 12 to 19 have the following general structure:

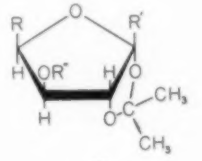

V

12. 1,2-*O*-Isopropylidene-D-xylofuranose, $R=HOCH_2-$; R' and $R''=H$.

13. 1,2-*O*-Isopropylidene-D-glucofuranose, $R=HOCH_2-\underset{OH}{\overset{H}{C}}-$; R' and $R''=H$.

14. 1,2-*O*-Isopropylidene-L-idofuranose, $R=HOCH_2-\underset{H}{\overset{OH}{C}}-$; R' and $R''=H$.

15. Lithium 1,2-*O*-isopropylidene-D-glucuronate, $R=LiO_2C-\underset{OH}{\overset{H}{C}}-$; R' and $R''=H$.

16. Barium 1,2-*O*-isopropylidene-D-glucuronate, $R=Ba_{1/2}O_2C-\underset{OH}{\overset{H}{C}}-$; R' and $R''=H$.

17. Calcium 1,2-*O*-isopropylidene-L-iduronate, $R=Ca_{1/2}O_2C-\underset{H}{\overset{OH}{C}}-$; R' and $R''=H$.

18. 1,2:3,5-Di-*O*-isopropylidene-D-xylofuranose, $RR''=H_2CO-C(CH_3)_2$; $R'=H$.

19. 1,2:5,6-Di-*O*-isopropylidene-D-glucofuranose, $R=H_2C-\underset{\displaystyle H_3C \quad CH_3}{\overset{\displaystyle O \quad O}{C}}-$; R' and $R''=H$.

The isopropylidene derivatives of D-glucuronolactone and L-iduronolactone (compounds 20 and 21) have three fused, 5-membered rings; the furanose ring occupies a middle position, sharing C1 and C2 with the dioxolane ring and C3 and C4 with the lactone ring. The dioxolane ring lies on one side of the plane of the middle ring at an angle of 120°; the lactone ring lies on the other side at an angle of 120°, but is not parallel to the dioxolane ring. Compounds 20 and 21 have the following general structure.

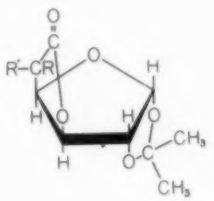

20. 1,2-*O*-Isopropylidene-D-glucofuranurono-6,3-lactone, $R=H$; $R'=OH$.

21. 1,2-*O*-Isopropylidene-L-idofuranurono-6,3-lactone, $R=OH$; $R'=H$.

Compounds 22,[8] 23, and 24 have a dioxolane ring fused at C2 and C3 of the furanose ring and of the γ-lactone ring, respectively. It may be noted that, for compounds 22 [8] and 23, α and β anomers should be capable of existence. Compounds 22,[8] 23, and 24 have the following general structure.

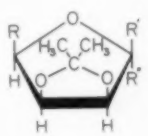

22. 2,3-*O*-Isopropylidene-D-lyxofuranose,[8] $R=HOCH_2-$; $R'=H$ and $R''=OH$ (or vice versa).

[8] Proof of the structure of this compound will be given in a forthcoming publication.

23. 2, 3:5, 6-Di-*O*-isopropylidene-D-mannofuranose,

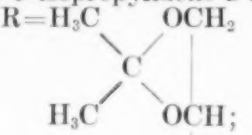

R′=H and R″=OH (or vice versa).

24. 2,3:5,6-Di-*O*-isopropylidene-D-mannono-1,4-lactone,

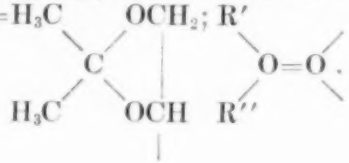

The ketose derivatives 25, 26, and 27 have a dioxolane ring fused at C2 and C3; but if the compounds are regarded as substituted aldoses, these carbon atoms may be classified as C1 and C2 of the furanose ring. Referring back to the skeletal structure V, these compounds have that structure; but, in each case, the molecule is the mirror image of that depicted. The following are the respective substituents:

25. 2,3-*O*-Isopropylidene-D-*threo*-pentulofuranose [1-*C*-(hydroxymethyl)-1,2-*O*-isopropylidene-D-*threo*-tetrofuranose],

R and R″=H; R′=CH_2OH.

26. 2,3:4,6-Di-*O*-isopropylidene-L-sorbofuranose [1-*C*-(hydroxymethyl)-1,2:3,5-di-*O*-isopropylidene-L-xylofuranose],

RR″=H_2COCMe_2; R′=CH_2OH.

27. Potassium 2,3:4,6-di-*O*-isopropylidene-L-*xylo*-hexulofuranonate,

RR″=H_2COCMe_2; R′=COOK.

3.4. Substances with a Fused Dioxolane Ring and a Fused *m*-Dioxane Ring

Compounds 18, 26, and 27 have the following general structure.

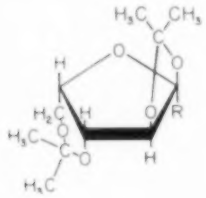

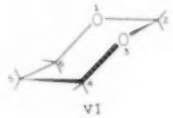

VI

In **26**, R=CH_2OH; in **27**, R=COOK; and in **18**, R=H, and the molecule is the mirror image of that depicted. A *m*-dioxane ring (VI) is present in many sugar acetals; hence, determination of absorption which is characteristic of the structure is highly desirable.

3.5. Substances with "Dangling" Dioxolane Rings

The isopropylidene group attached to the oxygen atoms at C5 and C6 of compounds 19, 23, and 24 forms a dioxolane ring that is free to swing about C4. Presumably, the position assumed by the group depends on the rest of the molecule, and the infrared spectra might be expected to provide information on this subject. Rings of this character, hereafter called "dangling," should have properties quite different from those of the fused rings which are more rigid.

1,2:5,6-Di-*O*-isopropylidene-D-mannitol, compound 28, has a dangling dioxolane ring attached by a carbon–carbon bond to each of the carbon atoms of

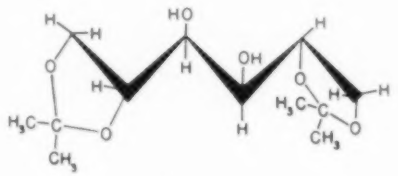

28. 1,2:5,6-Di-*O*-isopropylidene-D-mannitol

ethylene glycol. Presumably, the spectrum of this substance is typical of spectra of compounds having dangling dioxolane rings, and it should be useful for assisting in the interpretation of the spectra of other compounds containing dangling dioxolane rings. Although, for convenience, the ring can be considered as capable of rotation (dangling), hydrogen bonding and steric factors may restrict the structure to a form in which each dioxolane ring lies in a definite steric position.

4. Discussion of the Spectra

Comparison of the spectra of the compounds listed in table 1, on the basis of the structural features outlined in the preceding section, reveals that the absorption bands are not highly characteristic of the type of ring present, and that there are no readily distinguishable bands suitable for the assignment of ring structure or for the study of ring conformation of these compounds. On making a qualitative comparison of any one spectrum with another, it is seen, for example, that in a general way, the spectra of the mono-isopropylidene acetals resemble one another more closely than they do those of the di-isopropylidene acetals, and vice versa, regardless of the particular sugar component or the size (or shape) of the sugar ring.

Although distinctive absorption bands are not apparent for pyranose or furanose, γ-lactone, 1,3-dioxolane, and *m*-dioxane rings, surprisingly large differences are found in the spectra of substances that differ in what might seem to be minor details. These differences can be studied by direct comparison of the spectra for the closely related substances.

On account of the multiplicity of bands and the lack of highly distinctive ones, detection of absorption characteristic for common structural features requires a statistical examination of the data. For this treatment, the compounds were classified according to their structural features, and the locations of the absorption bands were compiled.

The method used for making comparisons is not conventional, but it seems suitable for the study of groups of related compounds. The distribution of the absorption bands for each group of related compounds was determined for the 2- to 15 μ- (5,000 to 667 cm^{-1}) range. First, the number of compounds showing one or more bands (or shoulders) in each wavelength increment of 0.1 μ was counted, and the percentage of such compounds was calculated. This percentage was then plotted against the wavelength, to give the black regions of the plots in figure 1. Only one region (3.3 to 3.4 μ) immediately revealed absorption by all of the compounds. Next, those groups of adjacent regions which seemed likely to encompass 100 percent of the compounds were noted and further examined; the results are given in the crosshatched regions of the plots in figure 1.

Because frequency is directly proportional to energy, use of wavenumbers in correlations of the kind sought is preferable to use of wavelength. On the other hand, the recordings (of infrared spectra) produced by the instruments we used are linear in wavelength, and readings from these charts must initially be made in terms of wavelength. Plots of the kind shown in figure 1 (which use 0.1-μ increments in wavelength) are compact, convenient, and reasonably satisfactory for use in analyzing a limited range.

However, for such plots (linear in wavelength), the bands appear crowded at low wavelengths (high frequencies) and become progressively less crowded as the wavelength increases (that is, as the frequency decreases). The 0.1-μ increments from 2.40 to 2.50 μ, 9.90 to 10.00 μ, and 39.90 to 40.00 μ correspond to decrements of 167, 10, and 0.6 cm^{-1}, respectively.

From the practical standpoint, in making intercomparisons, too much spreading out of bands is just as inconvenient as too much crowding of bands in such plots. Consequently, for the 10- to 40-μ range, all wavelengths were converted to wavenumbers; and, in the analysis, decrements of 10 cm^{-1} in wavenumber were employed. The resulting plots are not reproduced here.

Ultimately, comparisons will be made by use of the classification system described previously [1] using this statistical treatment. The present comparisons are, however, based largely on the structural features characteristic of this relatively limited group of compounds. The compounds were studied in the groups outlined in table 3. By making comparisons for groups of related compounds that differed in various ways, the manner in which the absorption of the various compounds differed on the average was ascertained. Utilization of averages (instead of the individual absorptions) overcomes, at least in part, the "irregularities" found when the spectra of individual compounds are compared. A few comparisons are given here; others will be deferred for inclusion in a study of a wide variety of carbohydrate derivatives.

TABLE 3. *Structural groups studied* [a]

Group	Structural feature	Compounds (numbers) in group
1	*O*-Acetyl (C=O)	1, 2, 4 to 6, 9
2	Carboxyl, ionized (COO^-)	15 to 17, 27
3	1,3-Dioxolane ring	1 to 28
4	Hydrate	16, 17
5	Hydroxyl group	3, 7, 10 to 17, 19 to 23, 25, 26, 28
6	Lactone (C=O)	20, 21, 24
7	*altro* configuration	6
8	*arabino* configuration (ketopyranose).	10, 11
9	*arabino; galacto* configuration (aldopyranose).	8; 6, 7, 9
10	Barium salt	16
11	Calcium salt	17
12	*m*-Dioxane ring	18, 26, 27
13	Furanose ring	12 to 23, 25 to 27
14	*threo; xylo; gluco* configuration	25; 12, 18, 26, 27; 5, 13, 15, 16, 19, 20
15	Glycoside (β-pyranoside)	5, 6
16	Hydroxyl group (glycosidic)	22(?), 23
17	Hydroxyl group (primary)	7, 10, 12 to 14, 22(?), 25, 26
18	Hydroxyl group (secondary)	3, 7, 11 to 17, 19 to 21, 22(?), 25, 28
19	*ido* configuration	14, 17, 21
20	1,2-*O*-Isopropylidene acetal	7 to 21, 25 to 28
21	2,3-*O*-Isopropylidene acetal	22(?), 23, 24
22	5,6-*O*-Isopropylidene acetal ("dangle")	19, 23, 24, 28
23	Lithium salt	15
24	*lyxo; manno* configuration	22; 1 to 3, 5, 23, 24, 28
25	Methoxyl group or methyl orthoacetate	1 to 6
26	5-*C*-Methyl (6-Deoxy) group	2, 3
27	Potassium salt	27
28	Pyranose ring	1 to 11
29	True α-pyranose or β-pyranose	5, 6, 11
30	Pyranose (boat conformation?)	1 to 6, 11
31	Pyranose (chair conformation?)	7 to 10
32	Sugar ring	1 to 23, 25 to 27
33	*talo* configuration	4
34	Three fused rings	8 to 10, 18, 20, 21, 26, 27

[a] The bands found for the various compounds will be considered further in publications dealing with specific structural features.

4.1. Absorption Bands Possibly Attributable to the Dioxolane Ring

In 1949, Boekelheide and co-workers [7] reported infrared spectra for the 2-amyl-2-methyl and 2-hexyl derivatives of 1,3-dioxolane-4-methanol. In 1950, Kuhn [8] recorded the spectra (in the range 8 to 15 μ) of 1,2-*O*-isopropylidene-D-glucofuranose and its 5,6-*O*-isopropylidene acetal (along with those of 77 other carbohydrate derivatives), but made no attempt to analyze these particular spectra. In the following year, Smith and Anderson [9] made a study of the infrared spectra of several 1,3-dioxolane derivatives [10], and decided that it is "likely that the presence of a peak at 9.6 μ indicates the presence of a dioxolane ring." However, it remained for Bergmann and Pinchas [11] to conduct a detailed study of the infrared spectra of 18 compounds having the 1,3-dioxolane ring, and to make definite correlations; their data have also been interpreted by Barker, Bourne, and Whiffen [12]. Tschamler and Leutner [13] later observed that compounds containing the 1,3-diox-

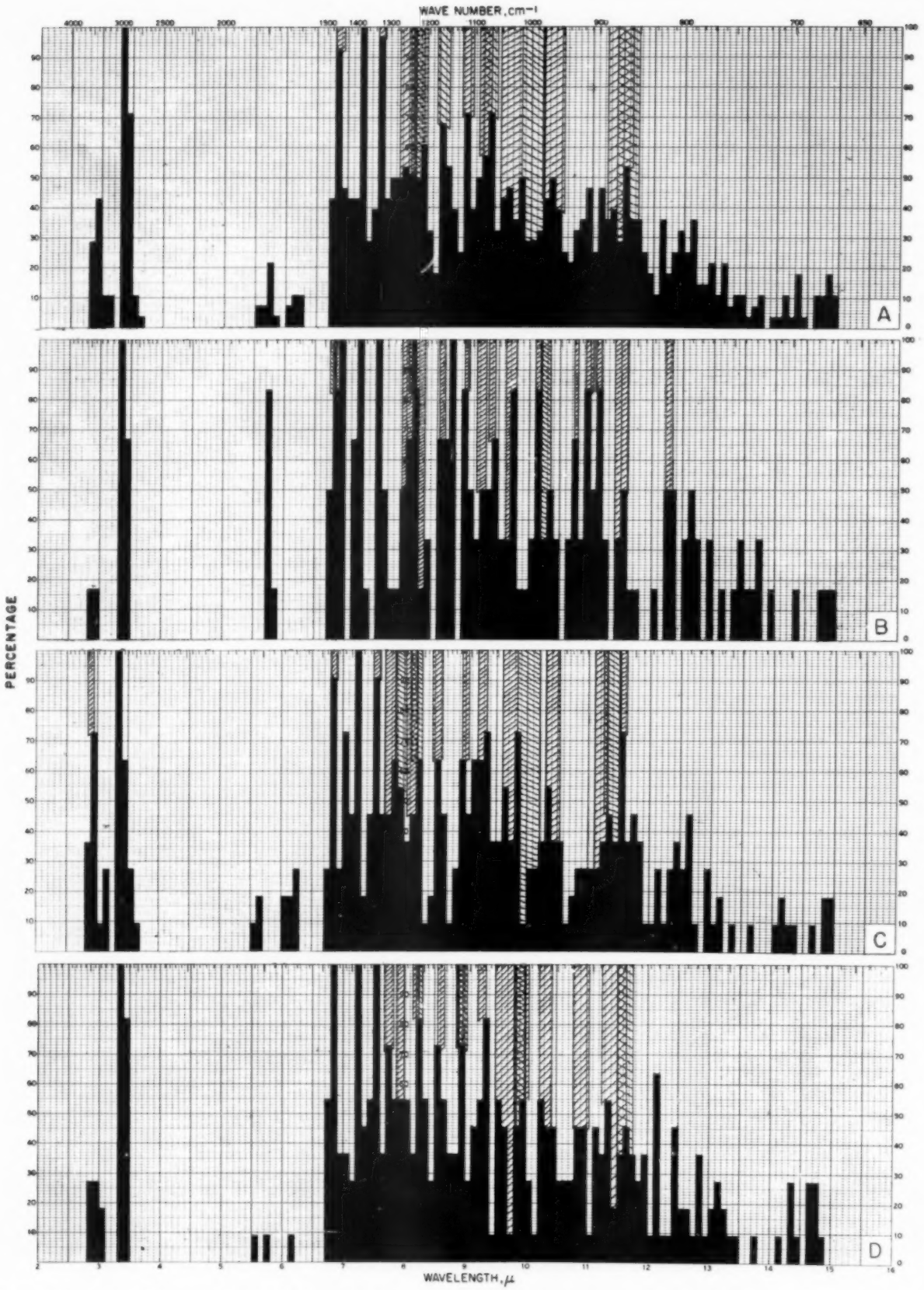

FIGURE 1. *Percentage of the acetals which showed infrared absorption at the various regions of the infrared spectrum (2 to 15 μ).*
A, All of the 28 acetals; **B**, the six methyl orthoacetates; **C**, the eleven mono-*O*-isopropylidene acetals; **D**, the eleven di-*O*-isopropylidene acetals.

TABLE 4. *Absorption bands formerly assigned to the 1,3-dioxolane ring*

Assigned by	Wavenumber (cm^{-1}) of spectral range of absorption bands			
	A	B	C	D
Smith and Anderson [1]				1042
Bergmann & Pinchas tables [2]	1190 to 1151	1151 to 1123	1105 to 1077	1053 to 1038
Bergmann & Pinchas text [2]	1190 to 1158	1143 to 1124	1098 to 1063	1056 to 1038
Barker and co-workers [3]	1173 to 1151	1151 to 1132	1105 to 1077	1053 to 1038
Tschamler and Leutner [4]	doublet between 1160 and 1120		doublet between 1110 and 1050	

References

1. L. I. Smith and R. H. Anderson, J. Org. Chem. **16,** 972 (1951).
2. E. D. Bergmann and S. Pinchas, Rec. trav. chim. **71,** 161 (1952).
3. S. A. Barker, E. J. Bourne, and D. H. Whiffen, Methods of biochemical analysis, vol. 3, p. 219 (Interscience Publishers, Inc., New York, N.Y., 1956).
4. H. Tschamler and R. Leutner, Monatsh. **83,** 1502 (1952).

olane ring generally show four recognizable absorption bands. Table 4 gives a résumé of the assignments of the prior workers.

Our results are in fair agreement with the figures in the tables of Bergmann and Pinchas [11]: (a) Twelve of the compounds in the present study fail to show a band (B) in the 1151- to 1123-cm^{-1} (8.80±0.11 μ) region. However, Bergmann and Pinchas found that the exact location of this band depends more upon the alcoholic than upon the carbonylic residue of the acetal; in possible agreement with this conclusion, a band (B′) is observed at 1126 to 1104 cm^{-1} (8.97±0.09 μ) for our compounds. (b) Two of our compounds show no band (C′) in the 1105- to 1077-cm^{-1} (9.17±0.12 μ) region. (c) Eight of our compounds fail to show a band (D) in the 1053- to 1038-cm^{-1} (9.57±0.07 μ) region.

However, all of our compounds show one or more bands or shoulders in the (A) 1181- to 1153-cm^{-1} (8.57±0.10 μ), (B′) 1126- to 1104-cm^{-1} (8.97±0.09 μ), and (C′) 1093- to 1070-cm^{-1} (9.25±0.10 μ) regions. Except for the spectra of 1,2-*O*-isopropylidene- and 1,2:3,5-di-*O*-isopropylidene-D-xylofuranose (compounds 12 and 18), all the spectra show at least one strong band (D′) at 1055 to 1029 cm^{-1} (9.60±0.12 μ); for the two exceptions, there is a strong band at 1015 cm^{-1} (9.85 μ). This characteristic of the D-xylose derivatives is under further study; the spectra of the anomers and glycosides of D-xylose are known to be exceptional [12]. These four bands (A, B′, C′, and D′) seem to be the most important, but they are not particularly striking inasmuch as they appear in a rather crowded part of the spectrum.

Each substance has an individualistic spectrum useful for identification purposes, but extensive generalization requires great caution. Since many unsubstituted and substituted sugars (and other organic compounds) also show absorption in 2, 3, or even all 4 of the above regions, allocation and interpretation of these bands will be reserved for a more comprehensive study (on a much larger group of sugar derivatives) to be conducted in the same manner.

Many comparisons of limited scope can be made. For example, the spectrum of 1,2:4,5-di-O-isopropylidene-D-fructose (compound 11), a spiro—dioxolane derivative, differs radically from that of its isomer (compound 10) and displays 17 of the 19 bands recorded [14], in the range 2941 to 763 cm^{-1}, for cyclohexane-1,2-di(spiro-2′-1′,3′-dioxolane). In addition to these, it shows 26 other bands in the range 3472 to 726 cm^{-1}.

4.2. Other Absorption Bands

The 28 compounds can be divided into three groups: the methyl orthoacetates, the mono-isopropylidene acetals, and the di-isopropylidene acetals. Bands shown by all the members of each of these groups are given in the crosshatched regions of figure 1 (B, C, and D) and in table 5. It is noted that, in certain regions, more than one interpretation of the data is possible.

Bands shown by all of the compounds in table 1 are shown in the crosshatched regions of figure 1 (A) and in table 5. Selection of one of the alternative ranges exhibited by a subgroup could often be made by intercomparing the ranges for all three subgroups. (Even so, more than one interpretation of ranges for band locations was found possible in certain regions of the spectrum.)

In addition to those mentioned in the preceding section, the following are some of the bands shown by *all* of the compounds, with possible assignments given in parentheses: 3012 to 2967 cm^{-1}, i.e., 3.32 to 3.37 μ (C—H stretching); 1468 to 1439 cm^{-1}, i.e., 6.81 to 6.95 μ (or 1466 to 1437 cm^{-1}, i.e., 6.82 to 6.96 μ), and 1333 to 1312 cm^{-1}, i.e., 7.50 to 7.62 μ (C—H bending); 1391 to 1379 cm^{-1}, i.e., 7.19 to 7.25 μ (or 1385 to 1372 cm^{-1}, i.e., 7.22 to 7.29 μ), often as a doublet (possibly —CH_3 deformation, but these bands are shown by many unsubstituted sugars); 1272 to 1236 cm^{-1}, i.e., 7.86 to 8.09 μ (C—O), and 1244 to 1212 cm^{-1}, i.e., 8.04 to 8.25 μ, or 1232 to 1205 cm^{-1}, i.e., 8.12 to 8.30 μ (C—O stretching); and 889 to 858 cm^{-1}, i.e., 11.25 to 11.66 μ, or 877 to 850 cm^{-1}, i.e., 11.40 to 11.76 μ (1,3-dioxolane ring?). Other bands, which may possibly be correlatable with one or other of these features, were noted at 981.4 to 948.8 cm^{-1}, 824.4 to 793.0 cm^{-1}, and 540.5 to 507.6 cm^{-1}. Some other possibilities noted encompass broader ranges of wavenumber and show overlapping. (They are mentioned in case some of them should prove to be significant, but

TABLE 5. *Bands shown by all of the 1,3-dioxolane derivatives and by all the members of each of the subgroups*

Wavelength (μ) of spectral range of absorption bands			
The six methyl orthoacetates	The eleven mono-isopropylidene acetals	The eleven di-isopropylidene acetals	All of the 28 acetals
	2.86 to 2.95		
3.33 to 3.37	3.32 to 3.37	3.32 to 3.36	3.32 to 3.37
(or 3.34 to 3.39)	(or 3.34 to 3.39)		
(6.75 to 6.84 or)			
6.81 to 6.95	6.82 to 6.92	6.83 to 6.87	6.81 to 6.95
(or 6.83 to 6.96)	6.82 to 6.92	6.83 to 6.87	(or 6.82 to 6.96)
6.95 to 6.97			
7.19 to 7.23	7.20 to 7.25	7.20 to 7.25	7.19 to 7.25
7.26 to 7.29	(or 7.22 to 7.27)	(or 7.22 to 7.28)	(or 7.22 to 7.29)
7.52 to 7.58	7.50 to 7.62	7.50 to 7.59	7.50 to 7.62
	7.69 to 7.88	7.68 to 7.83	
	(7.82 to 7.97 or)		
7.93 to 8.09	7.86 to 8.04	7.88 to 8.02	7.86 to 8.09
7.93 to 8.09	(or 7.91 to 8.12)		
(or 8.04 to 8.15)	(or 8.04 to 8.22)	8.15 to 8.25	(or 8.04 to 8.25)
	(or 8.10 to 8.26)	8.15 to 8.25	
(or 8.12 to 8.30)	(or 8.12 to 8.30)	8.15 to 8.25	(or 8.12 to 8.30)
		(or 8.20 to 8.31)	
8.54 to 8.64	8.47 to 8.63	8.56 to 8.67	8.47 to 8.67
8.72 to 8.79			
		(8.86 to 8.98 or)	
8.95 to 9.03	8.95 to 9.06	8.88 to 9.04	8.88 to 9.06
9.15 to 9.30	9.20 to 9.35	9.22 to 9.35	9.15 to 9.35
9.34 to 9.45	(or 9.27 to 9.39)	(or 9.23 to 9.37)	(or 9.23 to 9.45)
(or 9.35 to 9.48)			
9.62 to 9.79	9.61 to 9.85	9.50 to 9.85	9.50 to 9.85
9.62 to 9.79	(or 9.72 to 9.86)	(or 9.55 to 9.88)	(or 9.55 to 9.88)
		(or 9.82 to 9.98)	
10.10 to 10.21	(or 9.85 to 10.22)	(or 9.85 to 10.06)	(or 9.85 to 10.22)
(or 10.19 to 10.35)	10.32 to 10.54	10.23 to 10.43	(or 10.19 to 10.54)
10.74 to 10.80			
10.93 to 11.05		10.78 to 11.04	
11.08 to 11.18	11.11 to 11.32		
11.40 to 11.61	(or 11.26 to 11.53)	11.25 to 11.66	11.25 to 11.66
11.40 to 11.61	11.52 to 11.63	(or 11.51 to 11.76)	(or 11.40 to 11.76)
12.23 to 12.34			

urther work will be needed in order to test this point.) These ranges are: 664.5 to 612.4 cm^{-1}; 580.4 to 524.9 cm^{-1}; 555.6 to 518.1 cm^{-1}; 532.8 to 493.8 cm^{-1}; 530.8 to 487.1 cm^{-1}; 436.7 to 376.7 cm^{-1}; 428.3 to 365.6 cm^{-1}· 418.4 to 363.0 cm^{-1}; 410.2 to 349.4 cm^{-1}; and 370.1 to 319.0 cm^{-1}.

The following absorption bands were shown only by compounds (in this study) having the structural features mentioned (groups 1, 2, and 4 to 6 of table 3); the wavelengths in microns and the possible assignments are given in parentheses. The acetates showed a band at 1748 to 1739 cm^{-1} (5.72 to 5.75 μ; acetate C=O stretching) and at 607.9 to 598.1 cm^{-1} (16.45 to 16.72 μ; acetate deformation). Those compounds having a hydroxyl group and an ionized carboxyl group showed bands at 3145 to 3125 cm^{-1} (3.18 to 3.20 μ; —OH modified by C=O), at 2786 to 2732 cm^{-1} (3.59 to 3.66 μ; —OH modified by C=O), and at 1637 to 1600 cm^{-1} (6.11 to 6.25 μ; $—COO^-$). The hydrates showed a strong shoulder at 1645 cm^{-1} (6.08 μ; water of crystallization) and a band at 706.2 to 703.7 cm^{-1}. All of the compounds having one or more free hydroxyl groups showed a band at 3472 to 3279 cm^{-1} (2.88 to 3.05 μ; associated alchoholic —O—H, stretching frequency). Compounds 10 and 28 showed a band at 3289 to 3279 cm^{-1} (3.04 to 3.05 μ; H-bonding ?). The lactones showed a band at 1789 to 1764 cm^{-1} (5.59 to 5.67 μ; C=O stretching frequency).

All of the spectra were also studied in regard to the 28 other features listed alphabetically as groups 7 to 34 of table 3. Those compounds having a *m*-dioxane ring showed a band at 310.3 to 307.7 cm^{-1}. The β-glycopyranosides showed bands at 967.1 to 966.2 cm^{-1}, 811.0 to 810.4 cm^{-1}, 646.0 to 644.8 cm^{-1}, and 475.1 to 470.6 cm^{-1}. Those compounds having a free hydroxyl group at carbon atom 1 showed a band at 893.7 to 892.1 cm^{-1} and at 683.1 to 680.7 cm^{-1}. The isopropylidene acetals showed a band at 859.1 to 833.3 cm^{-1}. Those compounds having a sugar ring (including compound 24) showed one or more bands at 914.1 to 884.2 cm^{-1}. (Other possible interpretations are: 900.9 to 878.7 cm^{-1}, or 900.1 to 877.2 cm^{-1}, or 896.9 to 867.3 cm^{-1}, or 892.1 to 861.3 cm^{-1}.) They also showed bands at 653.6 to 611.6 cm^{-1} and at 591.7 to 544 cm^{-1}. Other possible ranges (which, because of the broader range or the overlapping, may not be significant) are: 639.0 to 578.0 cm^{-1}; 584.8 to 540.5 cm^{-1}; and 580.4 to 533.3 cm^{-1}. Further work may throw light on the significance of these bands.

From a study of the infrared absorption spectra of sugars and their derivatives capable of existence in anomeric forms (namely, of compounds in which the hydroxyl group of the hemiacetal carbon atom is, for example, free, acetylated; or involved in glycosidic union), Barker and co-workers [15, 16] were able to recognize certain absorption bands which were considered to be characteristic of the α and β anomers, respectively, of the pyranoid forms. In the present study, the only pyranoid compounds capable of existence as α and β anomers are compounds 5, 6, and 11 (which are, respectively, a β-D-glucoside, a β-D-galactoside, and a D-fructopyranose derivative), and they show bands fitting the assignments called types 1, 2, and 3 by Barker and

co-workers. The other pyranoid derivatives, which cannot exist in anomeric forms, show many of the bands in question; but, as might be expected, these do not fit the structural correlations.

Similarly, of the furanoid derivatives, only compound 23 (and possibly [8] 22) is capable of existence in anomeric forms, and it shows bands fitting the tentative assignments (for furanoid sugars) called types A, C, and D by Barker and Stephens [17]. The other compounds show many of these bands, but they do not fit the structural correlations.

5. Experimental Procedures

5.1. Preparation and Purification of the Compounds

The compounds listed in table 1 were prepared by the methods given in the references cited. For compound 4, the few milligrams of the material remaining from the original preparation of Pigman and Isbell [3] had a melting point somewhat low, but it was apparently in good condition; because of the lack of material for recrystallization, its infrared absorption spectrum (2 to 15 μ) was determined directly, and this showed the presence of a small proportion of free hydroxyl group (band at 3484 cm^{-1}; 2.87 μ). For compounds 21 and 25, the melting points were satisfactory, but insufficient material remained for checking their optical rotations. With these exceptions, each substance was recrystallized or otherwise purified until further treatment caused no change in its melting point or optical rotation. In most cases, these values then agreed with those found in the literature; but where a higher melting point is now given, it is believed that the new values reported in table 1 are correct.

As regards the preparation of compound 12, by the acid hydrolysis of compound 18, a survey of the literature showed that use of 0.16 percent hydrochloric acid [18, 19], 0.2 percent hydrochloric acid [20, 21], 0.04 *N* sulfuric acid [22], and 0.2 *N* sulfuric acid [23] had been recommended; the last concentration cited may be a misprint. Accordingly, a solution of compound 18 (10 g) in 250 ml of 0.05 *N* sulfuric acid was kept at room temperature for 2 hours. The acid was then neutralized by adding barium carbonate (5 g) and shaking until neutral to Congo Red. The suspension was filtered through a layer of Celite plus barium carbonate, and the clear, colorless filtrate was added to barium carbonate (1 g) and evaporated to dryness under diminished pressure at 30° (bath temp.). The mixture of sirup plus solid was extracted with acetone and filtered, and the filtrate was dried with anhydrous sodium sulfate, filtered, and evaporated to dryness under diminished pressure. The resulting sirup was distilled (bp 112° to 114° C at 0.06 mm), affording an almost quantitative yield of a colorless, viscous sirup which completely crystallized spontaneously. Although previous workers [18, 23] have stated that the compound cannot be recrystallized from organic solvents, it may readily be recrystallized from ether (2 vols.) plus heptane (0.2 vol.) on standing in the freezing compartment of the refrigerator.

5.2. Preparation of the Pellets

Samples for spectrophotometric study were prepared in the solid phase, as pellets of the crystalline compound suspended in an alkali-metal halide. The pellets were 9.5 mm in diameter and weighed approximately 100 mg; the weight of sample per 100 mg of potassium chloride (for the 2- to 15-μ region) or per 100 mg of potassium iodide (for the 15- to 40-μ region) is shown in table 6. The accuracy of weighing was not high ($\pm$0.1 mg per mg of sample), but this was relatively unimportant in view of other factors to be discussed. No special precautions, beyond working under an infrared lamp and storage in a vacuum desiccator, were taken for drying the powder, which was hand-ground in a Mullite mortar. The pellets were pressed in a simple, nonevacuable, three-piece die, consisting of a cylindrical body and two plungers (9.5 mm in diameter), similar to one described by Anderson and Woodall [24]. A machine-shop vise was used for applying pressure (estimated to be 20 tons/in.^{2} for pellets of this diameter). Satisfactory pellets were obtained without evacuation. It should be noted that there may have been a slight variation in pellet thickness from pellet to pellet.

TABLE 6. *Conditions for recording the spectra*

Compound	Molecular weight	Concentration for 2- to 15-μ range		Concentration for 15- to 40-μ range	
		mg/100 mg KCl	*mole/kg of mixture*	*mg/100 mg KI*	*mole/kg of mixture*
1	362.35	0.4	0.01_1	2	0.05_4
2	304.30	.4	$.01_3$	2	$.06_4$
3	220.23	.4	$.01_8$		
4	362.35	.4	$.01_1$		
5	650.60	.4	.006	2	.030
6	650.60	.4	.006	2	.030
7	220.23	.5	$.02_3$	2.5	$.1_1$
8	230.26	.4	$.01_7$	2	$.08_5$
9	302.33	.4	$.01_3$	2	$.06_9$
10	260.29	.4	$.01_5$	2	$.07_5$
11	260.29	.4	$.01_5$	2	$.07_5$
12	190.20	.6	$.03_1$	1	$.05_2$
13	220.23	.4	$.01_8$	2	.089
14	220.23	.4	$.01_8$	2	.089
15	240.14	.4	$.01_7$	2	$.08_2$
16	[a] 310.89	.4	[a] $.01_3$	3	[a] $.09_8$
17	[a] 271.26	.4	[a] $.01_4$	2	[a] $.07_2$
18	230.26	1	$.04_3$	2	$.08_5$
19	260.29	0.4	$.01_5$	2	$.07_6$
20	216.20	.4	$.01_8$	2	$.09_1$
21	216.20	.4	$.01_8$	2	$.09_1$
22	190.20	3.5	$.17_8$	4	.20
23	260.29	0.4	$.01_5$	2	$.07_3$
24	258.27	1	$.03_8$	2	$.07_6$
25	190.20	0.8	$.04_2$	4	.20
26	260.29	.4	$.01_5$	2	$.07_5$
27	312.37	1	$.03_2$	3	$.09_6$
28	262.31	0.4	$.01_5$	2	$.07_3$

[a] Equivalent weight.

5.3. Measurement of Infrared Absorption

The spectrograms are shown in figures 2 and 3. Those in the 2- to 15-μ range for compounds 7, 12, 18, 22, 24, 25, and 27 were recorded with a Beckman Model IR4 (double-beam) spectrophotometer equipped with prisms of sodium chloride; they have deliberately been reproduced somewhat differently from

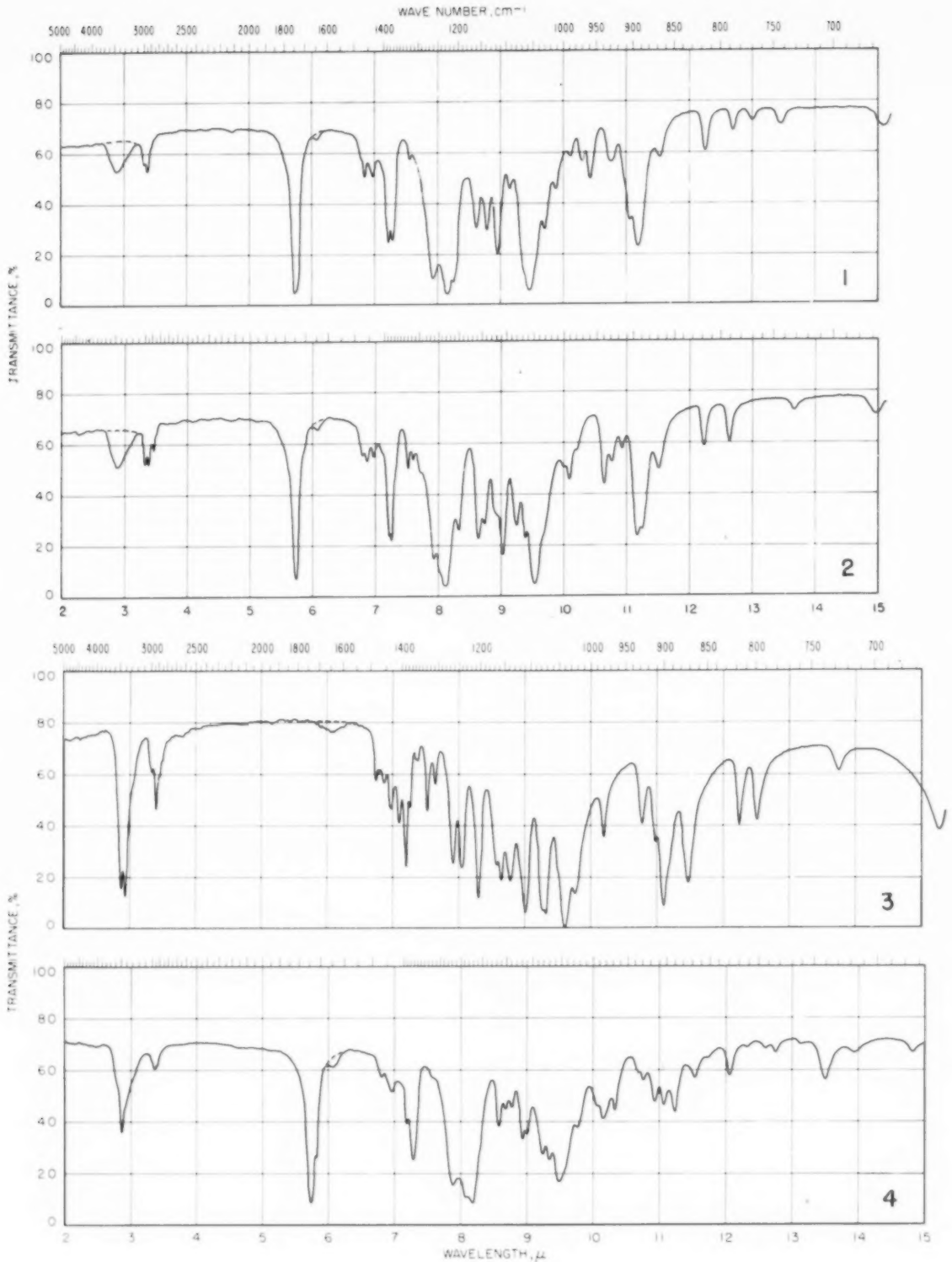

FIGURE 2. *Spectograms of materials in potassium chloride pellets.*

1, D-Mannopyranose 1,2-(methyl orthoacetate) triacetate; **2,** 6-deoxy-L-mannopyranose 1,2-(methyl orthoacetate) diacetate; **3,** 6-deoxy-L-mannopyranose 1,2-(methyl orthoacetate); **4,** D-talopyranose 1,2-(methyl orthoacetate) triacetate.

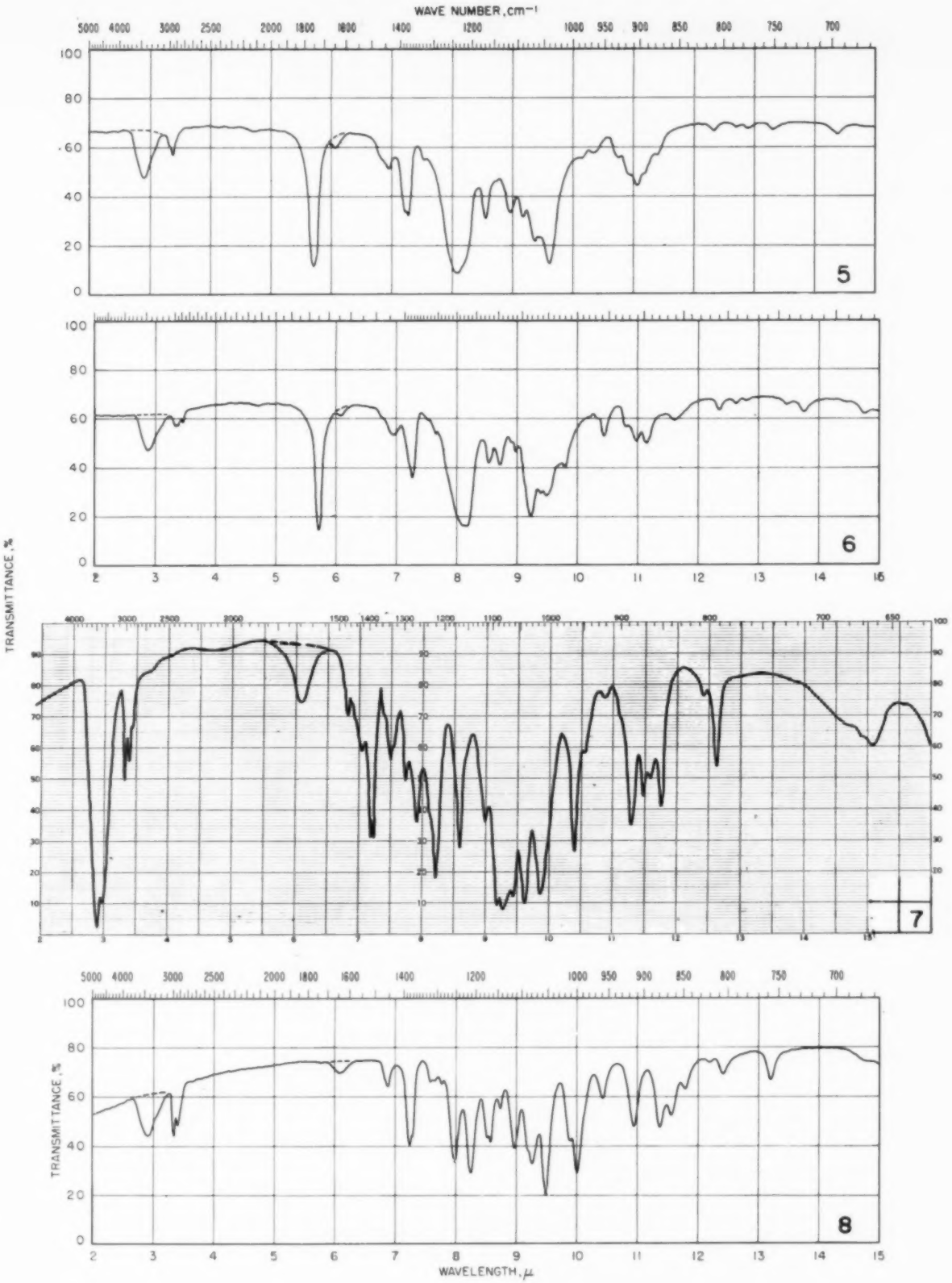

FIGURE 2. *Spectograms of materials in potassium chloride pellets.*—Continued

5, β-D-glucopyranosyl-(1→4)-D-mannopyranose 1,2-(methyl orthoacetate) hexaacetate; **6**, β-D-galactopyranosyl-(1→4)-D-altropyranose 1,2-(methyl orthoacetate) hexaacetate; **7**, 1,2-*O*-isopropylidene-D-galactopyranose; **8**, 1,2:3,4-di-*O*-isopropylidene-L-arabinopyranose.

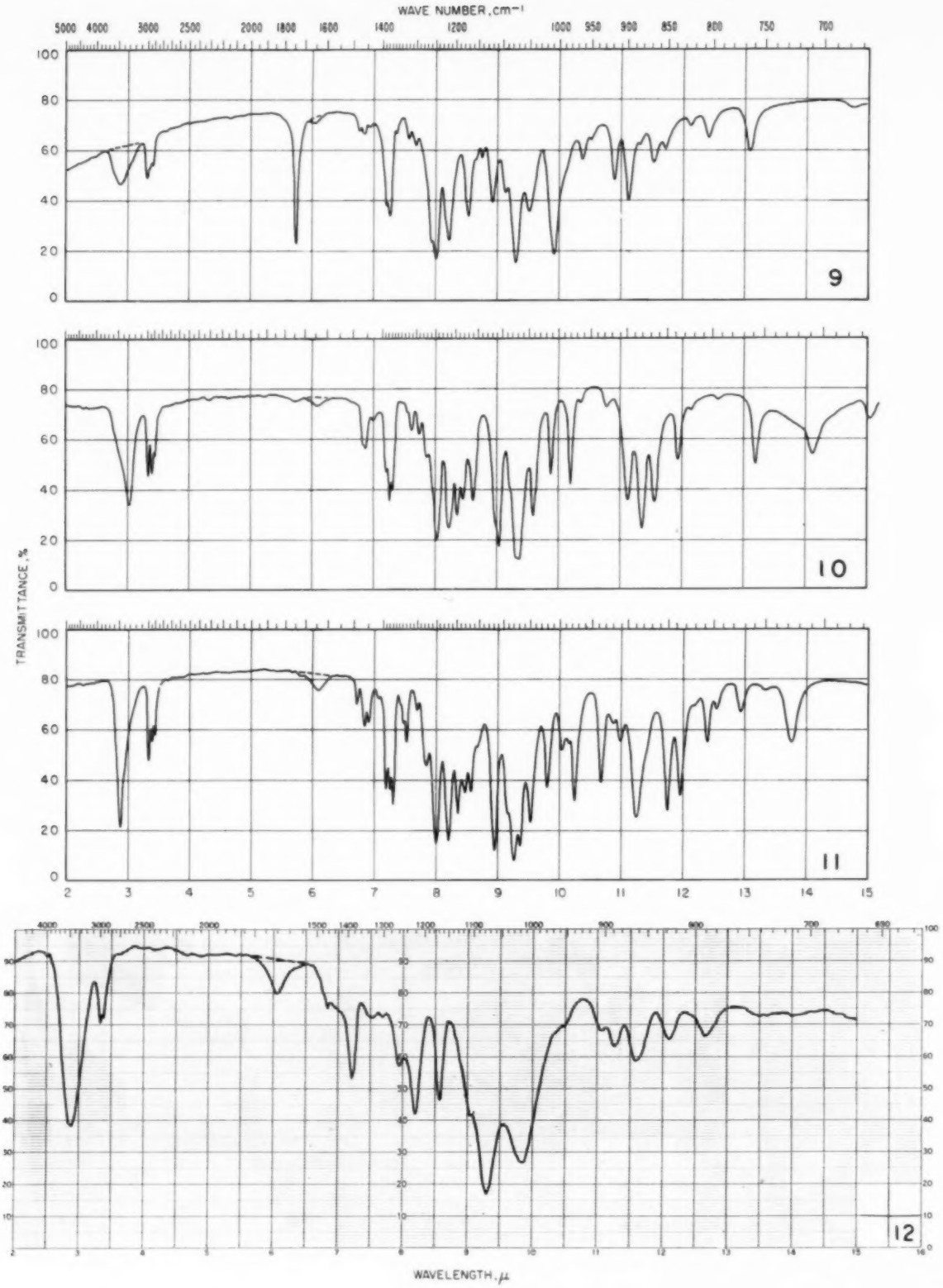

FIGURE 2. *Spectograms of materials in potassium chloride pellets.*—Continued

9, 1,2:3,4-di-*O*-isopropylidene-D-galactopyranose 6-monoacetate; **10,** 2,3:4,5-di-*O*-isopropylidene-D-fructopyranose; **11,** 1,2:4,5-di-*O*-isopropylidene-D-fructopyranose; **12,** 1,2-*O*-isopropylidene-D-xylofuranose.

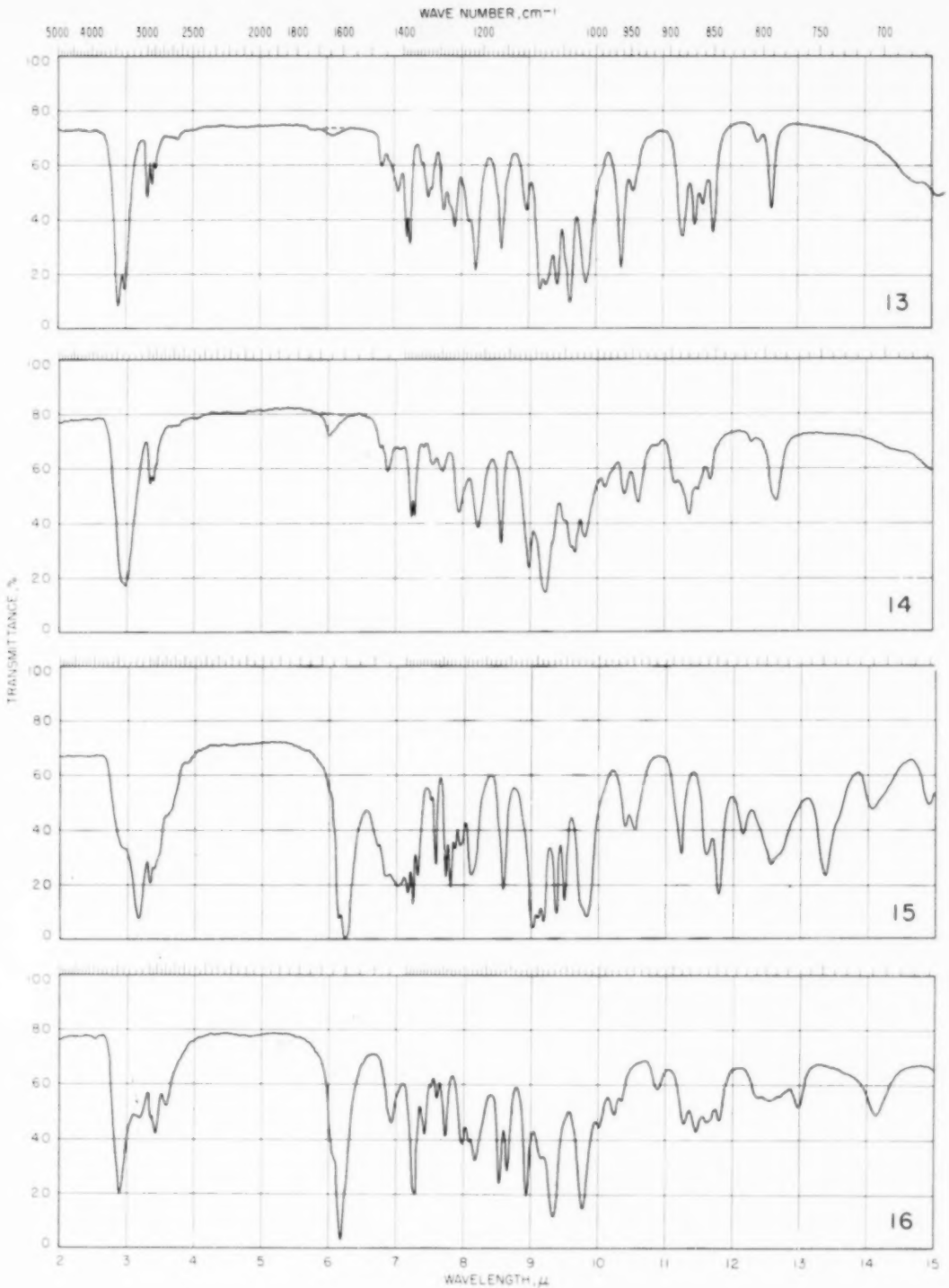

FIGURE 2. *Spectograms of materials in potassium chloride pellets.*—Continued

13, 1,2-*O*-isopropylidene-D-glucofuranose; **14,** 1,2-*O*-isopropylidene-L-idofuranose; **15,** lithium 1,2-*O*-isopropylidene-D-glucofuranuronate; **16,** barium 1,2-*O*-isopropylidene-D-glucofuranuronate monohydrate.

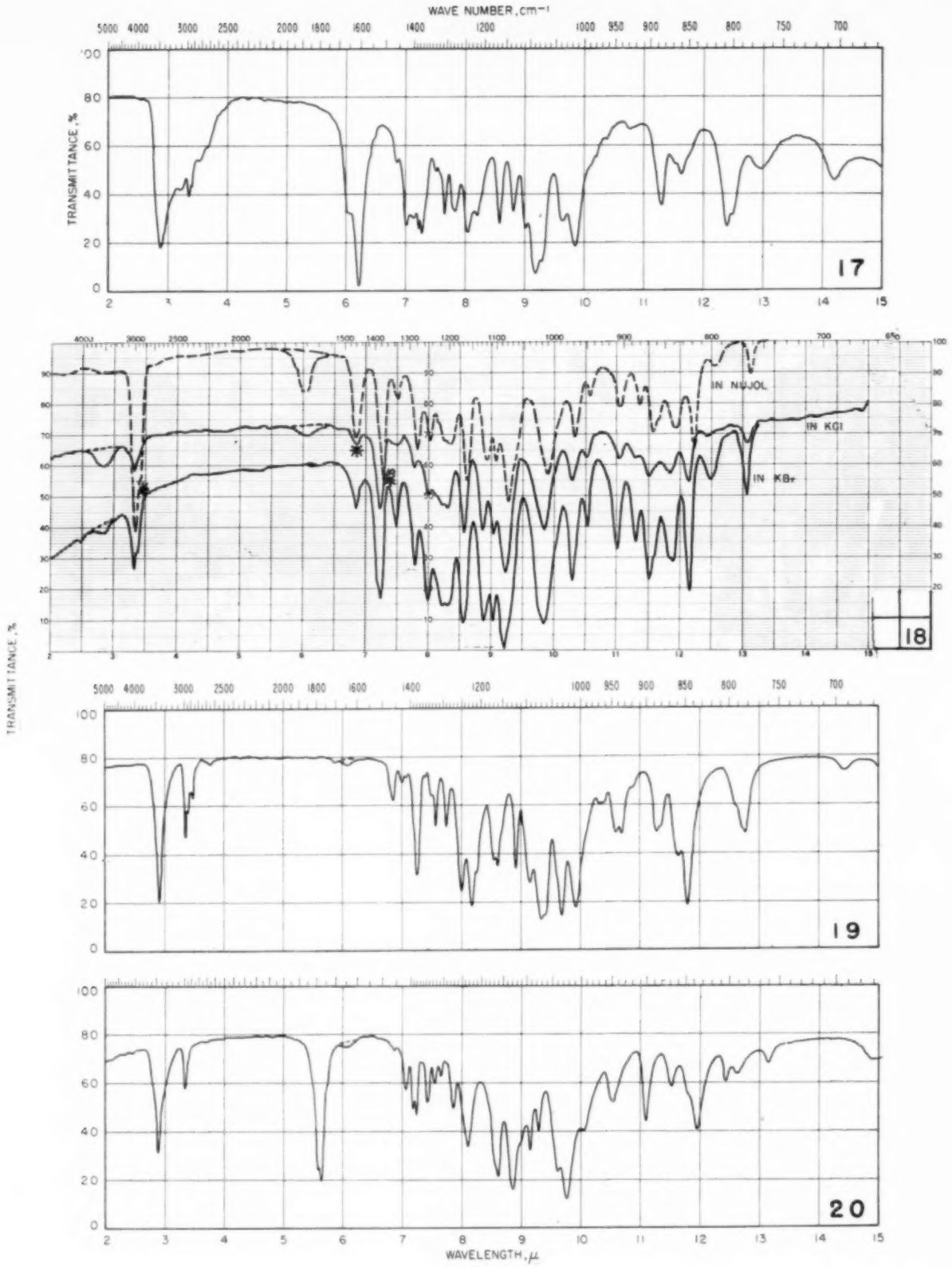

FIGURE 2. *Spectograms of materials in potassium chloride pellets.*—Continued

17, calcium 1,2-*O*-isopropylidene-L-idofuranuronate dihydrate; **18,** 1,2:3,5-di-*O*-isopropylidene-D-xylofuranose; **19,** 1,2:5,6-di-*O*-isopropylidene-D-glucofuranose; **20,** 1,2-*O*-isopropylidene-D-glucofuranurono-6,3-lactone.

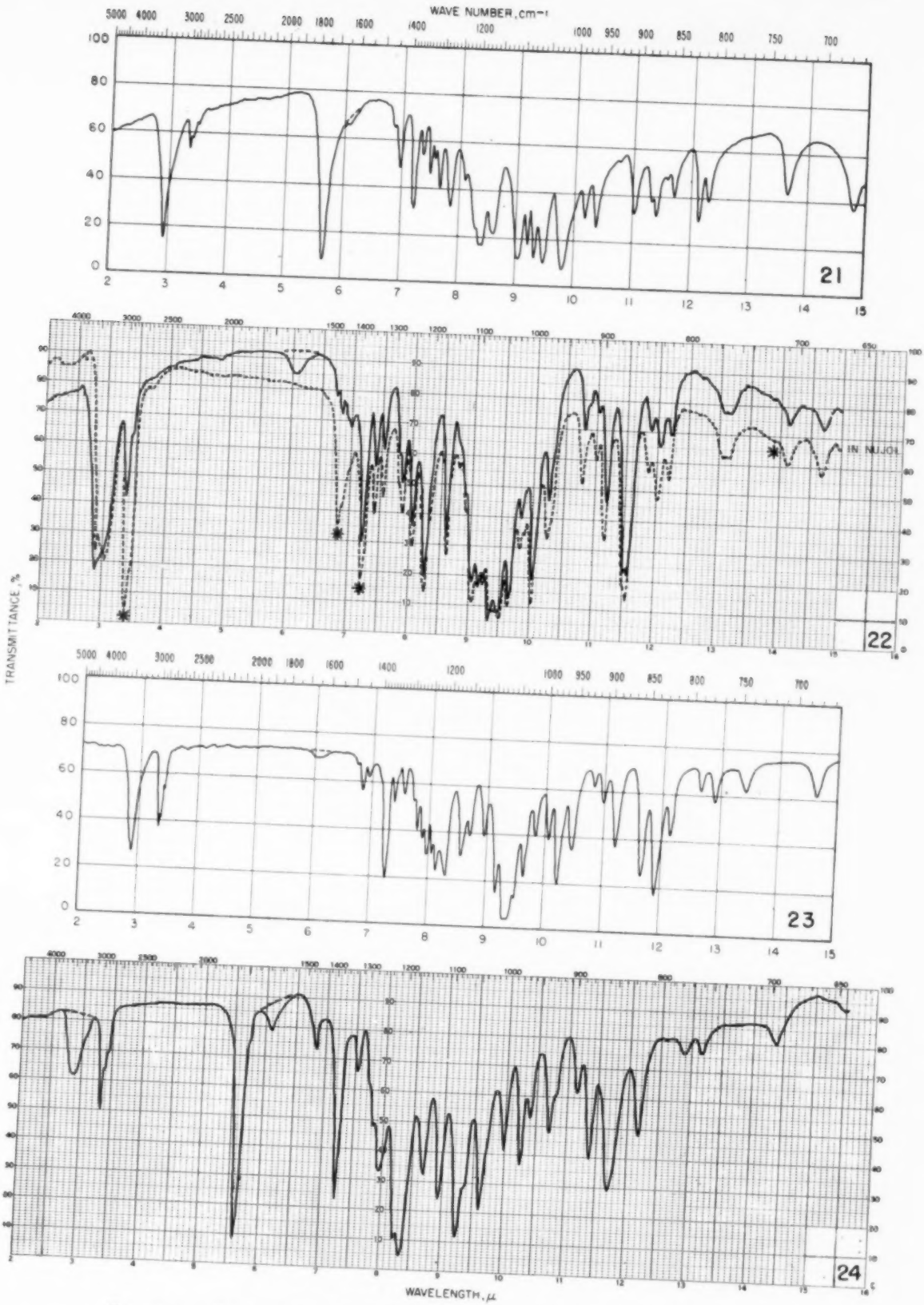

FIGURE 2. *Spectograms of materials in potassium chloride pellets.*—Continued

21, 1,2-*O*-isopropylidene-L-idofuranurono-6,3-lactone; **22,** 2,3(or 3,5)-*O*-isopropylidene-D-lyxo(furano?)se; **23,** 2,3:5,6-di-*O*-isopropylidene-D-mannofuranose; **24,** 2,3:5,6-di-*O*-isopropylidene-D-mannono-1,4-lactone.

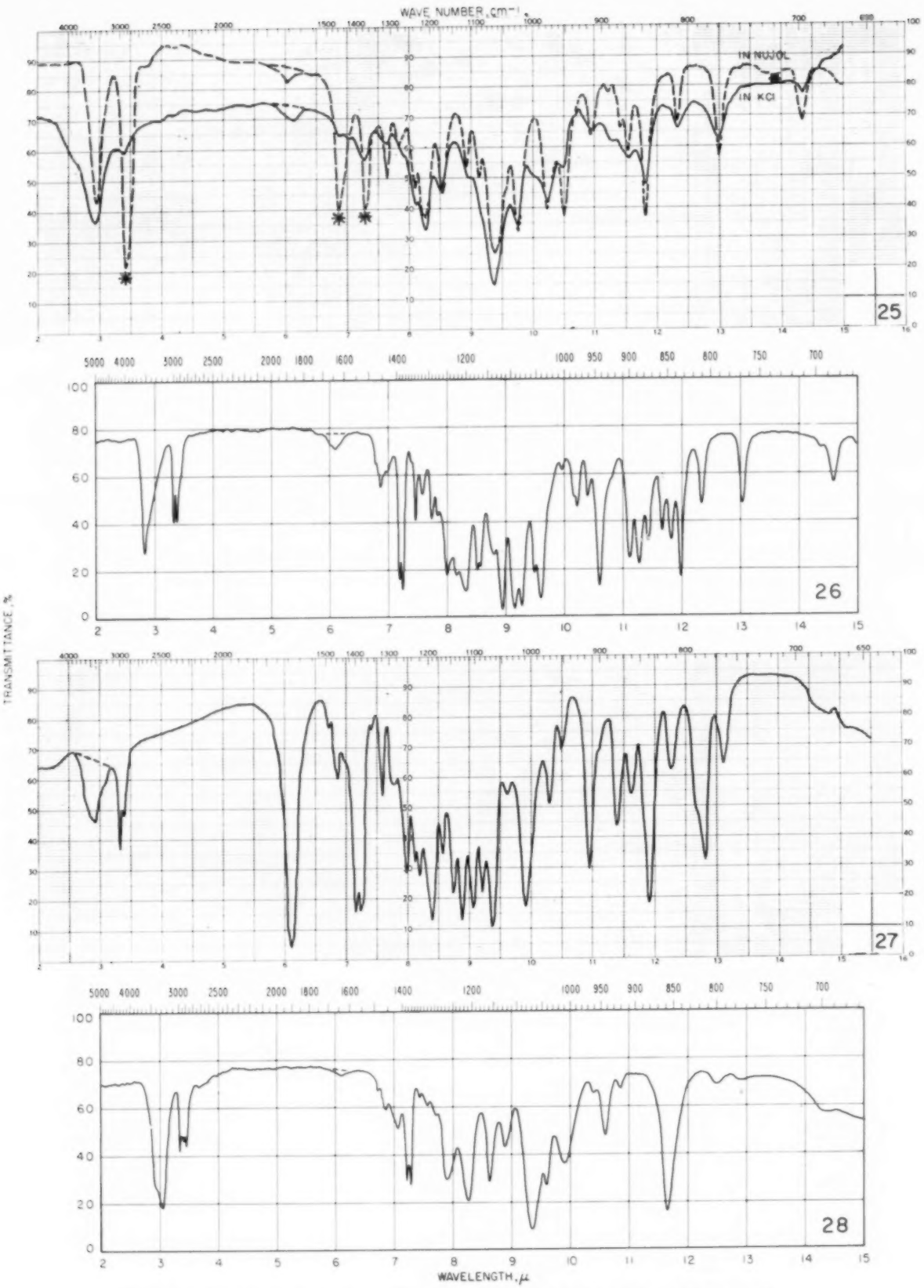

FIGURE 2. *Spectograms of materials in potassium chloride pellets.*—Continued

25, 2,3-*O*-isopropylidene-D-*three*-pentulofuranose; **26,** 2,3:4,6-di-*O*-isopropylidene-L-*xylo*-hexulofuranose; **27,** potassium 2,3:4,6-di-*O*-isopropylidene-L-*xylo*-hexulofuranonate; **28,** 1,2:5,6-di-*O*-isopropylidene-D-mannitol.

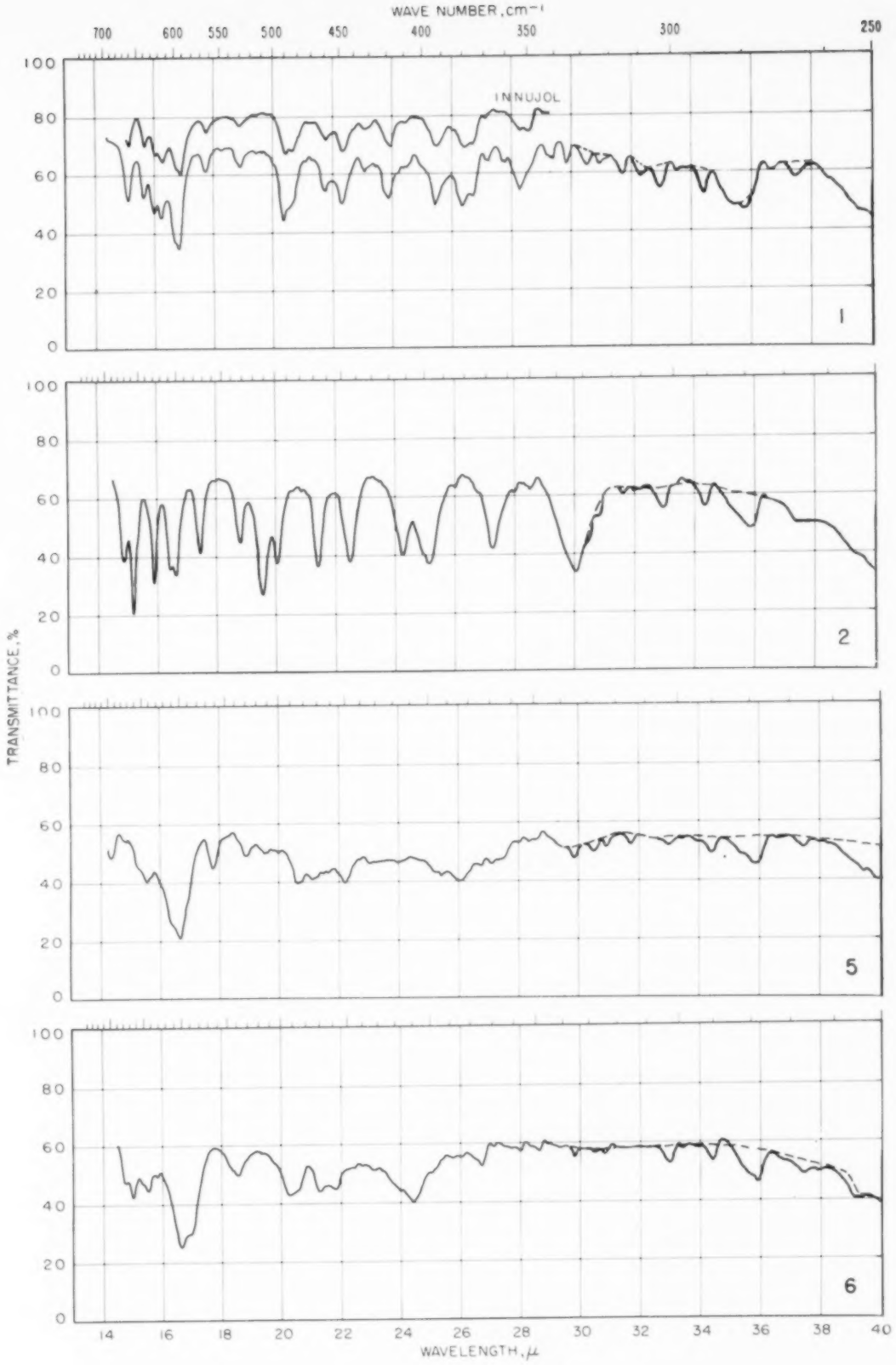

FIGURE 3. *Spectograms of materials in potassium iodide pellets.*

1, D-Mannopyranose 1,2-(methyl orthoacetate) triacetate; **2,** 6-deoxy-L-mannopyranose 1,2-(methyl orthoacetate) diacetate; **5,** β-D-glucopyranosyl-(1→4)-D-mannopyranose 1,2-(methyl orthoacetate) hexaacetate; **6,** β-D-galactopyranosyl-(1→4)-D-altropyranose 1,2-(methyl orthoacetate) hexaacetate.

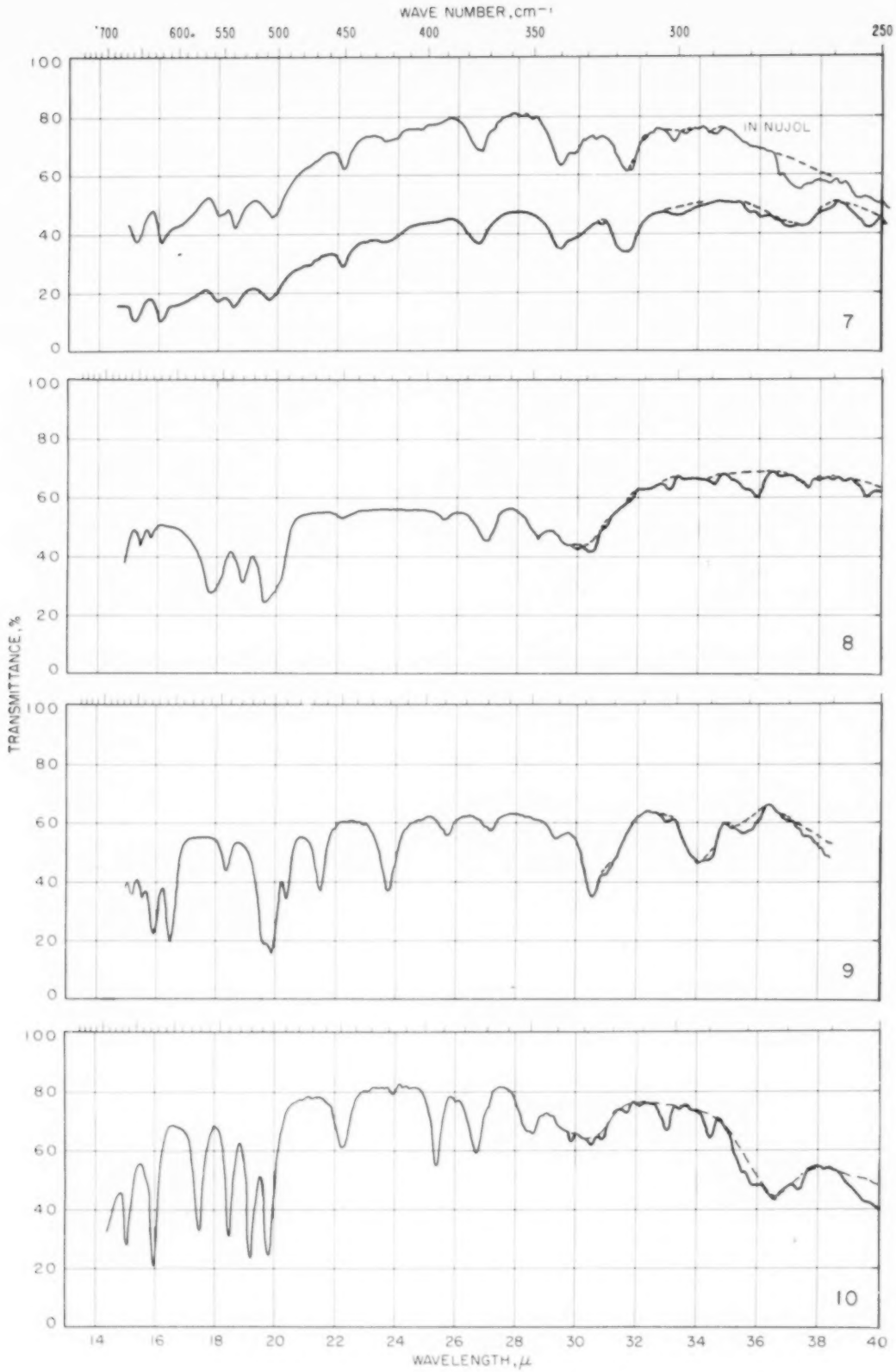

FIGURE 3. *Spectograms of materials in potassium iodide pellets.*—Continued

7, 1,2-*O*-isopropylidene-D-galactopyranose; **8,** 1,2:3,4-di-*O*-isopropylidene-L-arabinopyranose; **9,** 1,2:3,4-di-*O*-isopropylidene-D-galactopyranose 6-monoacetate; **10,** 2,3:4,5-di-*O*-isopropylidene-D-fructopyranose.

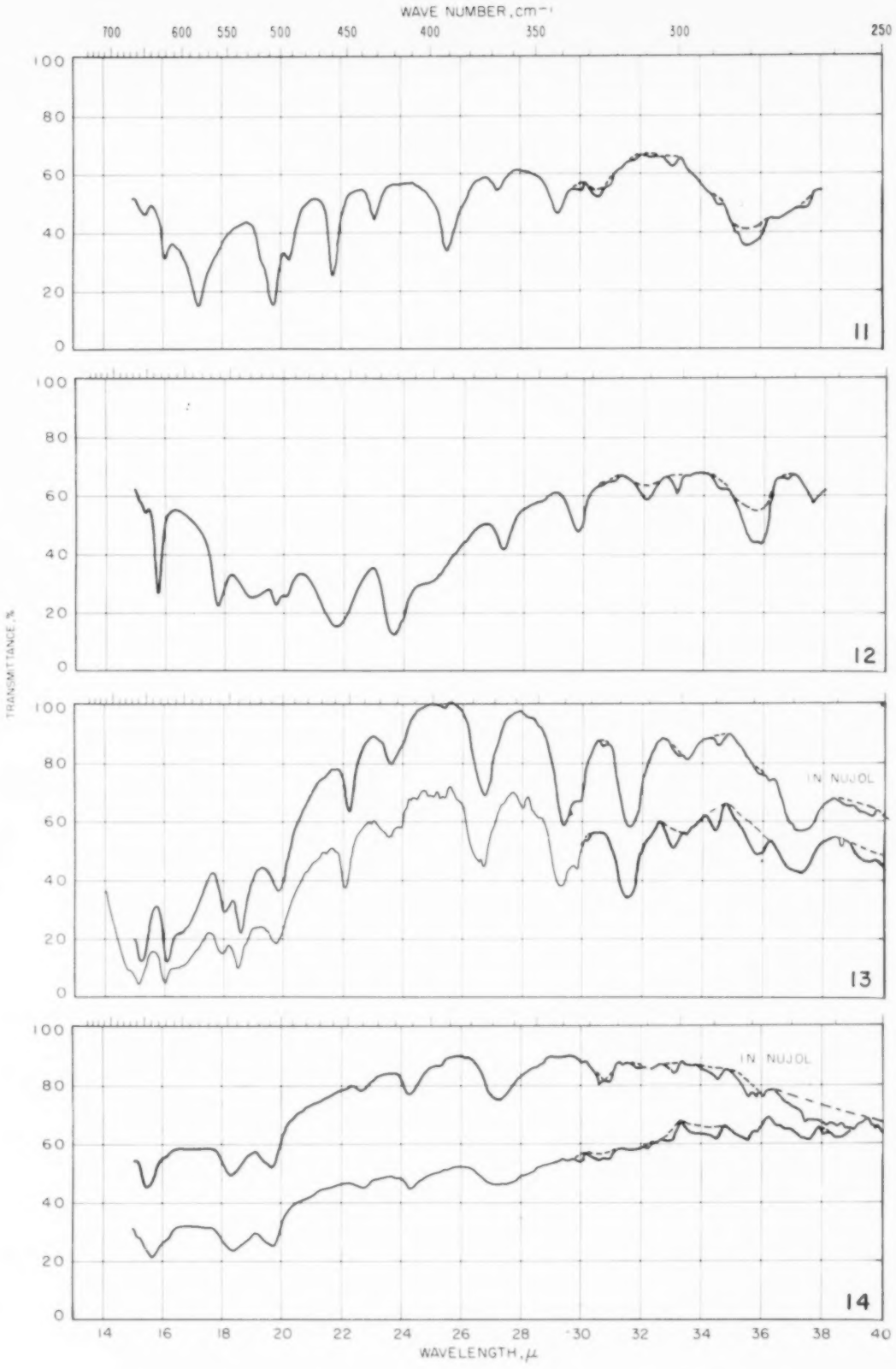

FIGURE 3. *Spectograms of materials in potassium iodide pellets.*—Continued

11, 1,2:4,5-di-*O*-isopropylidene-D-fructopyranose; **12,** 1,2-*O*-isopropylidene-D-xylofuranose; **13,** 1,2-*O*-isopropylidene-D-glucofuranose; **14,** 1,2-*O*-isopropylidene-L-idofuranose.

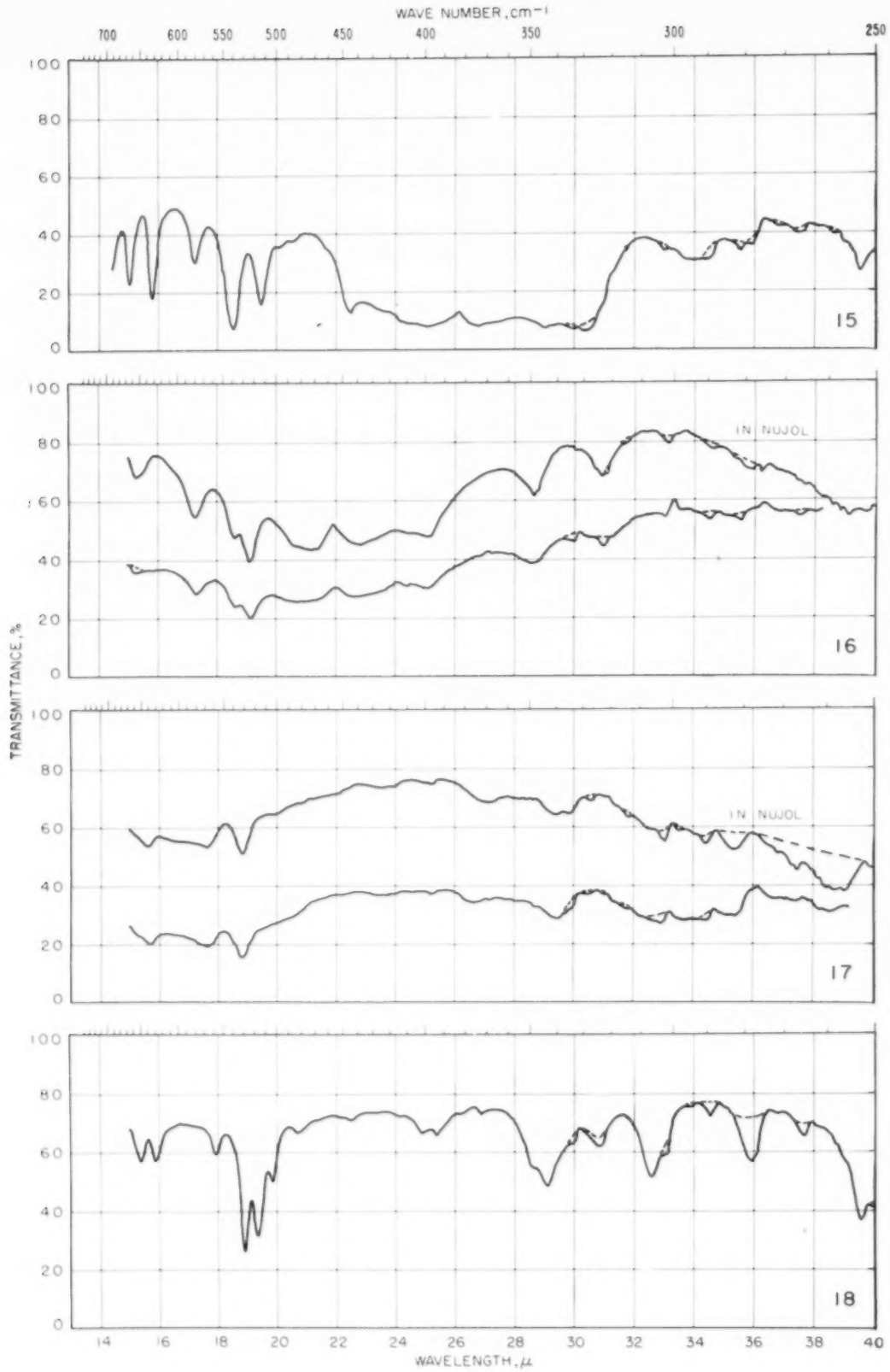

FIGURE 3. *Spectograms of materials in potassium iodide pellets.*—Continued

15, Lithium 1,2-*O*-isopropylidene-D-glucofuranuronate; **16,** barium 1,2-*O*-isopropylidene-D-glucofuranuronate monohydrate; **17,** calcium 1,2-*O*-isopropylidene-L-idofuranuronate dihydrate; **18,** 1,2:3,5-di-*O*-isopropylidene-D-xylofuranose.

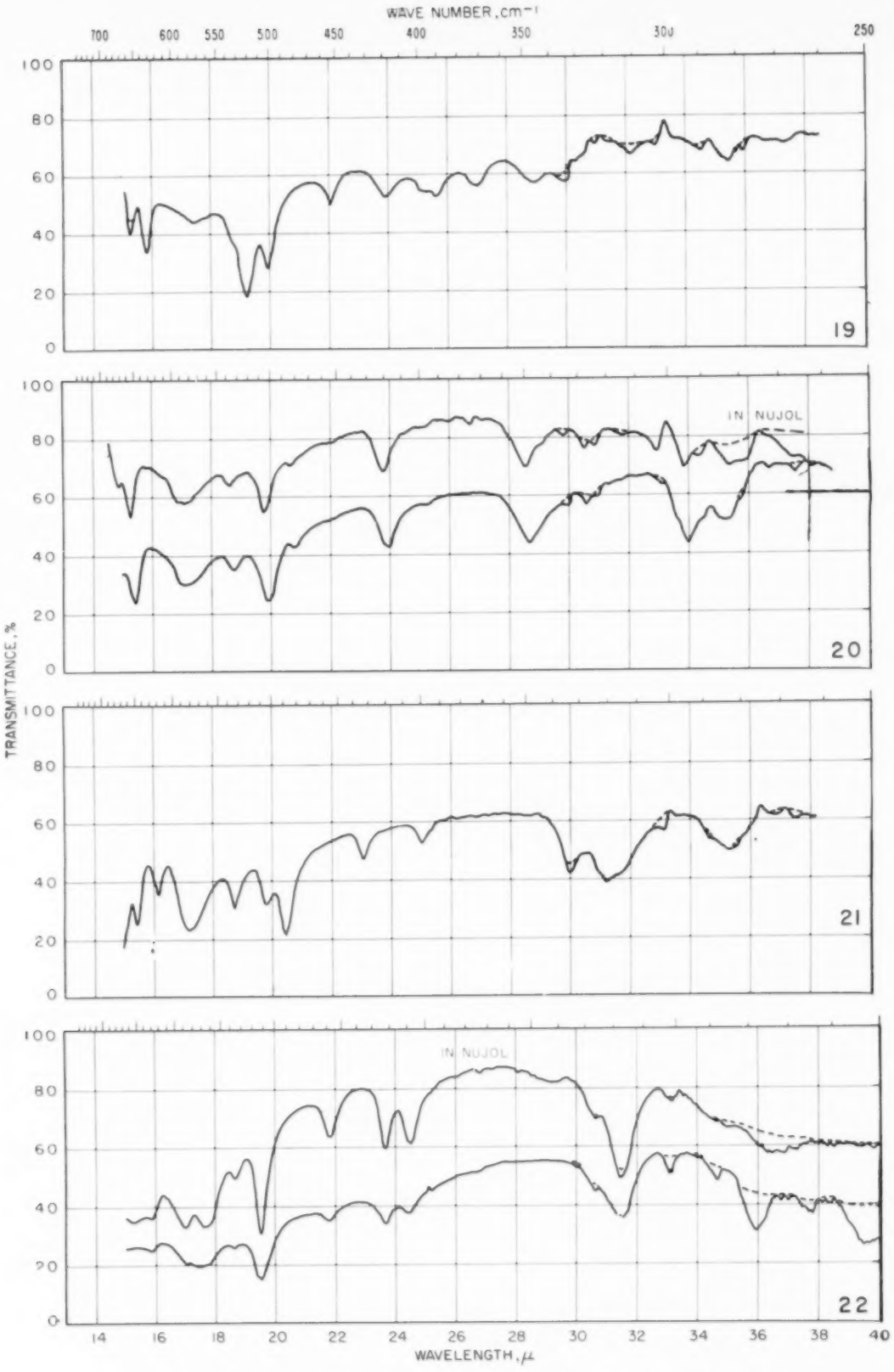

FIGURE 3. *Spectograms of materials in potassium iodide pellets.*—Continued

19, 1,2:5,6-di-*O*-isopropylidene-D-glucofuranose; **20,** 1,2-*O*-isopropylidene-D-glucofuranurono-6,3-lactone; **21,** 1,2-*O*-isopropylidene-L-idofuranurono-6,3-lactone; **22,** 2,3(or 3,5)-*O*-isopropylidene-D-lyxo(furano?)se.

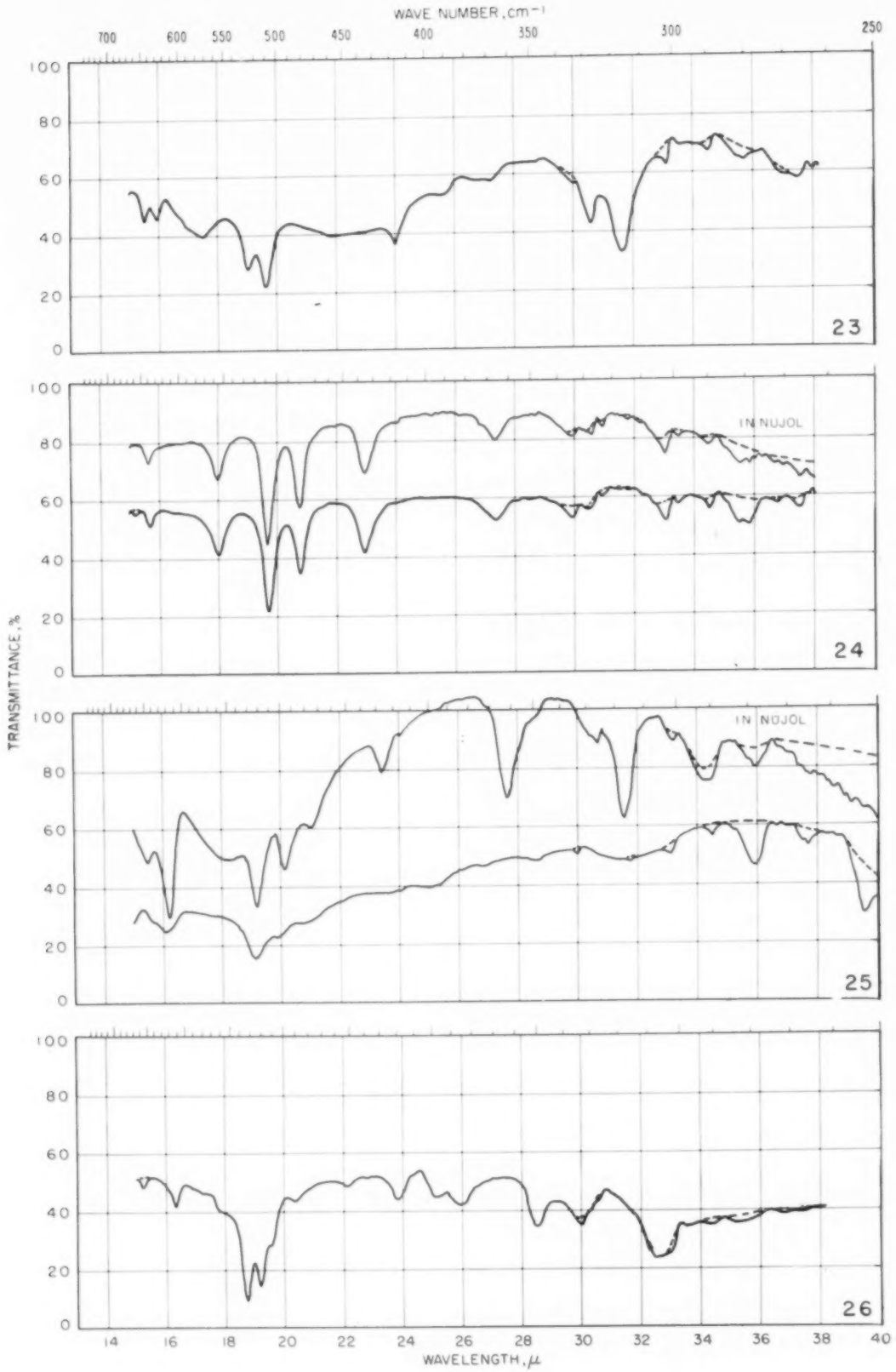

FIGURE 3. *Spectograms of materials in potassium iodide pellets.*—Continued

23, 2,3:5,6-di-*O*-isopropylidene-D-mannofuranose; **24,** 2,3:5,6-di-*O*-isopropylidene-D-mannono-1,4-lactone; **25,** 2,3-*O*-isopropylidene-D-*threo*-pentulofuranose; **26** 2,3:4,6-di-*O*-isopropylidene-L-*xylo*-hexulofuranose.

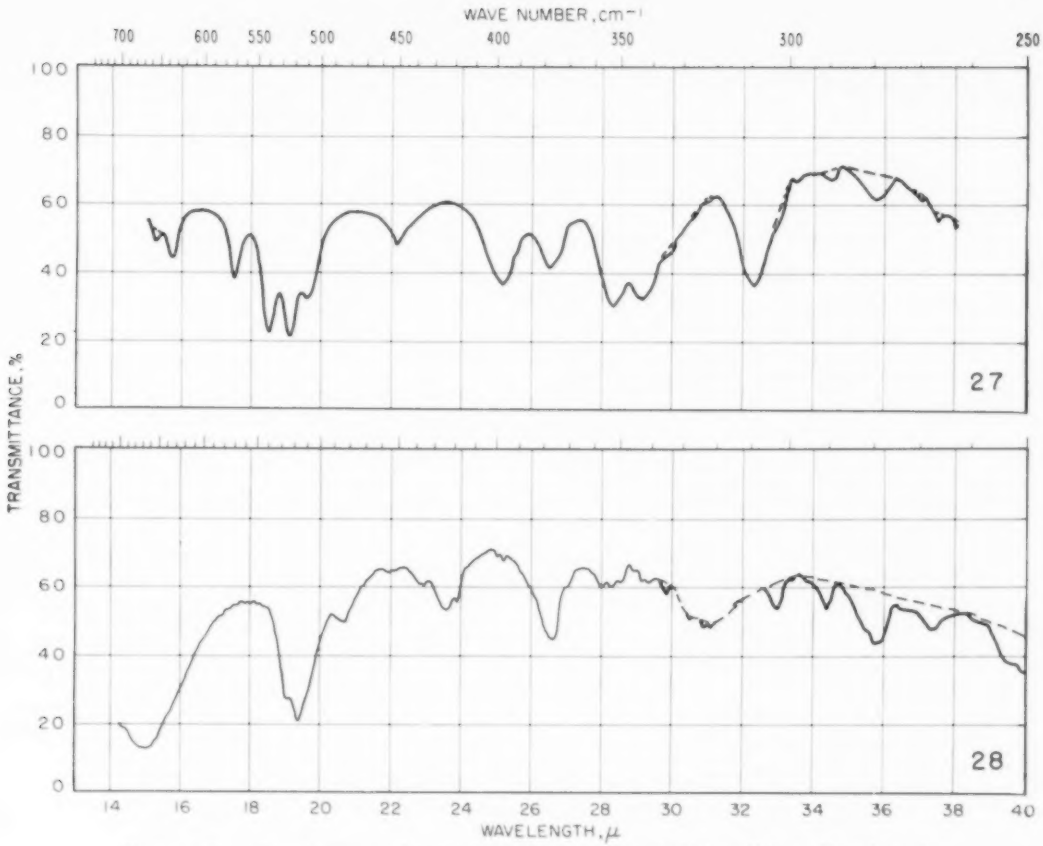

FIGURE 3. *Spectograms of materials in potassium iodide pellets.*—Continued

27, Potassium 2,3:4,6-di-*O*-isopropylidene-L-*xylo*-hexulofuranonate; **28,** 1,2:5,6-di-*O*-isopropylidene-D-mannitol.

the rest of the spectra. All the other spectrograms were recorded with a Perkin-Elmer Model 21 (double-beam) spectrophotometer equipped with a prism of sodium chloride (for the 2- to 15-μ range) and of cesium bromide (for the 15- to 40-μ range). The use of these two prisms was found to be adequate for obtaining survey or identification spectra encompassing the entire 2- to 40-μ range, because we have found that the resolution obtainable with a cesium bromide prism is not much inferior to that given by a potassium bromide prism in the 15- to 20-μ range and is about its equal in the 20- to 25-μ range. By replacing the usual, stray-radiation filter-turret with one containing retractable filters (Reststrahlen mirrors) of lithium fluoride (for the 15- to 30-μ region) and of calcium fluoride (for the 30- to 40-μ region), the stray radiation (encountered in the 15- to 40-μ region when a prism of cesium bromide is used) was virtually eliminated for the 15- to 34-μ range, and reduced to one percent at 36.5 μ and to two percent at 38 μ. No pellet blank was inserted and, indeed, this is not at present practical for the far infrared, because insufficient energy is available for that region.

In the presence of stray radiation, it is not in general possible to achieve complete compensation for substances, such as water vapor, common to the reference and sample beams of the spectrophotometer. The spectra were recorded without compensation (in the reference beam) for reflection or scatter by the pellet, or for absorption by traces of moisture in the sugar derivative or in the alkali-metal halide. Consequently, in the 2- to 15-μ range, a small amount of absorption attributable to water was observed at 2.9 and 6.1 μ. Attention is drawn to these regions by means of dashed lines.

Similarly, some uncompensated absorption by atmospheric water vapor was evident in the far-infrared curves, and the spectral region beyond about 34 μ was doubtful in the sense that weak bands might not be observed because of the superimposed (uncompensated) bands due to water. Hence, these regions are drawn on the spectrograms with dashed lines, inserted after consideration of the curves (shown in fig. 4) obtained for potassium iodide, moist potassium iodide, and Nujol. These dashed lines are merely precautionary; they should not be interpreted quantitatively.

In the 2- to 15-μ range, the accuracy of the wavelength readings was better than ± 0.02 μ; in the 15- to 40 μ range, the accuracy was within ± 0.05 μ.

Because of the possibility of interaction of the various compounds with the pelleting halide under high pressure, the spectra of typical compounds were also recorded in a Nujol mull (requiring no pressure) for comparison. On one occasion, compound 20 gave visual (development of color) and spectrographic evidence of interaction with potassium iodide and, to a smaller extent, with potassium bromide, but not with potassium chloride; however, this behavior was not observed on repetition with fresh samples of the halides.

The spectra (2 to 15 μ) given for compound 18 illustrate how bands exhibited by a compound suspended in potassium chloride can be obscured (by the bands of Nujol) when a Nujol mull is employed. Another reason for preferring the alkali-halide pellets

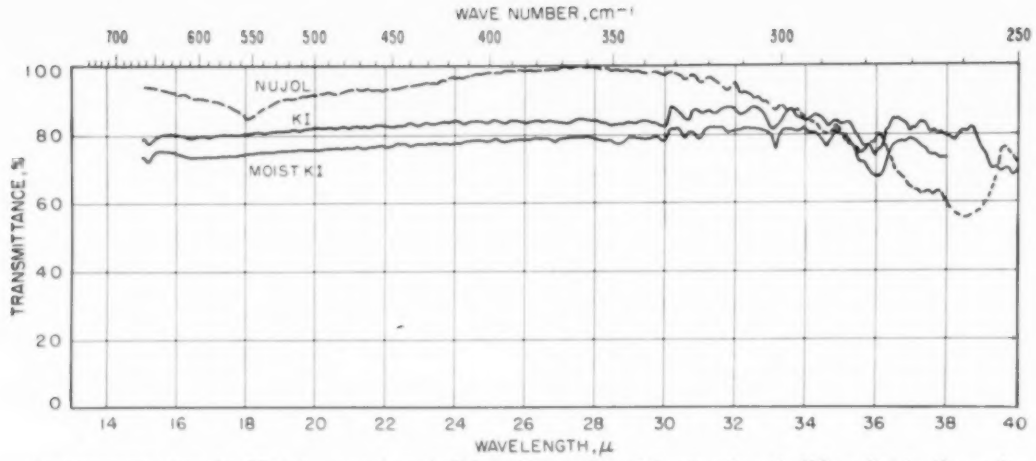

FIGURE 4. *Spectograms given by Nujol, potassium iodide pellet, and moist potassium iodide pellet in the region 15 to 40 μ.*

is that some of the compounds studied are not sufficiently soluble in such solvents as dioxane, carbon disulfide, chloroform, or carbon tetrachloride to afford solutions concentrated enough for recording of satisfactory infrared absorption spectra.

In table 6 are shown the calculated concentrations, in mole per kilogram of alkali-metal halide, of the various pellets. These varied rather widely because of (a) the range in molecular weight of the compounds and (b) the different concentrations (in milligram per milligram of halide) which were found necessary for adequate recording of the spectra. As a consequence, comparisons of intensity of absorption, from one compound to another, can only be true and quantitative where the concentration (in mole per kilogram) is the same. Intercomparisons made for the other compounds are relative and qualitative as regards the intensity of the bands, although the positions of the bands (in microns) may properly be compared.

Insufficient material was available for recording the spectra of compounds 3 and 4 in the 15- to 40-μ region.

5.4. Spectra Measured Under Different Conditions

The infrared absorption spectra of crystalline materials show more bands than the spectra of the same compounds in solution. [This is because, for the solid, the following factors are operative: (1) A removal of degeneracies by perturbations from lattice forces, (2) an intensification of overtones and combination vibrations, and (3) occurrence of combination vibrations between molecular and lattice modes in the solid.]

The spectra (in the 2- to 15-μ region) of compounds 1 and 2 in carbon tetrachloride and in dioxane had been published previously [25]; those given in pellets of potassium chloride for the same region of wavelength are shown in figure 2. A comparison of the relative complexity of the spectra for the solutions and pellets of compounds 1 and 2 (as well as of many other sugar derivatives yet to be published) shows the above-mentioned effect.

The authors express their gratitude to Harriet L. Frush, J. D. Moyer, and R. Schaffer for providing samples of certain of the compounds used in this study; to Alex Cohen for technical assistance; and to J. J. Comeford and F. P. Czech for recording some of the infrared absorption spectra.

6. References

[1] H. S. Isbell, J. Research NBS **57,** 171 (1956) RP2707.
[2] H. S. Isbell, BS J. Research **7,** 1115 (1931) RP392.
[3] W. W. Pigman and H. S. Isbell, J. Research NBS **19,** 189 (1937) RP1021.
[4] H. L. Frush and H. S. Isbell, J. Research NBS **27,** 413 (1941) RP1429.
[5] J. A. Mills, Advances in Carbohydrate Chem. **10,** 18 (1955).
[6] H. S. Isbell, Ann. Rev. Biochem. **9,** 65 (1940).
[7] V. Boekelheide, L. Liberman, J. Figueras, C. Krespan, F. C. Pennington, and D. S. Tarbell, J. Am. Chem. Soc. **71,** 3303 (1949).
[8] L. P. Kuhn, Anal. Chem. **22,** 276 (1950).
[9] L. I. Smith and R. H. Anderson, J. Org. Chem. **16,** 972 (1951).
[10] R. H. Anderson, Ph. D. Thesis, University of Minnesota, 1950.
[11] E. D. Bergmann and S. Pinchas, Rec. trav. chim. **71,** 161 (1952).
[12] S. A. Barker, E. J. Bourne, and D. H. Whiffen, Methods of Biochem. Anal., vol. 3, p. 219 (Interscience Publishers, Inc., New York, N.Y., 1956).
[13] H. Tschamler and R. Leutner, Monatsh. **83,** 1502 (1952).
[14] R. H. Jaeger and H. Smith, J. Chem. Soc. **1955,** 160.
[15] S. A. Barker, E. J. Bourne, M. Stacey, and D. H. Whiffen, J. Chem. Soc. **1954,** 171.
[16] S. A. Barker, E. J. Bourne, R. Stephens, and D. H. Whiffen, J. Chem. Soc. **1954,** 3468.
[17] S. A. Barker and R. Stephens, J. Chem. Soc. **1954,** 4550.
[18] O. Svanberg and K. Sjöberg, Ber. deut. chem. Ges. **56,** 863 (1923).
[19] H. Müller and T. Reichstein, Helv. Chim. Acta **21,** 251 (1938).
[20] O. Svanberg, Ber. deut. chem. Ges. **56,** 2195 (1923).
[21] W. N. Haworth and C. R. Porter, J. Chem. Soc. **1928,** 611.
[22] K. Freudenberg, H. Molter, and G. Dietrich, Chem. Ber. **80,** 53 (1947).
[23] P. A. Levene and A. L. Raymond, J. Biol. Chem. **102,** 317 (1933).
[24] D. H. Anderson and N. B. Woodall, Anal. Chem. **25,** 1906 (1953).
[25] H. S. Isbell, F. A. Smith, E. C. Creitz, H. L. Frush, J. D. Moyer, and J. E. Stewart, J. Research NBS **59,** 41 (1957) RP2772.

WASHINGTON, January 29, 1959

Journal of Research of the National Bureau of Standards Vol. 62, No. 6, June 1959 Research Paper 2961

Earth Currents Near a Top-Loaded Monopole Antenna With Special Regard to Electrically Small L- and T-Antennas

H. Lottrup Knudsen

An investigation has been made of the ground currents near a top-loaded monopole with nonazimuthal symmetry. Formulas have been developed for the surface current density produced by an inclined, straight wire over a horizontal ground plane for an arbitrary current distribution on the antenna. Working formulas have been developed and numerical calculations of the surface current density on the ground plane have been carried out for the case of a small antenna with a linear current distribution. These results have been used for the calculation of the contribution to the surface current density due to the top loading in the case of an L-antenna and in the case of a T-antenna. In each case both the absolute value of the surface current density arising from the top loading and the relative value of its ϕ-component have been plotted, as it may be expected that this component under certain circumstances may be important in calculating the ground losses in the case of a system of radial ground wires.

1. Introduction

Low-frequency and very-low-frequency antennas often consist of a vertical wire with a top loading of inclined, or in a special case, horizontal, wires radiating from the top of the vertical member as shown in figure 1a. In order to reduce the losses in the ground around the antenna, caused by the currents induced in the earth, a system of ground wires is generally used. As the ground currents have essentially a radial direction, it is a common practice to let the ground wires point radially outwards from the base of the antenna.

In the far zone field of the antenna the main contribution to the field comes from the vertical wire. If the top loading is horizontal, the ratio of the contribution to the field coming from the horizontal wires to the contribution coming from the vertical wire tends toward zero, as the distance from the antenna goes toward infinity. Also in calculating the ground currents and the ground losses, i.e., in calculating the field at the ground near the antenna, it has generally been assumed without proof, that the contribution from the top loading is insignificant. Recently Wait [1] has investigated this question. In his investigation he assumes that the top loading may be replaced by a cone, or, in the special case of a horizontal top loading, by a disk; i.e., he assumes perfect rotational symmetry. In his investigation, Wait arrives at the result that under usually existing circumstances the top loading contributes only to a small extent to the currents and losses in the ground.

However, as has been pointed out by Wait, when the number of wires in the top loading is very small, say one, as in the case of the L-antenna, or two, as in the case of the T-antenna, the top loading may furnish a circumferential component of the ground current, which, although small, may contribute considerably to the ground losses, as it is perpendicular to the radial ground wires. It seems, therefore, justified to carry out an investigation of the ground current excited by a top loading consisting of only a few wires and to compare it with the contribution from the vertical wire. This is the object of the present paper. Whereas formulas for the ground current have been worked out for the general case, working formulas and numerical calculations are given only for the case where the antenna is small compared to the wavelength.

The theory has been developed under the assumption that the current distribution on the antenna including that on top loading is known. For antennas that are short compared to the wavelength, we may make the following statements: If the number of wires in the top loading is large, the current distribution will probably be very near quadratic as was assumed by Wait in his investigation of a disk-loaded antenna. On the other hand, if the

[1] J. R. Wait, Earth currents near a monopole antenna with symmetrical top loading, J. Research NBS **62**, (1959) RP2959.

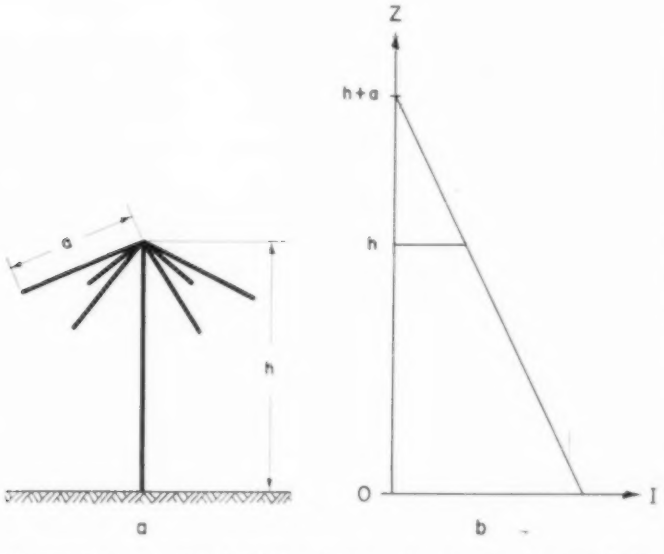

FIGURE 1. a, *Top-loaded antenna.* b, *Assumed current distribution on this antenna.*

number of top-loading wires is small, say one or two, as we shall assume here, the current distribution will probably be linear, to a good approximation. This is shown in figure 1b, where h denotes the length of the vertical wire, a, the length of the radial wires, (these being assumed to be of equal length), and I, the antenna current. A part of the following theory has been derived for an arbitrary current distribution on the antenna. However, in those parts of the investigation where a specific choice of the current distribution has been made, as e.g., in the numerical calculations, the linear current distribution has been chosen.

List of Principal Symbols

a = length of radial wires in top loading,

$\overline{A}$ = vector potential of current on inclined wire,

A_m = coefficient in power series expansion for current distribution function $g(\sigma)$,

b = height over ground plane of one end of inclined wire,

$B = -\frac{\rho}{c}\sin\alpha\cos(\phi-\beta)-\frac{b}{c}\cos\alpha$,

c = length of inclined wire,

$C = \left(\frac{\rho}{c}\right)^2+\left(\frac{b}{c}\right)^2$,

d = reference distance (arbitrary),

$f(s)$ = current distribution function for inclined wire in terms of s,

$g(\sigma)$ = current distribution function for inclined wire in terms of σ,

h = length of vertical member of antenna,

$I(s)$ = current on inclined wire,

I_o = reference current (arbitrary),

I' = current in one top-loading wire at connection point with vertical wire,

I_b = current in vertical member at ground,

I_t = current in vertical member at connection point with top loading,

$\overline{j}$ = normalized surface current density on ground plane: $\frac{d}{I_o}\overline{K}$,

$\overline{j}^h$ = normalized surface current density on ground plane excited by one horizontal wire,

$\overline{j}^H$ = normalized surface current density on ground plane excited by horizontal members of T-antenna,

$\overline{j}^+$ = normalized surface current density on ground plane excited by horizontal members of antenna with four top-loading wires,

$\overline{j}^v$ = normalized surface current density on ground plane excited by vertical member of antenna with top loading,

J = the integral $\int_0^c \frac{f(s)e^{ikr}}{r}ds$,

$\overline{K}$ = surface current density on ground plane,

n = number of wires in top loading,

$N = C-B^2$,

p = moment of Hertz dipole,

p_m = the integral $\int_0^1\left[\left(\frac{c}{R}\right)^3-ikc\left(\frac{c}{R}\right)^2\right]\sigma^m d\sigma$,

P = the integral $\int_0^1\left[\left(\frac{c}{R}\right)^3-ikc\left(\frac{c}{R}\right)^2\right]g(\sigma)e^{ikR}d\sigma$,

r = distance from point of antenna (ξ, η, ζ) to field point (ρ, ϕ, z),

R = distance from point of antenna (ξ, η, ζ) to point of ground plane $(\rho, \phi, 0)$,

s = coordinate along inclined wire,

$\hat{s}$ = unit vector pointing in positive direction of inclined wire,

$\hat{s}_1$, $\hat{s}_2$ = unit vectors pointing in the two directions of horizontal members of T-antenna,

S = point of penetration of inclined wire through ground plane,

$\hat{x}$ etc. = unit vector in x-direction etc.,

$X = \left(\frac{R}{c}\right)^2$,

$X_1 = C+2B+1$,

α = angle between downward vertical direction (negative z-axis) and positive direction $(\hat{s})$ of inclined wire,

β = azimuth of inclined wire,

v = any one of the coordinates ρ, ϕ or z,

ρ, ϕ, z = cylindrical coordinates of field point,

σ = normalized coordinate s/c along inclined wire,

ξ, η, ζ = rectangular coordinates of point of inclined wire.

2. Earth Currents Excited by Inclined Wire

In this section the earth current excited by the current in an inclined straight wire will be calculated, with special reference to the case where the length of the wire, as well as its height over the ground plane, is small compared to the wavelength.

The ground plane is taken as the (x, y) plane in an (x, y, z) coordinate system. A wire of the length c with one of its ends situated on the z-axis at the height b over the (x, y) plane forms the angle α with this axis as shown in figure 2. A coordinate s along the wire is introduced, $s=0$ corresponding to the point of the z-axis. The wire is assumed to carry a current $I(s)=I_o f(s)$ where I_o is an arbitrarily chosen reference current. In this section no particular choice of I_o is made.

The normalized coordinate $\sigma=s/c$ and the function $g(\sigma)=g(s/c)=f(s)$ are introduced. The antenna may be described in parametric form in the rectangular coordinate system (x, y, z) as follows:

$$\xi = s\sin\alpha\cos\beta,$$
$$\eta = s\sin\alpha\sin\beta, \qquad 0\leqq s\leqq c.$$
$$\zeta = b-s\cos\alpha, \qquad (1)$$

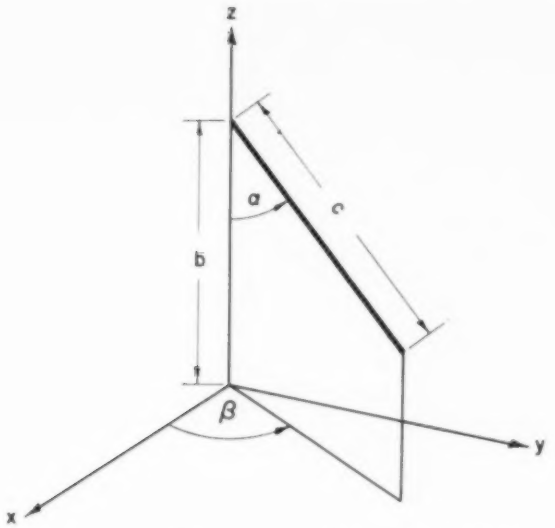

FIGURE 2. *Inclined wire above ground plane.*

With the time factor $e^{-i\omega t}$ the rectangular coordinates of the vector potential $\overline{A}$ are expressed by

$$A_x=\frac{\mu I_o}{4\pi}\sin\alpha\cos\beta\,J,$$

$$A_y=\frac{\mu I_o}{4\pi}\sin\alpha\sin\beta\,J,$$

$$A_z=-\frac{\mu I_o}{4\pi}\cos\alpha\,J, \tag{2}$$

where

$$J=\int_0^c\frac{f(s)\,e^{ikr}}{r}\,ds \tag{3}$$

with

$$r=[(s\sin\alpha\cos\beta-\rho\cos\phi)^2+(s\sin\alpha\sin\beta-\rho\sin\phi)^2+(b-s\cos\alpha-z)^2]^{1/2}, \tag{4}$$

where $(\rho,\ \phi,\ z)$ denote the cylindrical coordinates of the field point. The coordinates of the vector potential $\overline{A}$ in the cylindrical coordinate system are

$$A_\rho=A_x\cos\phi+A_y\sin\phi=\frac{\mu I_o}{4\pi}\sin\alpha\cos(\phi-\beta)\,J,$$

$$A_\phi=-A_x\sin\phi+A_y\cos\phi=-\frac{\mu I_o}{4\pi}\sin\alpha\sin(\phi-\beta)\,J,$$

$$A_z=-\frac{\mu I_o}{4\pi}\cos\alpha\,J. \tag{5}$$

The magnetic field intensity $\overline{H}$ may now be obtained from

$$\overline{H}=\frac{1}{\mu}\nabla\times\overline{A}.$$

Until now, the effect of the ground plane has not been considered. Assuming this to have infinite conductivity, this may be done by adding the field of the image. Since we are interested only in the tangential magnetic field at the ground plane, this is twice the tangential component of the magnetic field calculated above.

For the current density $\overline{K}$ in the ground plane, then,

$$\overline{K}=2(\hat{z}\times\overline{H})_{z=0}. \tag{6}$$

It is convenient to define a dimensionless, normalized surface current density

$$\bar{j}=\frac{d}{I_o}\overline{K}. \tag{7}$$

where d is an arbitrarily chosen reference distance. With the above definition of $\bar{j}$ it is found that

$$j_\rho=-\frac{2d}{I_o}(H_\phi)_{z=0},$$

$$j_\phi=\frac{2d}{I_o}(H_\rho)_{z=0}. \tag{8}$$

Defining

$$P=\int_0^1\left[\left(\frac{c}{R}\right)^3-ikc\left(\frac{c}{R}\right)^2\right]g(\sigma)e^{ikR}d\sigma, \tag{9}$$

with

$$R=(r)_{z=0}=[(s\sin\alpha\cos\beta-\rho\cos\phi)^2+(s\sin\alpha\sin\beta-\rho\sin\phi)^2+(s\cos\alpha-b)^2]^{1/2}$$

$$=c\left[\left(\sigma\sin\alpha\cos\beta-\frac{\rho}{c}\cos\phi\right)^2+\left(\sigma\sin\alpha\sin\beta-\frac{\rho}{c}\sin\phi\right)^2+\left(\sigma\cos\alpha-\frac{b}{s}\right)^2\right]^{1/2}, \tag{10}$$

we finally obtain after some manipulation

$$j_\rho=\frac{1}{2\pi}\frac{d}{c}\left[-\frac{b}{c}\sin\alpha\cos(\phi-\beta)+\frac{\rho}{c}\cos\alpha\right]P, \tag{11a}$$

$$j_\phi=\frac{1}{2\pi}\frac{d}{c}\frac{b}{c}\sin\alpha\sin(\phi-\beta)\,P. \tag{11b}$$

The first term in the square bracket in the expression for P corresponds to the induction field, whereas the last term corresponds to the radiation field.

It is easily verified, from the above expressions for the components of $\bar{j}$ as well as by physical considerations, that j_ρ is an even function of $\phi-\beta$, whereas j_ϕ is an odd function of $\phi-\beta$.

As a partial check of the formulas developed here, these formulas may be applied to a short vertical wire with a constant current I_o as considered by

Wait (see footnote 1). This may be done, for example, by setting

$$b=0,$$

$$\alpha=\pi,$$

$$g(\sigma)=1,$$

$$e^{ikR}\simeq e^{ik\rho}. \tag{12}$$

Then

$$K_\rho=\frac{I_o}{d}j_\rho=\frac{I_o}{2\pi}\frac{\rho}{c^2}\cos\alpha, P=-\frac{I_o e^{ik\rho}\rho}{2\pi}\int_0^a\left[\frac{1}{R^3}-\frac{ik}{R^2}\right]ds \tag{13}$$

$$K_\phi=0,$$

where

$$R=[\rho^2+s^2]^{1/2}.$$

This expression checks with formula (7) in the above mentioned paper by Wait (except for the sign; a different sign convention seems to have been used by Wait).

Whereas it is necessary to evaluate the integral P in order to obtain the normalized surface current density $\bar{j}$, the direction of $\bar{j}$ may be obtained without carrying out any integration. The reason for this is that all the current elements of the wire give contributions to $\bar{j}$ pointing in the same direction. The direction of the current is expressed by the angle u which it forms with the ρ-axis, as shown in figure 3.

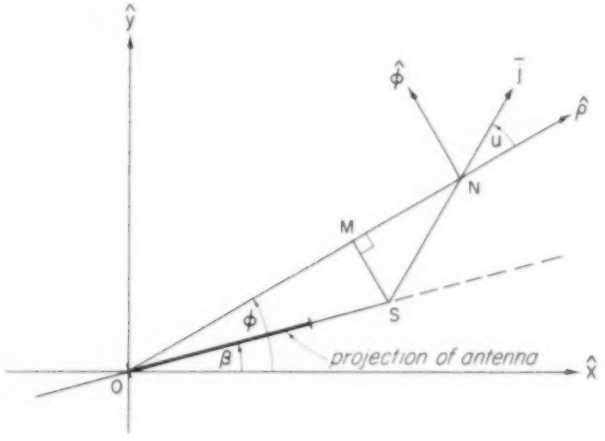

FIGURE 3. *Surface current density.*

The surface current density j points radially outward from (or toward) the point of pentration S through the ground plane of the antenna or its prolongation.

It is found that

$$u=\tan^{-1}\frac{j_\phi}{j_\rho}=\tan^{-1}\frac{b\sin\alpha\sin(\phi-\beta)}{-b\sin\alpha\cos(\phi-\beta)+\rho\cos\alpha}. \tag{14}$$

It will be shown that this expression exactly expresses that the surface current density $\bar{j}$ at every point of the ground plane points radially outward from (or toward) the point S in which the inclined wire or its prolongation penetrates the ground plane. Referring again to figure 3, it is found that the distance from the origin O to the point S is $b\tan\alpha$. Introducing the perpendicular SM from S to the line from the origin O to the field point N, if the current at N points radially outward from S, it follows that

$$u=\tan^{-1}\frac{\mathrm{SM}}{\mathrm{NM}}=\tan^{-1}\frac{b\tan\alpha\sin(\phi-\beta)}{\rho-b\tan\alpha\cos(\phi-\beta)}. \tag{15}$$

As this expression is equal to the expression for u derived above, it is concluded that the surface current density points radially outward from (or toward) the point where the linear antenna or its prolongation penetrates the ground plane. This result, which was arrived at as a detail in a more comprehensive investigation, may of course be derived in a more straightforward manner. In figure 4a is shown an antenna that penetrates the ground plane at S, and lines that are everywhere parallel to the surface current density. They are not field lines in a strict sense, as their mutual distance is not proportional to the magnitude of the surface current density. In the case where the antenna is parallel to the ground plane, i.e., where the point of penetration is at infinity, the surface current density will be everywhere parallel to the wire. This is illustrated in figure 4b.

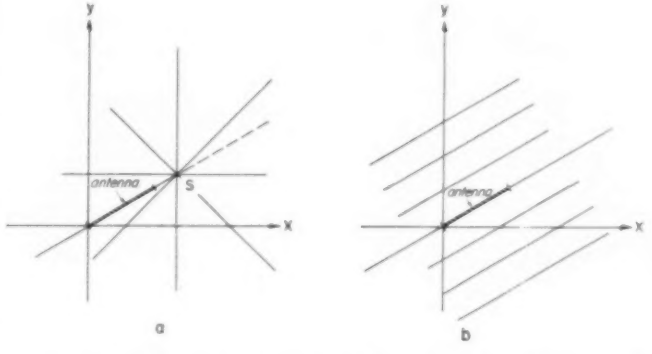

FIGURE 4. *Lines showing direction of the surface current density on the ground plane due to a linear antenna.*

a, The antenna is not parallel to the ground plane; S denotes the point of penetration of the antenna through the ground plane. b, The antenna is parallel to the ground plane, i.e., the point of penetration is at infinity.

Returning to the calculation of the magnitude of the surface current density, the expression P must be evaluated. In the general case the integral by which P is defined can apparently not be expressed by known functions. In the general case, therefore, numerical or graphical methods must be applied to evaluate P. This can be done in any specified case without a prohibitive amount of labor.

A case which has a great practical importance and in which the analysis is greatly simplified is the one where both the height b and the length c of the antenna are small compared to the wavelength or more exactly where

$$k(b+c)<<1.$$

A similar approximation was used by Wait (see footnote 1) in the case of a vertical antenna. For an inclined wire, as is considered here, this approximation will, for the directions perpendicular to the wire, be just as good as for the vertical wire. However, in the directions of the projection of the wire on the ground plane, the approximation will be worse than in the above mentioned case. Or otherwise expressed, for the directions not perpendicular to the wire, kc must be smaller than for a vertical wire in order that we shall obtain the same approximation.

The rest of this report will be concerned exclusively with this case. Under the above assumption, any case will be included in at least one of the following four situations:

1. $k\rho \ll 1$,
2. Neither $k\rho \ll 1$ nor $b+c \ll \rho$,
3. $b+c \ll \rho$ but not $1 \ll k\rho$,
4. $1 \ll k\rho$.

When $k(b+c)$ is not much smaller than 1, say $k(b+c)=0.2$, situation 2 may apply for some values of ρ. On the other hand, if $k(b+c) \lll 1$, situations 1 and 3 may apply simultaneously for some values of ρ. The above discussion is illustrated in figures 5a and 5b applying respectively to the situation where $k(b+c)$ is relatively large (although conforming to the inequality $k(b+c) \ll 1$) and to the situation where $k(b+c)$ is extremely small, $k(b+c) \lll 1$.

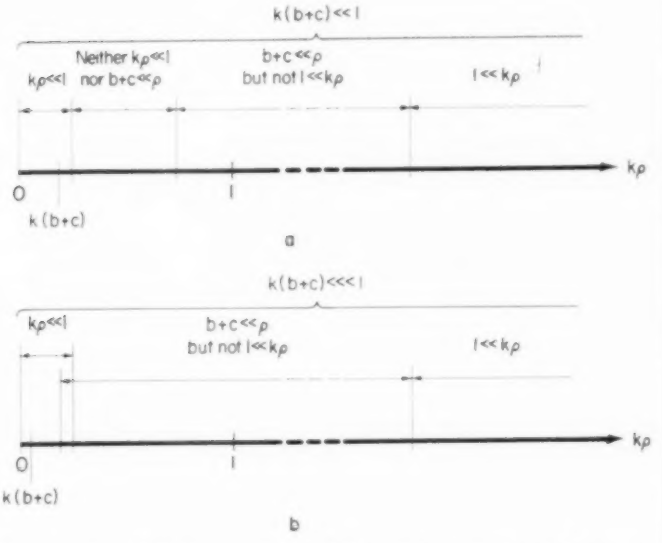

FIGURE 5. *Relative position of the various regions of parameters in which various approximations to the integral* P *apply.*

a, $k(b+c) \ll 1$, but not extremely small; b, $k(b+c) \lll 1$.

$k\rho \ll 1$

$$P \cong \int_0^1 \left(\frac{c}{R}\right)^3 [1-ikR]\left[1+ikR+\frac{(ikR)^2}{2}\right] g(\sigma)d\sigma$$

$$\cong \int_0^1 \left(\frac{c}{R}\right)^3 \left[1+\frac{(kR)^2}{2}\right] g(\sigma)d\sigma \cong \int_0^1 \left(\frac{c}{R}\right)^3 g(\sigma)d\sigma$$

$$+\text{terms containing } (ka)^2,\ (kh)^2,\ (k\rho)^2, \text{ etc.} \quad (16)$$

In using the last approximation the radiation field term, as well as the retardation, is neglected.

Neither $k\rho \ll 1$ nor $b+c \ll \rho$

It turns out that the last one of the approximate formulas worked out for the case of $k\rho \ll 1$ is a special case of the approximate formula in the case of $b+c \ll \rho$. Probably, the last formula may therefore be applied with a fair approximation in the present case, too.

$b+c \ll \rho$ but not $1 \ll k\rho$

$$R=\rho\left[1-2\frac{s}{\rho}\sin\alpha\cos(\phi-\beta)+\left(\frac{s}{\rho}\right)^2-2\frac{s}{\rho}\frac{b}{\rho}\cos\alpha\right.$$

$$\left.+\left(\frac{b}{\rho}\right)^2\right]^{\frac{1}{2}} \cong \rho - s\sin\alpha\cos(\phi-\beta)$$

$$+\text{terms containing } \rho\left(\frac{s}{\rho}\right)^2,\ \rho\frac{s}{\rho}\frac{b}{\rho},\ \rho\left(\frac{b}{\rho}\right)^2 \text{ etc.} \quad (17)$$

$$P \cong e^{ik\rho}\int_0^1 \left(\frac{c}{R}\right)^3 [1-ikR][1-ikc\sigma\sin\alpha\cos(\phi-\beta)]g(\sigma)d\sigma$$

$$+\text{terms containing } kc\left(\frac{c}{\rho}\right)^4,\ kc\frac{b}{\rho}\left(\frac{c}{\rho}\right)^3 \text{ etc.} \quad (18)$$

Though this integral may be expressed by known functions for some current distribution functions $g(\sigma)$, those functions which will be used later in this report will, except in the case of $g(\sigma)=$ constant, require rather complicated computations. As $kc \ll 1$ has been assumed, the term in the last bracket, containing kc, may be neglected with a fair approximation. Thus,

$$P \cong e^{ik\rho}\int_0^1 \left[\left(\frac{c}{R}\right)^3 - ikc\left(\frac{c}{R}\right)^2\right] g(\sigma)d\sigma$$

$$+\text{terms containing } kc\left(\frac{c}{\rho}\right)^3 \text{ etc.} \quad (19)$$

When using this approximation, the retardation along the antenna is neglected (but not from the antenna to the field point).

$1 << k\rho$

Here,

$$kR >> 1,$$

from which

$$P \simeq -e^{ik\rho} ike \int_0^1 \left(\frac{c}{R}\right)^2 [1 - ikc\sigma \sin\alpha \cos(\phi - \beta)] g(\sigma) d\sigma$$

$$+ \text{terms containing } (kR)^{-1} \text{ etc.} \quad (20)$$

Using this approximation means to neglect the induction field term. Also in this case it will generally involve too cumbersome calculations to include the second term in the square bracket; as in the case considered above, with a fair approximation this term may be omitted. This means neglecting the retardation along the antenna itself. Then,

$$P \simeq -e^{ik\rho} ike \int_0^1 \left(\frac{c}{R}\right)^2 g(\sigma) d\sigma. \quad (21)$$

In what follows, eq (16), (19), and (21) will be used as working formulas. The first and the third formulas are both special cases of the second formula. Therefore, the following work will be based upon formula (19), and specializations to the two other cases will be made only at the end of this section.

As was done by Wait (see footnote 1) in treating a disk-loaded monopole, it may profitably be assumed here that the distribution function $g(\sigma)$ of the antenna current is expressed by the series

$$g(\sigma) = \sum_{m=0}^{\infty} A_m \sigma^m.$$

Inserting the above series expression for the current distribution function $g(\sigma)$ in the integral expressing P,

$$P = e^{ik\rho} \sum_{m=0}^{\infty} A_m p_m,$$

where

$$p_m = \int_0^1 \left[\left(\frac{c}{R}\right)^3 - ikc\left(\frac{c}{R}\right)^2\right] \sigma^m d\sigma. \quad (22)$$

This integral may be expressed by known functions for any integral value of m. The coefficients p_m necessary for dealing with a linear current distribution, i.e., p_0 and p_1, will be evaluated here.

In order to carry out the integrations, $X = (R/C)^2$ is put into the standard form,

$$X = C + 2B\sigma + \sigma^2,$$

where

$$B = -\frac{\rho}{c} \sin\alpha \cos(\phi - \beta) - \frac{b}{c} \cos\alpha,$$

$$C = \left(\frac{\rho}{c}\right)^2 + \left(\frac{b}{c}\right)^2.$$

In carrying out the integrations it is important to know the sign of $N = C - B^2$. It is found that

$$N = \left(\frac{\rho}{c}\right)^2 + \left(\frac{b}{c}\right)^2 - \left(\gamma\frac{\rho}{c} + \delta\frac{b}{c}\right)^2,$$

where

$$\gamma = \sin\alpha \cos(\phi - \beta),$$

$$\delta = \cos\alpha.$$

As

$$\gamma^2 + \delta^2 \leqq 1,$$

it may easily be verified that

$$N \geqq 0.$$

Further defining

$$X_1 = (X)_{\sigma=1} = C + 2B + 1,$$

the following is obtained:

$$p_0 = \frac{1}{N}\left[\frac{B+1}{\sqrt{X_1}} - \frac{B}{\sqrt{C}}\right] - \frac{ikc}{\sqrt{N}}\left[\tan^{-1}\frac{B+1}{\sqrt{N}} - \tan^{-1}\frac{B}{\sqrt{N}}\right], \quad (23)$$

$$p_1 = \frac{1}{N}\left[-\frac{B+C}{\sqrt{X_1}} + \sqrt{C}\right] - ikc\left[\frac{1}{2}\ln\frac{X_1}{C} - \frac{B}{\sqrt{N}}\left(\tan^{-1}\frac{B+1}{\sqrt{N}} - \tan^{-1}\frac{B}{\sqrt{N}}\right)\right]. \quad (24)$$

These expressions are sufficient for calculating the contributions to the surface current density corresponding to the terms containing σ^0 and σ^1 in the series expression for the current distribution $g(\sigma)$ of the wire. The terms p_2, p_3, etc. corresponding to the higher order terms in the series expression for $g(\sigma)$ may be found for example by using partial integration, but the calculation is tedious. In the following sections there is a use only for the terms p_0 and p_1, corresponding to a linear current distribution. The calculation of p_1, p_2, etc., is therefore omitted.

Following the discussion given earlier, simplified expressions will be given here for p_0 and p_1 applying when p is respectively very small and very large compared to the wavelength.

$k\rho << 1$

$$p_0 = \frac{1}{N}\left[\frac{1+B}{\sqrt{X_1}} - \frac{B}{\sqrt{C}}\right] \quad (25a)$$

$$p_1 = \frac{1}{N}\left[-\frac{B+C}{\sqrt{X_1}} + \sqrt{C}\right] \quad (25b)$$

$1 << k\rho$

$$p_0 = -ikc\left(\frac{\rho}{c}\right)^{-2} \quad (26a)$$

$$p_1 = -\frac{ikc}{2}\left(\frac{\rho}{c}\right)^{-2}. \quad (26b)$$

3. Vertical Wire

The main purpose of this paper is to calculate the earth current excited by a top loading consisting of one or more inclined or, as a special case, horizontal wires. However, a comparison of the contribution to the earth current from the top loading with the contribution from the vertical member of the antenna is desired. The formulas for calculating this contribution may be obtained as a special case of the formulas developed above.

Considering an antenna of the height h and with a few top-loading wires of the length a, and assuming therefore a linear current distribution, the current I in the vertical member of the antenna may be expressed by

$$I=I_b\left(1-\frac{s}{a+h}\right),$$

where I_b is the current at the bottom of the vertical wire, and where $s=z$. In this section and the following sections I_b will be used as the reference current I_o and the height h of the antenna as the reference distance d occurring in the above formulas. In using these formulas on the vertical member it is further set that

$$b=0,$$

$$c=h,$$

$$\alpha=\pi.$$

The distribution function $g(\sigma)$ for the current on the vertical wire is then expressed by

$$g(\sigma)=1-\frac{h}{a+h}\sigma.$$

The following expression for the normalized earth current $\bar{j}^e$ due to the vertical wire is hereby obtained:

$$j_\rho^e=-\frac{1}{2\pi}\frac{\rho}{h}P,$$

$$j_\phi^e=0,$$

where

$$P=(A_0p_0+A_1p_1)e^{ik\rho}$$

with

$$A_0=1,$$

$$A_1=-\frac{1}{1+\frac{a}{h}}, \tag{27a}$$

$$p_0=\frac{1}{\left(\frac{\rho}{h}\right)^2\sqrt{1+\left(\frac{\rho}{h}\right)^2}}-\frac{ikh}{\frac{\rho}{h}}\tan^{-1}\frac{1}{\frac{\rho}{h}}, \tag{27b}$$

$$p_1=-\frac{1}{\sqrt{1+\left(\frac{\rho}{h}\right)^2}}+\frac{1}{\frac{\rho}{h}}-\frac{ikh}{2}\ln\frac{1+\left(\frac{\rho}{h}\right)^2}{\left(\frac{\rho}{h}\right)^2}. \tag{27c}$$

As the main purpose of this report is to investigate the ground current induced by the top loading, whereas the ground current induced by the vertical member is only calculated for comparison, it may be assumed, for the sake of simplicity, that the vertical wire carries a constant current I_1 equal to the mean value of the actual current distribution, i.e.,

$$I_1=I_b\left[1-\frac{1}{2\left(1+\frac{a}{h}\right)}\right]. \tag{28}$$

We then have

$$P=A_0p_0,$$

where

$$A_0=1-\frac{1}{2\left(1+\frac{a}{h}\right)},$$

and where p_0 is expressed as above. The final expressions for the components of $\bar{j}^e$ then become

$$j_\rho^e=-\frac{e^{ik\rho}}{2\pi}\left[\frac{1}{\frac{\rho}{h}\sqrt{1+\left(\frac{\rho}{h}\right)^2}}-ikh\tan^{-1}\frac{1}{\frac{\rho}{h}}\right]\left[1-\frac{1}{2\left(1+\frac{a}{h}\right)}\right],$$

$$j_\phi^e=0. \tag{29}$$

These expressions are equivalent to formula (7) in the paper by Wait (see footnote 1) referred to above.

In figure 6 $|j_\rho^e|$ has been plotted for $kh=0$ as a function of ρ/h and with a/h as a parameter. In this case, the last term in the first square bracket in the formula expressing j_ρ^e drops out. In the case of very large distances ρ, however, this last term may become significant and even dominant. Figure 7 shows a similar plot of $|j_\rho^e|$ for $kh=0.1$. This value of kh corresponds approximately to the antenna for the planned U.S. Navy vlf radio station, Cutler, Maine (approximate data: $f\simeq 15$ kc, $h\simeq 800$ ft).

4. Top Loading

The ground current excited by an umbrella type of top loading may be calculated by adding vectorially the currents excited by the single wires. In this section an expression is given for the surface current density $\bar{j}$ induced by a single wire of the top loading. Letting $\sigma=0$ correspond to that end of the wire under consideration which is connected to the vertical member of the antenna and $\sigma=1$ to the outer end of the wire, the fact that the current at the end of the antenna is zero is expressed by

$$g(1)=0.$$

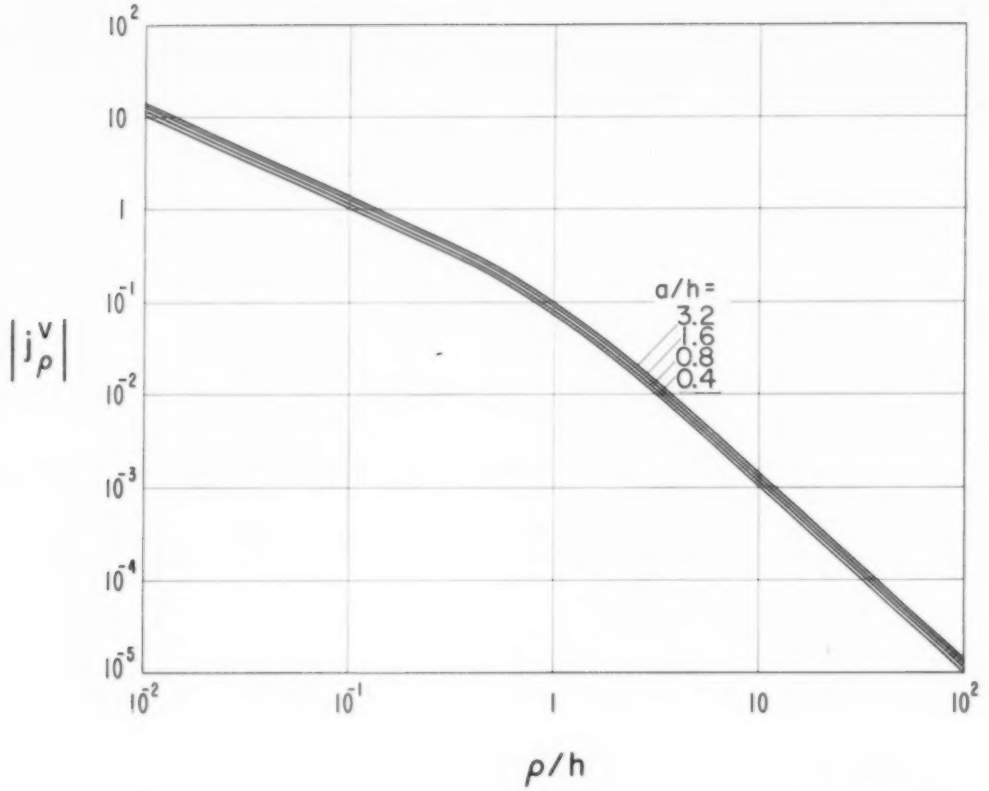

FIGURE 6. *Normalized surface current density* $|j^v_\rho|$ *at the ground plane due to the current in the vertical member of a top-loaded antenna as a function of the normalized distance* ρ/h *from the base of the antenna and with the normalized length* a/h *of the top-loading wires as a parameter.*

It is assumed that the height h of the antenna is infinitely small compared to the wavelength, i.e., $kh=0$.

Using the series expression introduced above for the current in the antenna, it is found that

$$\sum_{m=0}^{\infty} A_m = 0.$$

The current at $\sigma=0$ is denoted by I'. As in the last section, the current I_b at the bottom of the vertical wire will be used as the references current, I_o. Thus,

$$g(0)=\frac{I'}{I_b}.$$

In what follows, it will be assumed that the top loading consists of n equiangularly spaced wires. Each wire will then carry the same current and consequently,

$$g(0)=\frac{1}{n}\frac{I_t}{I_b},$$

where I_t is the current at the top of the vertical wire. Using the series expansion for $g(\sigma)$,

$$A_0=\frac{1}{n}\frac{I_t}{I_b}.$$

In the case of a top loading consisting of one wire (if the wire is horizontal, an L-antenna), or of two wires (if the wires are horizontal, a T-antenna), the current on these wires will probably, to a good approximation, be linear. Then,

$$A_0=-A_1=\frac{1}{n}\frac{\frac{a}{h}}{1+\frac{a}{h}}$$

and all other coefficients A_m equal to zero.

On the other hand, if the top loading is of the umbrella type, i.e., if it consists of several equiangularly spaced wires, the current on the wires will probably be better approximated by a quadratic function. In this case,

$$A_0=-A_2=\frac{1}{n}\frac{\frac{a}{h}}{1+\frac{a}{h}}$$

and all other coefficients A_m equal to zero. The remaining part of this report will be concerned mainly with the cases of a top loading consisting of

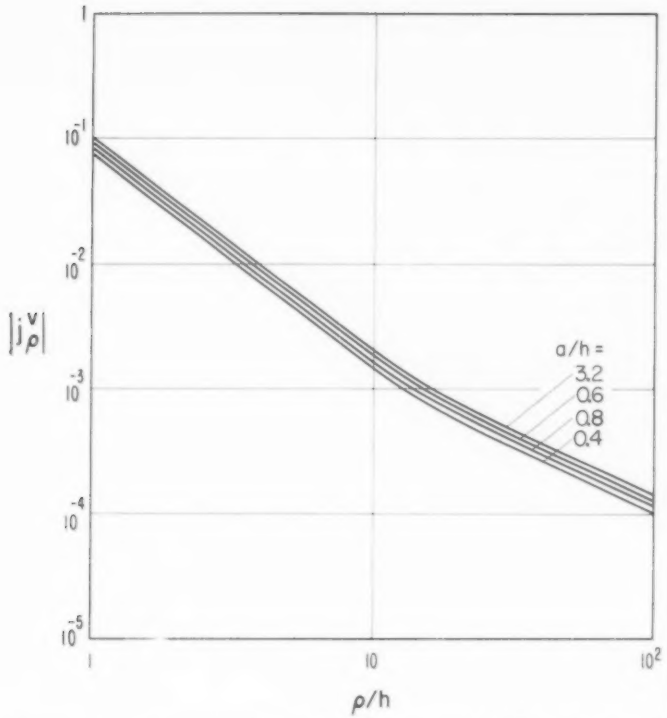

FIGURE 7. *Normalized surface current density $|j^v_\rho|$ at the ground plane due to the current in the vertical member of a top-loaded antenna as a function of the normalized distance ρ/h from the base of the antenna and with the normalized length a/h of the top-loading wires as a parameter, the height* h *of the antenna being given by* kh=0.1.

one ($n=1$) or two ($n=2$) wires and the current distribution will consequently be assumed to be linear.

As in the last section, h will be used as the reference distance d in calculating the normalized surface current density. Further setting

$$b=h$$

$$c=a$$

the following is obtained from the formulas developed above

$$j_\rho=\frac{1}{2\pi}\frac{h}{a}\left[-\frac{h}{a}\sin\alpha\cos(\phi-\beta)+\frac{\rho}{a}\cos\alpha\right]P, \quad (30a)$$

$$j_\phi=\frac{1}{2\pi}\left(\frac{h}{a}\right)^2\sin\alpha\sin(\phi-\beta)P, \quad (30b)$$

where

$$P=\frac{1}{n}\frac{\frac{a}{h}}{1+\frac{a}{h}}(p_0-p_1)e^{ik\rho}=\frac{1}{n}\frac{\frac{a}{h}}{1+\frac{a}{h}}\left\{\frac{1}{N}\left[\sqrt{X_1}-\frac{B}{\sqrt{C}}-\sqrt{C}\right]+ikh\frac{a}{h}\left[\frac{1}{2}\ln\frac{X_1}{C}-\frac{B+C}{\sqrt{N}}\left(\tan^{-1}\frac{B+1}{\sqrt{N}}-\tan^{-1}\frac{B}{\sqrt{N}}\right)\right]\right\}e^{ik\rho}, \quad (31)$$

$$B=-\frac{\rho}{a}\sin\alpha\cos(\phi-\beta)-\frac{h}{a}\cos\alpha,$$

$$C=\left(\frac{\rho}{a}\right)^2+\left(\frac{h}{a}\right)^2,$$

$$N=C-B^2,$$

$$X_1=C+2B+1.$$

For numerical calculations, it is of practical importance to have simplified expressions for P valid when ρ is very small and very large compared to the wavelength respectively. Making use of the discussion given earlier, the following is obtained

$k\rho<<1$

$$P=\frac{1}{n}\frac{\frac{a}{h}}{1+\frac{a}{h}}\frac{1}{N}\left[\sqrt{X_1}-\frac{B}{\sqrt{C}}-\sqrt{C}\right], \quad (32)$$

$1<<k\rho$

$$P=\frac{1}{2n}\frac{\frac{a}{h}}{1+\frac{a}{h}}\left[\frac{1}{C^{3/2}}-ika\frac{1}{C}\right]e^{ik\rho}\cong\frac{1}{2n}\frac{\frac{a}{h}}{1+\frac{a}{h}}\left[\left(\frac{a}{\rho}\right)^3-ika\left(\frac{a}{\rho}\right)^2\right]e^{ik\rho}\cong-\frac{1}{2n}\frac{\frac{a}{h}}{1+\frac{a}{h}}ika\left(\frac{a}{\rho}\right)^2e^{ik\rho}. \quad (33)$$

5. Horizontal Top Loading

In practice a horizontal or nearly horizontal top loading is often used. In this section the simplification which may be obtained in the formulas derived in the last section, as applied to the case of one or two wires when these wires are horizontal, will be considered, and a numerical calculation of the surface current will be carried out.

Setting $\alpha=\pi/2$ the following expressions are obtained for the components of the normalized surface current density $\bar{j}^h$ induced by the horizontal wire

$$j^h_\rho=-\frac{1}{2\pi}\left(\frac{h}{a}\right)^2\cos(\phi-\beta)P \quad (34a)$$

$$j^h_\phi=\frac{1}{2\pi}\left(\frac{h}{a}\right)^2\sin(\phi-\beta)P. \quad (34b)$$

From these formulas it is seen, as has also been shown before, that $\bar{j}^h$ is parallel to the horizontal wire. Therefore, $\bar{j}^h=j^h_s\,\hat{s}$ may be set, where $\hat{s}$ is a unit vector pointing in the positive direction of the wire. It is found that

$$j^h_s=-\frac{1}{2\pi}\left(\frac{h}{a}\right)^2P.$$

The factor P is expressed by the quantities B, C, N, and X_1 as in the last section. However, in the present case the expression for B reduces to

$$B=-\frac{\frac{\rho}{h}}{\frac{a}{h}}\cos(\phi-\beta).$$

The quantity $n\,|j_s^h|$ has been plotted in figures 8a and 8b for $kh=0$ and in figures 9a and 9b for $kh=0.1$, and in both cases for $\phi-\beta=0°$ and 180° as a function of ρ/h and with a/h as a parameter. From these curves and from similar curves for other values of $\phi-\beta$, the ρ and the ϕ components of nj^h by multiplying with cos $(\phi-\beta)$ and sin $(\phi-\beta)$, respectively, are obtained.

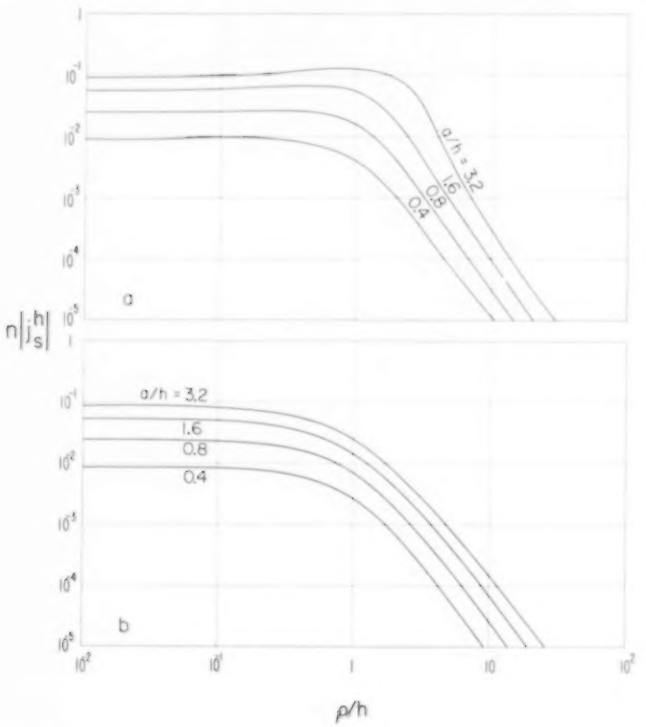

FIGURE 8. *Normalized surface current density* $|j_s^h|$ *at the ground plane due to the current in the horizontal member of an antenna with one horizontal top-loading wire as a function of the normalized distance* ρ/h *from the base of the antenna and with the normalized length* a/h *of the top-loading wire as a parameter.*

It is assumed that the height h of the antenna is infinitely small compared to the wavelength, i.e, $kh=0$. a, $\phi-\beta=0°$; b, $\phi-\beta=180°$.

6. L-Antenna

An L-antenna of the height h and its horizontal member having the length a as shown in figure 10 are considered. As in this case the number n of wires in the top loading is equal to 1, the contribution $\bar{j}^h$ to the normalized surface current density coming from the horizontal top loading may be obtained directly from figures 8 and 9 in the last section.

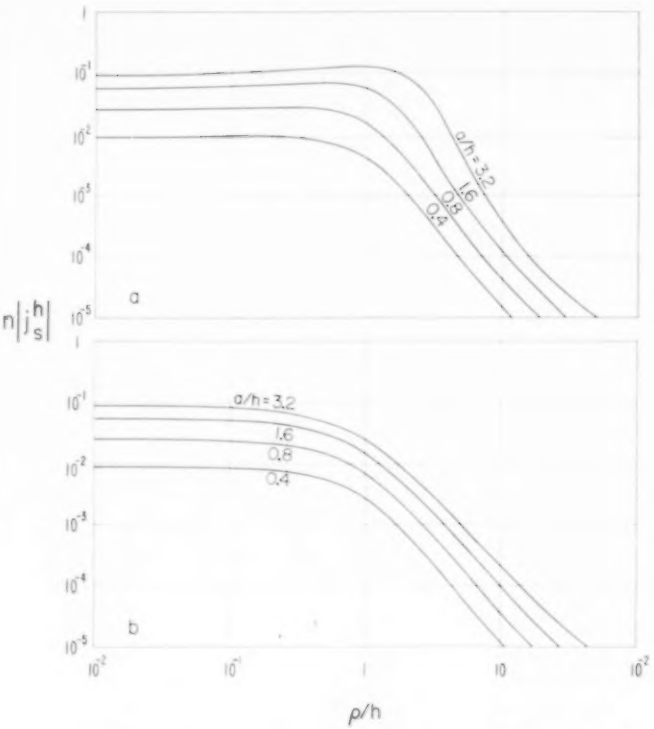

FIGURE 9. *Normalized surface current density* $|j_s^h|$ *at the ground plane due to the current in the horizontal member of an antenna with one horizontal top-loading wire as a function of the normalized distance* ρ/h *from the base of the antenna and with the normalized length* a/h *of the top-loading wire as a parameter, the height* h *of the antenna being given by* $kh=0.1$.

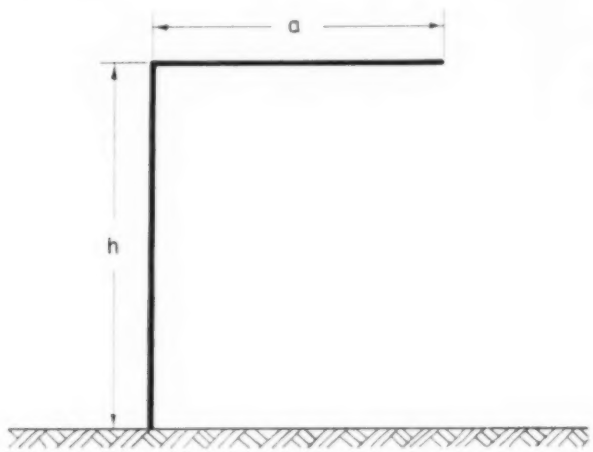

FIGURE 10. *L-antenna.*

The contribution $\bar{j}^h$ obtained from these curves should be compared with the contribution $\bar{j}^v$ originating from the vertical member of the antenna as shown in figures 6 and 7. A comparison of these figures shows that, compared to the radial component j_ρ^v of the normalized surface current density induced by the vertical wire, the radial component j_ρ^h of the normalized surface current density induced by the horizontal wire is small also in the vicinity of the

antenna, and becomes insignificant at large distances. This was the same conclusion that was arrived at by Wait (see footnote 1) in his investigation of a disk-loaded monopole. A similar statement may be made regarding the azimuthal component j_ϕ^h of the normalized surface current density induced by the horizontal wire. However, if the ground wires are placed radially around the antenna, as is usually the case, the ground losses induced by the azimuthal component j_ϕ^h may be significant compared to the losses induced by j_ρ^v, even if j_ϕ^h is considerably smaller than j_ρ^v.

In order to facilitate a comparison of j_ϕ^h with j_ρ^v, the quotient

$$\frac{|j_\phi^h|}{|j_\rho^v|}=\frac{|j_s^h \sin(\phi-\beta)|}{|j_\rho^v|}$$

has been plotted in figures 11a and 11b for $kh=0$ and for $\phi-\beta=45°$ and 135°. In the cases of $\phi-\beta=0°$ and 180°, respectively, the quotient is zero. Curves have not been given for the case of $kh=0.1$ treated earlier, as these curves would deviate only slightly from the curves in the case of $kh=0$ over the significant range of values of ρ/h.

7. T-Antenna

A T-antenna of the height h and with its horizontal member having the length $2a$ as shown in figure 12 is considered. Letting $\beta=\beta_1$ denote the angular position of one of the two horizontal wires of which the top loading consists, we have for the

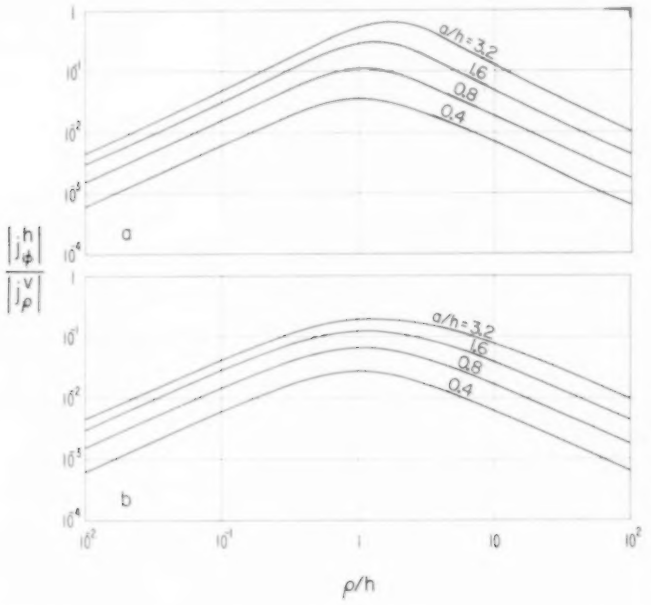

FIGURE 11. *Ratio between the azimuthal component* $|j_\phi^h|$ *of the surface current density due to the current in the horizontal member of an* L*-antenna and the surface current density* $|j_\rho^v|$ *due to the vertical member of the same antenna.*

It is assumed that the height h of the antenna is infinitely small compared to the wavelength, i.e., $kh=0$; a, $\phi-\beta=45°$. b, $\phi-\beta=135°$.

angular position $\beta=\beta_2$ of the other radial wire $\beta_2=\beta_1+\pi$. Utilizing the symmetry properties of the normalized surface current density $\bar{j}^h$ induced by one radial wire it is then found that the following expressions for the normalized surface current density $\bar{j}^H$ of the total top loading by adding the contributions from each of the two wires,

$$\bar{j}^H(\phi-\beta_1)=\bar{j}^h(\phi-\beta_1)+\bar{j}^h(\phi-\beta_2)=\hat{s}_1 j_s^h(\phi-\beta_1)$$
$$+\hat{s}_2 j_s^h(\phi-\beta_1-\pi), \quad (36)$$

where $\hat{s}_1$ and $\hat{s}_2$ denote unit vectors in the positive directions of the two top-loading wires, respectively, as shown in figure 12, and where $j_s^h(u)$ is the function introduced in the section on a general, horizontal top loading. Utilizing

$$\hat{s}_2=-\hat{s}_1$$

and

$$j_s^h(-u)=j_s^h(u),$$

it is found that

$$\bar{j}^H(\phi-\beta_1)=\hat{s}_1 j_{s_1}^H(\phi-\beta_1), \quad (37)$$

where

$$j_{s_1}^H(\phi-\beta_1)=j_s^h(\phi-\beta_1)-j_s^h(\pi-(\phi-\beta_1)). \quad (38)$$

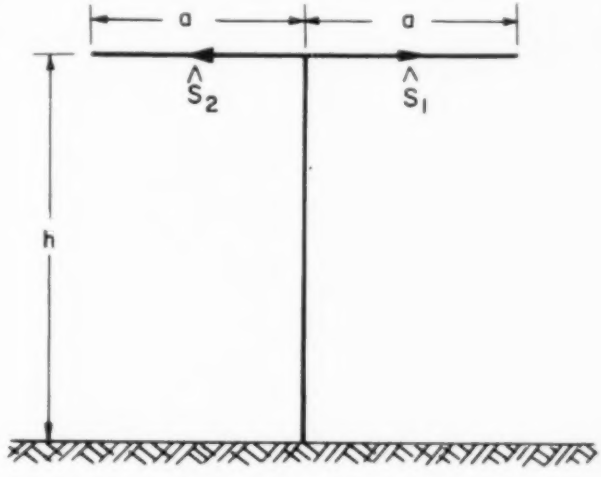

FIGURE 12. T-*antenna.*

As the number of wires in the top loading is equal to 2, the function

$$j_s^h(\phi-\beta_1)$$

may be obtained as one-half the value given by the curves in figure 8 or 9.

It is easily verified that $j_s^h(\phi-\beta)$ satisfies the following symmetry relations,

$$j_{s_1}^H[-(\phi-\beta_1)]=j_{s_1}^H(\phi-\beta_1), \quad (39a)$$

$$j_{s_1}^H[\pi-(\phi-\beta_1)]=j_{s_1}^H(\phi-\beta_1). \quad (39b)$$

It follows from the above expression for $\bar{j}^H$ that

$$\bar{j}^H\left(\pm\frac{\pi}{2}\right)=0.$$

Because of the symmetry relations mentioned above, it is necessary only to calculate the normalized surface current density for $\phi-\beta_1$ being in the interval 0 to $\pi/2$.

The quantity $|\bar{j}^H_{s_1}(\phi-\beta)|$ has been plotted in figure 13 for $kh=0$ and for $\phi-\beta_1=0°$ as a function of ρ/h and with a/h as a parameter. This diagram giving the contributions to the normalized surface current density arising from the horizontal wire should be compared to the contributions from the vertical member shown in figures 6 and 7. This comparison leads to the same qualitative statements regarding the significance of the relative contributions from the horizontal wire as were arrived at in the case of the L-antenna.

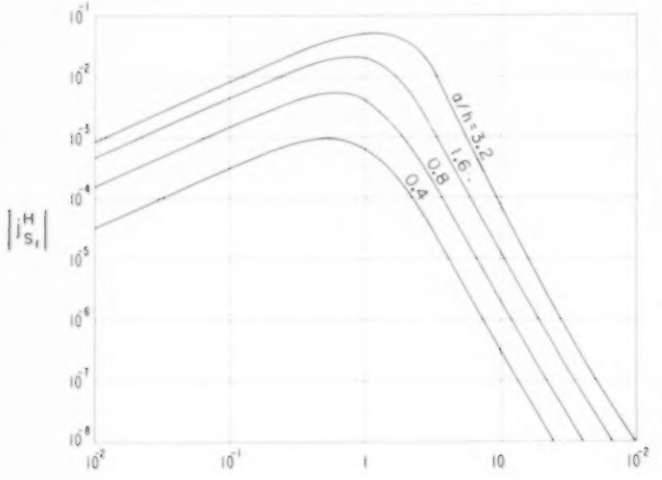

FIGURE 13. *Normalized surface current density $|j^{-H}_{s_1}|$ at the ground plane due to the current in the horizontal members of a T-antenna as a function of the normalized distance ρ/h from the base of the antenna and with the normalized length a/h of the top-loading wires as a parameter.*

It is assumed that the height h of the antenna is infinitely small compared to the wavelength, i.e., $kh=0$, $\phi-\beta=0°$.

In order to be better able to survey the situation, in figure 14 the following quotient is plotted,

$$\left|\frac{j^H_\phi}{j^V_\rho}\right|$$

for $kh=0$ and for $\phi=45°$ as a function of ρ/h and with a/h as a parameter. For $\phi=0°$ and 90° the quotient is zero. Paying attention to this fact and comparing figure 14 with figures 11a and 11b, it can probably be said that in general the azimuthal component of the surface current density induced by the top loading is smaller for a T-antenna with a horizontal wire of the length $2a$ than for an L-antenna of the same height and with a horizontal wire of the length a.

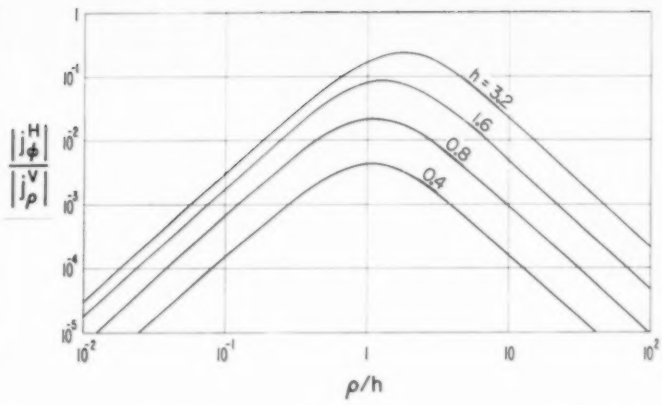

FIGURE 14. *Ratio between the azimuthal component $|j^h_\phi|$ of the surface current density due to the current in the horizontal members of a T-antenna and the surface current density $|j^v_\rho|$ due to the vertical member of the same antenna.*

It is assumed that the height h of the antenna is infinitely small compared to the wavelength, i.e., $kh=0$. $\phi-\beta=45°$.

On the other hand, the radial component will at some points be larger, at some points smaller for the T-antenna than for the corresponding L-antenna. For an antenna with a radial ground wire system it is essential to keep the azimuthal component of the surface current density as small as possible in order to make the total ground losses the smallest possible. In this respect a T-antenna is probably in general preferable to an L-antenna.

8. Antenna with Four Horizontal Top-Loading Wires

The theory developed above for the surface current induced on the ground plane by a straight wire with a linear current distribution will be used also for finding the earth currents induced by a top-loaded antenna with four equiangularly spaced wires in the top loading. Although in the present case the assumption of a linear current distribution, as was mentioned before, probably does not approximate the actual current distribution so well as in the case of an L- or a T-antenna, it is desirable to include the case of an antenna with four horizontal top-loading wires, as this case is very close to the case of a disk-loaded antenna; on the basis of the results obtained in this section it should therefore be possible to make a comparison between the theory developed in this report and the theory developed for a disk-loaded monopole. However, it should be kept in mind that whereas the formulas and numerical results obtained in this report are based on the assumption of a linear current distribution on the top loading, Wait in his investigation of a disk-loaded antenna assumes a quadratic current distribution on the disk.

The length of the vertical member of the antenna is denoted by h and the length of the top-loading wires by a as indicated in figure 15. Further, the azimuth of the top-loading wires is denoted by β_1, β_2, β_3, and β_4, respectively, and the unit vectors

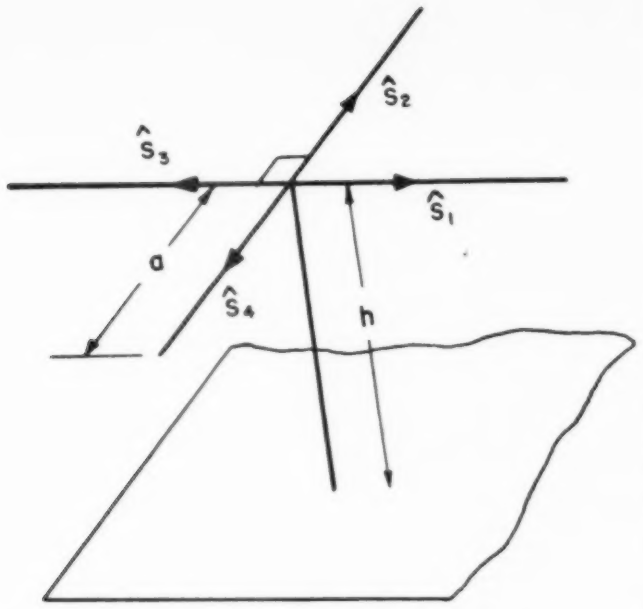

FIGURE 15. *Antenna with four horizontal, top-loading wires.*

pointing in the positive direction of these wires by $\hat{s}_1$, $\hat{s}_2$, $\hat{s}_3$, and $\hat{s}_4$. Then,

$$\beta_2=\beta_1+\frac{\pi}{2},$$

$$\beta_3=\beta_1+\pi,$$

$$\beta_4=\beta_1+\frac{3\pi}{2},$$

and

$$\hat{s}_3=-\hat{s}_1,$$

$$\hat{s}_4=-\hat{s}_2.$$

Making use of the symmetry properties of the normalized surface current density $\bar{j}^h$ induced by one radial wire it is found that the following expressions for the normalized surface current density $\bar{j}^+$ of the total top loading:

$$\begin{aligned}\bar{j}^+(\phi-\beta_1)&=\hat{s}_1 j_s^h(\phi-\beta_1)+\hat{s}_2 j_s^h(\phi-\beta_2)\\&\quad+\hat{s}_3 j_s^h(\phi-\beta_3)+\hat{s}_4 j_s^h(\phi-\beta_4)\\&=\hat{s}_1 j_{s_1}^+(\phi-\beta_1)+\hat{s}_2 j_{s_2}^+(\phi-\beta_1),\end{aligned}\tag{40}$$

where

$$j_{s_1}^+(\phi-\beta_1)=j_s^h(\phi-\beta_1)-j_s^h(\pi-(\phi-\beta_1)),\tag{41a}$$

$$j_{s_2}^+(\phi-\beta_1)=j_s^h\left(\frac{\pi}{2}-(\phi-\beta_1)\right)-j_s^h\left(\phi-\beta_1+\frac{\pi}{2}\right).\tag{41b}$$

It may be verified that $\bar{j}^+(\phi-\beta_1)$ satisfies the following symmetry relations:

$$\bar{j}^+(-(\phi-\beta_1))=\hat{s}_1 j_{s_1}^+(\phi-\beta_1)-\hat{s}_2 j_{s_2}^+(\phi-\beta_1),\tag{42a}$$

$$\bar{j}^+\left(\frac{\pi}{2}-(\phi-\beta_1)\right)=\hat{s}_1 j_{s_2}^+(\phi-\beta_1)+\hat{s}_2 j_{s_1}^+(\phi-\beta_1),\tag{42b}$$

$$\bar{j}^+(\pi-(\phi-\beta_1))=-\hat{s}_1 j_{s_1}^+(\phi-\beta_1)+\hat{s}_2 j_{s_2}^+(\phi-\beta_1).\tag{42c}$$

It follows from the above expression for $\bar{j}^+$ that

$$\bar{j}^+(0)=\hat{s}_1[j_s^h(0)-j_s^h(\pi)]=\hat{\rho}[j_s^h(0)-j_s^h(\pi)],\tag{43a}$$

$$\begin{aligned}\bar{j}^+\left(\frac{\pi}{4}\right)&=(\hat{s}_1+\hat{s}_2)\left[j_s^h\left(\frac{\pi}{4}\right)-j_s^h\left(\frac{3\pi}{4}\right)\right]\\&=\hat{\rho}\sqrt{2}\left[j_s^h\left(\frac{\pi}{4}\right)-j_s^h\left(\frac{3\pi}{4}\right)\right],\end{aligned}\tag{43b}$$

where $\hat{\rho}$ denotes a unit vector pointing in the radial direction. As the number n of wires in the top loading is equal to 4, the function

$$j_s^h(\phi-\beta)$$

may be obtained as one-fourth the value given by the curves in figure 8 or 9.

Because of the above relations the whole current field will be known, if it has been calculated in the angular space

$$0\leqq\phi-\beta_1<\frac{\pi}{4}.$$

Using the symmetry relations stated above it is found that $\bar{j}^+(\phi-\beta_1)$ is purely radial for

$$\phi-\beta_1=p\frac{\pi}{4},$$

where p is an integer. For these angles the radial component

$$j_\rho^+(\phi-\beta_1)$$

is given by

$$j_\rho^+(\phi-\beta_1)=\begin{cases}j_s^h(0)-j_s^h(\pi)\ \text{for}\ \phi-\beta_1=q\dfrac{\pi}{2}\\[2ex]\sqrt{2}\left[j_s^h\left(\dfrac{\pi}{4}\right)-j_s^h\left(\dfrac{3\pi}{4}\right)\right]\ \text{for}\ \phi-\beta_1=\dfrac{\pi}{4}+q\dfrac{\pi}{2}\end{cases}$$

where q is an integer. (44)

The quantity $|j_\rho^+(\phi-\beta_1)|$ has been plotted in figure 16 for $kh\simeq 0$ and for $\phi-\beta_1=0°$ as a function of ρ/h and with a/h as a parameter. These curves should be compared with the curves given in Wait's report

(see footnote 1) on the earth currents induced by the disk in a disk-loaded monopole. It is seen that the currents in figure 16 have the same trend and the same order of magnitude as the curves computed by Wait.

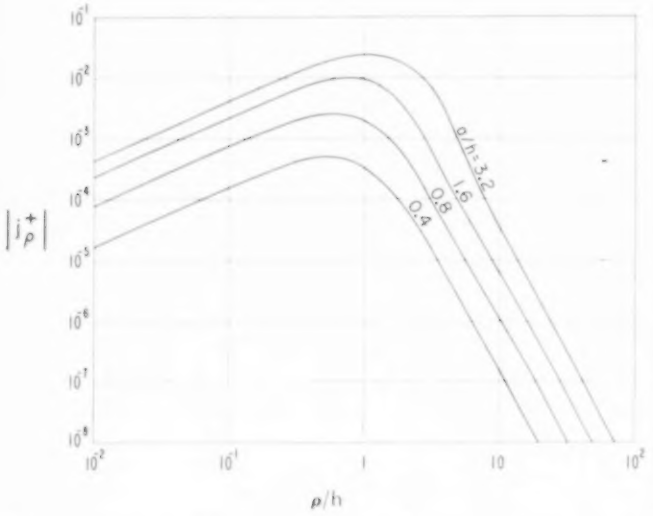

FIGURE 16. *Radial component $|j_\rho^+|$ of normalized surface current density due to the current in the horizontal members of an antenna with four horizontal, top-loading wires as a function of the normalized distance ρ/h from the base of the antenna and with the normalized length a/h of the top-loading wires as a parameter.*

It is assumed that the height h of the antenna is infinitely small compared to the wavelength, i.e., $kh=0$; $\phi-\beta=0°$.

9. Conclusion

Based on a formula for and numerical calculations of the surface current density on a ground plane above which is placed a straight piece of wire with a length that is small compared to the wavelength and with a linear current distribution, the contribution to the ground current of the top loading of L- and T-antennas that are small compared to the wavelength has been found and plotted. Whereas the contribution from the top-loading to the radial component of the surface current density, as was shown earlier by Wait, in general may be neglected, as it is insignificant compared to the contribution from the vertical wire, the azimuthal component of the surface current density produced by the top loading may be important in calculating the ground losses in the case of a system of radial ground wires, as it is perpendicular to these wires. The formulas and numerical results in this report form a basis for calculating the ground losses due to this azimuthal component.

This investigation was carried out while the author was temporarily employed as a consultant at the National Bureau of Standards in Boulder. He thanks the Bureau for the opportunity to do this work. He also thanks James R. Wait for suggesting the problem and Maxine W. Clark for making the numerical calculations.

BOULDER, COLO., January 27, 1959.

INDEX TO VOLUME 62

January to June 1959—Research Papers 2921 to 2963

A

Page

Abramowitz, M., W. F. Cahill, C. Wade Jr., Heat transfer in laminar flow through a tube, RP2937 ... 101
Absolute light-scattering photometer: I. Design and operation, RP2946 ... 153
Absorption spectra, infrared, of some cyclic acetals of sugars, RP2960 ... 259
Acetals, cyclic, of sugars, infrared absorption spectra, RP2960 ... 259
Adsorption of polyesters on glass, silica, and alumina, RP2933 ... 71
Antenna, monopole with symmetrical top loading, earth currents near, RP2959 ... 247
Antenna, top-loaded monopole, earth currents near with special regard to electrically small L- and T-antennas, RP2961 ... 283
Arsenate, silicate, and phosphate, separation and determination, RP2954 ... 201

B

Barium disilicate—dibarium trisilicate, subsystem, phase equilibria, RP2953 ... 193
Bates, R. G., M. Eden, Resolution of the dissociation constants of *d, l*-malic acid from 0° to 50° C, RP2947 ... 161
Bender, B. K., A. J. Goldman, Capacity requirement of a mail sorting device, RP2948 ... 171
Benzenes, tetrafluoro, 1, 2, 2, 4-, preparation of from 2-chloroheptafluorotoluene, RP2939 ... 113
Blaine, L. R., E. K. Plyler, Infrared high-resolution grating spectrometer, RP2922 ... 7
Block, S., G. Burley, A. Perloff, R. D. Mason, Jr., Refinement of the crystal structure of triclinic magnesium pyroborate, RP2936 ... 95
Block-type osmometer, design and performance, RP2931 ... 63
Boric oxide, the heat of formation, heat of reaction of diborane with water, RP2927 ... 43
Boron trichloride, heat of formation, RP2956 ... 213
Burley, G., S. Block, A. Perloff, R. D. Mason, Jr., Refinement of the crystal structure of triclinic magnesium pyroborate, RP2936 ... 95

C

Cahill, W. F., M. Abramowitz, C. Wade, Jr., Heat transfer in laminar flow through a tube, RP2937 ... 101
Capacity requirement of a mail sorting device, RP2948 ... 171
Chi, M., L. K. Irwin, Elastic deformation in strips with holes loaded through pins, RP2945 ... 147
Clabaugh, W. S., A. Jackson, Separation and determination of phosphate, silicate, and arsenate, RP2954 ... 201
Crystal structure of triclinic magnesium pyroborate, refinement, RP2936 ... 95
Currents, earth, near a top-loaded monopole antenna, with special regard to electrically small L- and T-antennas, RP2961 ... 283
Cyclic acetals of sugars, infrared absorption spectra, RP2960 ... 257

D

Deformation, elastic, in strips with holes loaded through pins, RP2945 ... 147
Degradation, thermal, of polymers at low rates, RP2957 ... 219
Design and performance of a block-type osmometer, RP2931 ... 63
Determination of niobium and tantalum in titanium-base alloys, RP2929 ... 53
Determination of titanium, zirconium, niobium, and tantalum in steels: separations by anion-exchange, RP2923 ... 11
Deuterostyrenes, mass spectra of some, RP2926 ... 39
Deviation, standard, and mean absolute value of the phase of a constant vector plus a Rayleigh-distributed vector, RP2950 ... 183
Diborane, heat of reaction of, with water and the heat of formation of boric oxide, RP2927 ... 43
Dissociation constant of *d, l*-malic acid, RP2947 ... 161
Doderer, G. C., D. McIntyre, Absolute light-scattering photometer: I. Design and operation, RP2946 ... 153
—, —, *J. H. O'Mara*, Design and performance of a block-type osmometer, RP2931 ... 63

E

Earth currents near a monopole antenna with symmetrical top loading, RP2959 ... 247
Earth currents near a top-loaded monopole antenna with special regard to electrically small L- and T-antennas, RP2961 ... 283
Earth satellite, theory of the effect of drag on the orbital inclination of, RP2934 ... 79
Eden, M., R. G. Bates, Resolution of the dissociation constants of *d, l*-malic acid from 0° to 50° C, RP2947 ... 161
Effect of internal radiant heat transfer on temperature distribution, thermal stress, and deflection in box beams, RP2949 ... 175
Effect of oxygen on the bonding of gold to fused silica, RP2942 ... 127
Elastic deformation in strips with holes loaded through pins, RP2945 ... 147
Engel, O. G., Pits in metals caused by collision with liquid drops and soft metal spheres, RP2958 ... 229
Exponential integral $\int_1^\infty e^{-xt}t^{-n}dt$ for large values of n, RP2941 ... 123

F

Flatness of large surfaces, testing of by interferometer, RP2943 ... 137
Florin, R. E., W. J. Pummer, L. A. Wall, Fluorination of haloaromatic compounds, RP2938 ... 107
—, —, —, Reactions of aromatic fluorocarbons with hydrogen, RP2940 ... 119
—, —, —, Synthesis of some disubstituted 3,4,5,6- tetrafluorobenzenes, RP2939 ... 113
Fluorination of haloaromatic compounds, RP2938 ... 107
Fluorocarbons, aromatic, reactions with hydrogen, RP2940 ... 119
Formation of titanium tetrachloride, heat, RP2928 ... 49
Frolen, L. J., G. S. Ross, Simple rotating molecular still, RP2951 ... 187

G

Garfinkel, S. B., W. B. Mann, L. L. Stockmann, W. J. Youden, A. Schwebel, P. A. Mullen, Preparation of new solution standards of radium, RP2924 ... 21
Gautschi, W., Exponential integral $\int_1^\infty e^{-xt}t^{-n}dt$ for large values of n, RP2941 ... 123
Glass formation in polymers. II. The system rubber-sulfur, RP2944 ... 141
Glasses, zinc borosilicate, properties, RP2930 ... 59
Gold, the bonding of to fused silica, effect of oxygen, RP2942 ... 127
Goldman, A. J., B. M. Bender, Capacity requirement of a mail sorting device, RP2948 ... 171
Goodman, S., S. B. Russell, C. E. Noble, Effect of internal radiant heat transfer on temperature distribution, thermal stress, and deflection in box beams, RP2949 ... 175
Gross, F. L., J. B. Saunders, Interferometer for large surfaces, RP2943 ... 137

H

Hague, J. L., L. A. Machlan, Determination of niobium and tantalum in titanium-base alloys, RP2929 ... 53
—, —, Determination of titanium, zirconium, niobium, and tantalum in steels: separations by anion-exchange, RP2923 ... 11
Haloaromatic compounds, fluorination, RP2938 ... 107
Hamilton, E. H., R. M. Waxler, J. M. Nivert, Jr., Properties of zinc borosilicate glasses, RP2930 ... 59
Heat of formation of boron trichloride, RP2956 ... 213
Heat of formation of potassium calcium silicate, RP2955 ... 207
Heat of formation of titanium tetrabromide, RP2932 ... 67
Heat of formation of titanium tetrachloride, RP2928 ... 49
Heat of mixing of polybutadiene and benzene, RP2921 ... 1
Heat of reaction of diborane with water and the heat of formation of boric oxide, RP2927 ... 43
Heat transfer in laminar flow through a tube, RP2937 ... 101
Heat transfer, effect of internal radiant, on temperature distribution, thermal stress, and deflection in box beams, RP2949 ... 175
High-resolution grating spectrometer, infrared, RP2922 ... 7

I

Infrared absorption spectra of some cyclic acetals of sugars, RP2960 ... 257
Infrared high-resolution grating spectrometer, RP2922 ... 7
Intercomparing neutron source strengths by means of a manganous sulfate bath, scintillation counter method, RP2952 ... 189
Interferometer for large surfaces, RP2943 ... 137
Irwin, L. K., M. Chi, Elastic deformation in strips with holes loaded through pins, RP2945 ... 147
Isbell, H. S., R. S. Tipson, J. E. Stewart, Ihfrared absorption spectra of some cyclic acetals of sugars, RP2960 ... 257

J

Jackson, A., W. S. Clabaugh, Separation and determination of phosphate, silicate, and arsenate, RP2954 ... 201
Jessup, R. S., Heat of mixing of polybutadiene and benzene, RP2921 ... 1
Johler, J. R., L. C. Walters, Mean absolute value and standard deviation of the phase of a constant vector plus a Rayleigh-distributed vector, RP2950 ... 183
Johnson, W. H., E. J. Prosen, F. Y. Pergiel, Heat of reaction of diborane with water and the heat of formation of boric oxide, RP2927 ... 43
—, *R. A. Nelson, E. J. Prosen*, Heat of formation of titanium tetrachloride, RP2928 ... 49
—, —, —, Heat of formation of titanium tetrabromide, RP2932 ... 67
—, *R. G. Miller, E. J. Prosen*, Heat of formation of boron trichloride, RP2956 ... 213

K

Knudsen, H. L., Earth currents near a top-loaded monopole antenna with special regard to electrically small L- and T-antennas, RP2961 ... 283

L

Laminar flow through a tube, heat transfer, RP2937 ... 101
Large surfaces, testing of by interferometer, RP2943 ... 137
Lead oxide-niobium pentoxide, phase equilibrium relations in the binary system, RP2925 ... 27
Levin, E. M., R. S. Roth, Phase equilibria in the subsystem barium disilicate—dibarium trisilicate, RP2953 ... 193

M

Machlan, L. A., J. L. Hague, Determination of niobium and tantalum in titanium-base alloys, RP2929 ... 53
—, —, Determination of titanium, zirconium, niobium, and tantalum in steels: separations by anion-exchange, RP2923 ... 11
Madorsky, S. L., Thermal degradation of polymers at low rates, RP2957 ... 219
Mail sorting device, capacity requirement, RP2948 ... 171
Malic acid, dissociation constant, RP2947 ... 161
Mandelkern, L., G. M. Martin, Glass formation in polymers. II. The system rubber-sulfur, RP2944 ... 141

Page

Mann, W. B., L. L. Stockmann, W. J. Youden, A. Schwebel, P. A. Mullen, S. B. Garfinkel, Preparation of new solution standards of radium, RP2924 ... 21
Martin, G. M., L. Mandelkern, Glass formation in polymers. II. The system rubber-sulfur, RP2944 ... 141
Mason, R. D., Jr., S. Block, G. Burley, A. Perloff, Refinement of the crystal structure of triclinic magnesium pyroborate, RP2936 ... 95
Mass spectra of some deuterostyrenes, RP2926 ... 39
McIntyre, D., G. C. Doderer, Absolute light-scattering photometer: I. Design and operation, RP2946 ... 153
—, —, *J. H. O'Mara*, Design and performance of a block-type osmometer, RP2931 ... 63
Mean absolute value and standard deviation of the phase of a constant vector plus a Rayleigh-distributed vector, RP2950 ... 183
Metals, pits in, by collision with liquid drops and soft metal spheres, RP2958 ... 229
Miller, R. G., W. H. Johnson, E. J. Prosen, Heat of formation of boron trichloride, RP2956 ... 213
Mohler, F. L., E. I. Quinn, Mass spectra of some deuterostyrenes, RP2926 ... 39
Molecular still, simple rotating, RP2951 ... 187
Monopole antenna with symmetrical top loading, earth currents near, RP2959 ... 247
Moore, D. G., H. R. Thornton, Effect of oxygen on the bonding of gold to fused silica, RP2942 ... 127
Mosburg, E. R., Jr., Scintillation counter method of intercomparing neutron source strengths by means of a manganous sulfate bath, RP2952 ... 189
Mullen, P. A., W. B. Mann, L. L. Stockmann, W. J. Youden, A. Schwebel, S. B. Garfinkel, Preparation of new solution standards of radium, RP2924 ... 21

N

Nelson, R. A., W. H. Johnson, E. J. Prosen, Heat of formation of titanium tetrabromide, RP2932 ... 67
—, —, —, Heat of formation of titanium tetrachloride, RP2928 ... 49
Neutron source strengths, scintillation counter method of intercomparing by means of a manganous sulfate bath, RP2952 ... 189
Newman, E. S., Heat of formation of potassium calcium silicate, RP2955 ... 207
Niobium and tantalum in titanium-base alloys, determination of, RP2929 ... 53
Niobium pentoxide-lead oxide, phase equilibrium relations in the binary system, RP2925 ... 27
Niobium, titanium, zirconium, and tantalum in steels, determination of, RP2923 ... 11
Nivert, J. M., Jr., E. H. Hamilton, R. M. Waxler, Properties of zinc borosilicate glasses, RP2930 ... 59
Noble, C. E., S. Goodman, S. B. Russell, Effect of internal radiant heat transfer on temperature distribution, thermal stress, and deflection in box beams, RP2949 ... 175
Numerical analysis, theorem of M. Riesz, RP2935 ... 89
Numerical computation, exponential integral, RP2941 ... 123

O

O'Mara, J. H., D. McIntyre, G. C. Doderer, Design and performance of a block-type osmometer, RP2931 ... 63
On a theorem of M. Riesz, RP2935 ... 89
Osmometer, block-type, design and performance, RP2931 ... 63
Oxygen, effect on the bonding of gold to fused silica, RP2942 ... 127

P

Parker, M. S., R. R. Stromberg, A. R. Quasius, S. D. Toner, Adsorption of polyesters on glass, silica, and alumina, RP2933 ... 71
Pearl, M., On a theorem of M. Riesz, RP2935 ... 89
Pergiel, F. Y., W. H. Johnson, E. J. Prosen, Heat of reaction of diborane with water and the heat of formation of boric oxide, RP2927 ... 43
Perloff, A., S. Block, G. Burley, R. D. Mason, Jr., Refinement of the crystal structure of triclinic magnesium pyroborate, RP2936 ... 95
Phase equilibria in the subsystem barium disilicate—dibarium trisilicate, RP2953 ... 193
Phase equilibrium relations in the binary system lead oxide-niobium pentoxide, RP2925 ... 27
Phase of a constant vector plus a Rayleigh-distributed vector, mean absolute value and standard deviation, RP2950 ... 183
Phosphate, silicate, and arsenate, separation and determination, RP2954 ... 201
Photometer, absolute light-scattering: I. Design and operation, RP2946 ... 153
Photometer for determining absolute light scattering from polymer solutions: I. Design and operation, RP2946 ... 153
Pits in metals caused by collision with liquid drops and soft metal spheres, RP2958 ... 229
Plyler, E. K., L. R. Blaine, Infrared high-resolution grating spectrometer, RP2922 ... 7
Polybutadiene and benzene, heat of mixing, RP2921 ... 1
Polyesters, absorption on glass, silica, and alumina, RP2933 ... 71
Polymers, glass formation. II. Rubber-sulfur system, RP2944 ... 141
Polymers, thermal degradation at low rates, RP2957 ... 219
Potassium calcium silicate, heat of formation, RP2955 ... 207
Preparation of new solution standards of radium, RP2924 ... 21
Properties of zinc borosilicate glasses, RP2930 ... 59
Prosen, E. J., W. H. Johnson, F. Y. Pergiel, Heat of reaction of diborane with water and the heat of formation of boric oxide, RP2927 ... 43
—, —, *R. A. Nelson*, Heat of formation of titanium tetrabromide, RP2932 ... 67
—, —, —, Heat of formation of titanium tetrachloride, RP2928 ... 49
—, —, *R. G. Miller*, Heat of formation of boron trichloride, RP2956 ... 213
Pummer, W. J., R. E. Florin, L. A. Wall, Fluorination of haloaromatic compounds, RP2938 ... 107
—, —, —, Reactions of aromatic fluorocarbons with hydrogen, RP2940 ... 119
—, —, —, —, Synthesis of some disubstituted 3,4,5,6-tetrafluorobenzenes, RP2939 ... 113

Q

Quasius, A. R., R. R. Stromberg, S. D. Toner, M. S. Parker, Adsorption of polyesters on glass, silica, and alumina, RP2933 ... 71
Quinn, E. I., F. L. Mohler, Mass spectra of some deuterostyrenes, RP2926 ... 39

R

Page

Radium, preparation of new solution standards, RP2924 ... 21
Reactions of aromatic fluorocarbons with hydrogen, RP2940 ... 119
Refinement of the crystal structure of triclinic magnesium pyroborate, RP2936 ... 95
Resolution of the dissociation constants of *d,l*-malic acid from 0° to 50° C, RP2947 ... 161
Riesz, M., theorem of, RP2935 ... 89
Ross, G. S., L. J. Frolen, Simple rotating molecular still, RP2951 ... 187
Rotating molecular still, simple, RP2951 ... 187
Roth, R. S., E. M. Levin, Phase equilibria in the subsystem barium disilicate—dibarium trisilicate, RP2953 ... 193
—, Phase equilibrium relations in the binary system lead oxide-niobium pentoxide, RP2925 ... 27
Russell, S. B., S. Goodman, C. E. Noble, Effect of internal radiant heat transfer on temperature distribution, thermal stress, and deflection in box beams, RP2949 ... 175

S

Saunders, J. B., F. L. Gross, Interferometer for large surfaces, RP2943 ... 137
Schwebel, A., W. B. Mann, L. L. Stockmann, W. J. Youden, P. A. Mullen, S. B. Garfinkel, Preparation of new solution standards of radium, RP2924 ... 21
Scintillation counter method of intercomparing neutron source strengths by means of a manganous sulfate bath, RP2952 ... 189
Separation and determination of phosphate, silicate, and arsenate, RP2954 ... 201
Silicate, phosphate, and arsenate, separation and determination, RP2954 ... 201
Simple rotating molecular still, RP2951 ... 187
Spectra, infrared absorption, of some cyclic acetals of sugars, RP2960 ... 257
Spectrometer, infrared high-resolution grating, RP2922 ... 7
Steels, determination of titanium, zirconium, niobium, and tantalum, RP2923 ... 11
Stewart, J. E., R. S. Tipson, H. S. Isbell, Infrared absorption spectra of some cyclic acetals of sugars, RP2960 ... 257
Stockmann, L. L., W. B. Mann, W. J. Youden, A. Schwebel, P. A. Mullen, S. B. Garfinkel, Preparation of new solution standards of radium, RP2924 ... 21
Strips with holes loaded through pins, elastic deformation, RP2945 ... 147
Stromberg, R. R., A. R. Quasius, S. D. Toner, M. S. Parker, Adsorption of polyesters on glass, silica, and alumina, RP2933 ... 71
Sugars, infrared absorption spectra of some cyclic acetals, RP2960 ... 257
Synthesis of some disubstituted 3,4,5,6-tetrafluorobenzenes, RP2939 ... 113

T

Tantalum in titanium-base alloys, determination of niobium, RP2929 ... 53
Tantalum, niobium, titanium, and zirconium in steels, determination, RP2923 ... 11
Tetrafluorobenzenes, disubstituted 3,4,5,6-, synthesis, RP2939 ... 113
Theorem of M. Riesz, RP2935 ... 89
Theory of the effect of drag on the orbital inclination of an earth satellite, RP2934 ... 79
Thermal degradation of polymers at low rates, RP2957 ... 219
Thermal stress in box beams, effect of internal radiant heat transfer, RP2949 ... 175
Thornton, H. R., D. G. Moore, Effect of oxygen on the bonding of gold to fused silica, RP2942 ... 127
Tipson, R. S., H. S. Isbell, J. E. Stewart, Infrared absorption spectra of some cyclic acetals of sugars, RP2960 ... 257
Titanium-base alloys, determination of niobium and tantalum, RP2929 ... 53
Titanium tetrabromide, heat of formation, RP2932 ... 67
Titanium tetrachloride, heat of formation, RP2928 ... 49
Titanium, zirconium, niobium, and tantalum in steels, determination, RP2923 ... 11
Toner, S. D., R. R. Stromberg, A. R. Quasius, M. S. Parker, Adsorption of polyesters on glass, silica, and alumina, RP2933 ... 71
Top-loaded monopole antenna, earth currents near, RP2959 ... 247

V

Vectors, a constant plus a Rayleigh-distributed, mean absolute value and standard deviation of the phase, RP2950 ... 183
Vinti, J. P., Theory of the effect of drag on the orbital inclination of an earth satellite, RP2934 ... 79

W

Wade, C., Jr., M. Abramowitz, W. F. Cahill, Heat transfer in laminar flow through a tube, RP2937 ... 101
Wait, J. R., Earth currents near a monopole antenna with symmetrical top loading, RP2959 ... 247
Wall, L. A., R. F. Florin, W. J. Pummer, Fluorination of haloaromatic compounds, RP2938 ... 107
—, —, —, Reactions of aromatic fluorocarbons with hydrogen, RP2940 ... 119
—, —, —, —, Synthesis of some disubstituted 3,4,5,6-, tetrafluorobenzenes, RP2939 ... 113
Walters, L. C., J. R. Johler, Mean absolute value and standard deviation of the phase of a constant vector plus a Rayleigh-distributed vector, RP2950 ... 183
Waxler, R. M., E. H. Hamilton, J. M. Nivert, Jr., Properties of zinc borosilicate glasses, RP2930 ... 59

Y

Youden, W. J., W. B. Mann, L. L. Stockmann, A. Schwebel, P. A. Mullen, S. B. Garfinkel, Preparation of new solution standards of radium, RP2924 ... 21

Z

Zinc boroxilicate glasses, properties, RP2930 ... 59
Zirconium, niobium, titanium, and tantalum in steels, determination, RP2923 ... 11

Important Notice

Beginning in July 1959, the Journal of Research will be published in four separate sections which may be subscribed for individually. This change is being made to provide a publication whose subject matter concentrates on particular fields of interest, thus meeting the specialized needs of individual scientists, engineers, and mathematicians.

Section A. Physics and Chemistry, to be issued bimonthly, will present papers of interest primarily to scientists working in these fields. This section will cover a broad range of physical and chemical research, with major emphasis on standards of physical measurement, fundamental constants, and properties of matter.

Section B. Mathematics and Mathematical Physics, to be issued quarterly, will present results in pure and applied mathematics, including mathematical statistics, theory of experiment design, numerical analysis, and short numerical tables; theoretical physics, chemistry, and engineering, where the emphasis is on the mathematical content or methodology; and logical design, programing, and applications of electronic computers and computer systems.

Section C. Engineering and Instrumentation, to be issued quarterly, will report results of interest chiefly to the engineer or applied scientist. This section will include many of the new developments in instrumentation resulting from the Bureau's work in physical measurement, data processing, and the development of test methods. It will also cover some of the work in acoustics, applied mechanics, building research, and cryogenic engineering.

Section D. Radio Propagation, to be issued bimonthly, will report research in radio propagation, communications, and upper atmospheric physics. Topics to be covered include propagation in ionized media, scattering by turbulence, the effect of irregular terrain on propagation, diffraction and scattering by solid obstacles, propagation through time-varying media, and antennas.

All present subscribers to the Journal will receive an announcement from the Superintendent of Documents when advance orders for the new sections can be accepted.

U.S. GOVERNMENT PRINTING OFFICE: 1959